Exchange Bias and Its Angular Dependence in $Fe_xZn_{1-x}F_2$ / Co Bilayers

By Hongtao Shi

DISSERTATION

Submitted to the Eberly College of Arts and Sciences

at

West Virginia University

In partial fulfillment of requirements for the Degree of

Doctor of Philosophy
In Physics

David Lederman, Ph.D., Chair
Larry Halliburton, Ph.D.
Mohindar Seehra, Ph.D.
Thomas Myers, Ph.D.
Charter Stinespring, Ph.D.

Morgantown, West Virginia

2002

Keywords:
thin film, molecular beam epitaxy, ferromagnet, antiferromagnet, cobalt, iron fluoride, zinc fluoride, exchange bias, angular dependence

ABSTRACT

Exchange Bias and Its Angular Dependence in $Fe_xZn_{1-x}F_2$ / Co Bilayers

Hongtao Shi

When materials with antiferromagnetic (AF) / ferromagnetic (F) interfaces are cooled through the Néel temperature (T_N) of the AF in a magnetic field, a unidirectional magnetic exchange anisotropy (EA) is induced in the F layers. Such anisotropy is manifested by a shift of the center of the F hysteresis loop by an amount known as exchange bias H_E. Exchange anisotropy has attracted much attention in the last decade due to its applications in magnetic random access memory, permanent magnets, and magnetic recording media. Despite this interest, the basic mechanism responsible for EA is not well understood.

In this thesis the EA is studied in dilute Ising antiferromagnets as a function of dilution, interface structure and angle of the various applied magnetic fields.

In the first set of experiments, antiferromagnetic $Fe_xZn_{1-x}F_2$ / ferromagnetic, polycrystalline Co bilayers were grown on MgO (100) substrates via molecular beam epitaxy (MBE). X-ray diffraction showed that the dilute antiferromagnet is (110)-oriented with two perpendicular crystallographic twins in the film plane. After field cooling samples with and without 1.0 nm pure FeF_2 at the interface between the $Fe_xZn_{1-x}F_2$ layer and the Co layer through the T_N of the AF layer, hysteresis loops were measured using a superconducting quantum interference device (SQUID) magnetometer to determine H_E in the bilayers. The blocking temperature T_B, at which $H_E = 0$, was found to have a linear dependence on the concentration of Fe, x, in the dilute layer for $x > 0.25$, which coincides with the T_N of the bulk dilute crystals. The exchange bias was increased by 65% for $x = 0.84$ compared to pure FeF_2 / Co bilayers. This enhancement is presumably due to the formation of domain states inside the dilute antiferromagnetic layers, and the pure interface layer is crucial in increasing the coupling between the F and the AF layers.

The angular dependence of H_E, as well as the coercivity and the remanence, on the cooling field direction was studied in the twinned samples using a vibrating sample magnetometer (VSM). The cooling field was applied at an angle α with respect to the twins' perpendicular bisector in the plane of the samples. The most negative H_E was found to occur along the AF easy c-axis for $0 \leq \alpha \leq 30^0 \sim 40^0$. An exchange bias flop occurred if α was increased further. The 1.0 nm pure FeF_2 interface layer resulted in a sharper exchange bias flop transition, indicating that the pure interface layer acts as a buffer for the interface interaction.

As a comparison, single crystal FeF_2 / Co bilayers were also prepared. A large H_E was observed with the sample field-cooled along the easy axis of FeF_2, whereas two loops with the same H_E magnitude but of opposite signs were observed when the cooling field was applied 90^0 to the AF easy c-axis. Changing the cooling field direction to 91^0 caused the sample to acquire a significant positive H_E parallel to the AF easy axis.

These experiments demonstrate that the interface coupling responsible for H_E is extremely sensitive to the underlying magnetic anisotropy of the AF layer, and that the direction of the cooling field does not necessarily determine the direction of H_E.

Dedication

To my family for their love, encouragement, and patience

Acknowledgements

I would like to thank my research advisor, Professor David Lederman, for directing my efforts in the field of magnetism, the guidance and the patience. Thanks are also given to the committee members for their time on the dissertation. I would also like to thank Timothy Charlton, Erie Morales, Yikuan Wang and Jorge Espinosa for their help in the laboratory. I also acknowledge the machine shop personnel, Carl Weber, Dough Mathess, and Tom Milam, for their instructions on the use of the machines, and the fabrication of the parts for the experiments. I am in debt to Prof. Charter Stinespring for doing the Auger experiments. I owe thanks to Dr. Eric E. Fullerton in IBM Almaden for his initial suggestion of the work on angular dependence of the exchange bias. Crystagon, Inc. in Ohio provided us free single crystal MgF_2, which is greatly appreciated.

Contents

Chapter

Tables

Table

Figures

Figure

Chapter 1

Introduction

1.1 Magnetic Anisotropy

Almost all magnetic materials have some magnetic anisotropy, *i.e.*, the magnetic properties depend on the direction in which the magnetic field is applied. A magnetic anisotropy may be characterized by easy directions of magnetization, along which a magnetic material will tend to magnetize and a certain amount of energy is required to point its magnetic moment along intervening hard directions. Examples of magnetic anisotropy are shown in Figure 1.1, where the magnetization **M** is plotted as a function of applied magnetic field **H** along different crystallographic directions for body-centered-cubic (*bcc*) iron (Fe), face-centered-cubic (*fcc*) nickel (Ni), and hexagonal-closed-packed (*hcp*) cobalt (Co),[1] which indicates that *bcc* [100], *fcc* [111], and *hcp* [0001] are the easy directions for Fe, Ni, and Co, respectively.

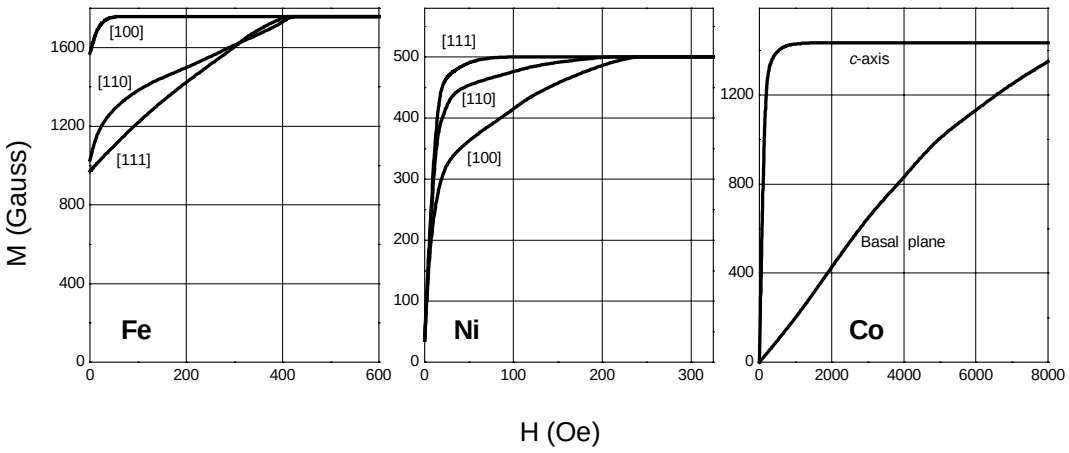

Figure 1.1: Magnetization curves of Fe, Ni, and Co with easy axis along *bcc* [100], *fcc* [111], and *hcp* [0001] for Fe, Ni, and Co, respectively. After Ref. 1.

The source of magnetic anisotropy can be the symmetry of the crystal structure, which results in magnetocrystalline anisotropy (Fig. 1.1); the shape of the grain; surface anisotropy; or stress within the crystal (which affects the magnetostrictive energy due to spin-orbit coupling). The effective field that represents the magnetocrystalline energy is called the coercive field or coercivity. The coercivity, H_C, is therefore the field sufficient to overcome the anisotropy energy and change the magnetization of the crystal.

The direction of magnetization of a ferromagnetic material therefore results from the competition among different energies such as the following:

1) Exchange energy: minimized when spins are aligned with one another.
2) Uniaxial anisotropy energy: minimized when spins are aligned along easy directions.
3) Thermal energy: acts to randomize magnetic moments.
4) Zeeman energy: minimized when the magnetic moments are aligned with the external field.
5) Magnetostatic energy: minimized when the magnetization points in the direction of the magnetic dipole moment fields created at the boundaries of the specimen.

It is often convenient to express the magnetocrystalline anisotropy energy in terms of the crystal anisotropy constants, K_1, K_2, K_3, *etc*. These are usually defined by expressing the free energy of crystal anisotropy as a function of the directional cosines, α_1, α_2, α_3, of the magnetization vector **M** with respect to the crystallographic axes. For example, in a cubic crystal, the magnetic anisotropy energy, written in ascending α's, is

$$E_k = K_0 + K_1(\alpha_1^2\alpha_2^2 + \alpha_2^2\alpha_3^2 + \alpha_3^2\alpha_1^2) + K_2\alpha_1^2\alpha_2^2\alpha_3^2 + ... \qquad (1.1)$$

The units commonly used are *erg/cm*^{3}. Terms in odd powers are absent due to the cubic symmetry. Higher terms are typically not necessary to express experimental results, and usually the term K_2 is negligible compared to K_1.

The uniaxial magnetocrystalline anisotropy of *hcp* crystals, such as Co, can be expressed to lowest order by the following formula:

$$E_K = K_{U1} \sin^2 \theta + K_{U2} \sin^4 \theta, \tag{1.2}$$

where θ is the angle between the magnetization and the easy axis, which is parallel to the crystallographic *c*-axis. Notice that the magnetic anisotropy energy is minimized at $\theta = 0$ and $\theta = 180^0$, and therefore the uniaxial anisotropy has a two-fold symmetry, *i.e.*, it is *bidirectional*.

1.2 Exchange Anisotropy

Exchange anisotropy (EA) or exchange bias (H_E) refers to the fact that an antiferromagnetic (AF) layer in contact with a ferromagnetic (F) layer affects the magnetic response of the F layer due to the interface coupling. EA was discovered in 1956 by Meiklejohn and Bean on ferromagnetic Co particles (~ 20 nm in diameter),[2] that were partially oxidized to form CoO. A compact of the partially oxidized cobalt particles cooled from 300 K to 77 K in a magnetic field had a hysteresis loop shift along the cooling field (H_{CF}) direction compared to the zero-field cooling ($H_{CF} = 0$), as shown in Figure 1.2. In other words, the center of the hysteresis loop, which traced out the history-dependent path of magnetization reversal, was displaced along the field axis.

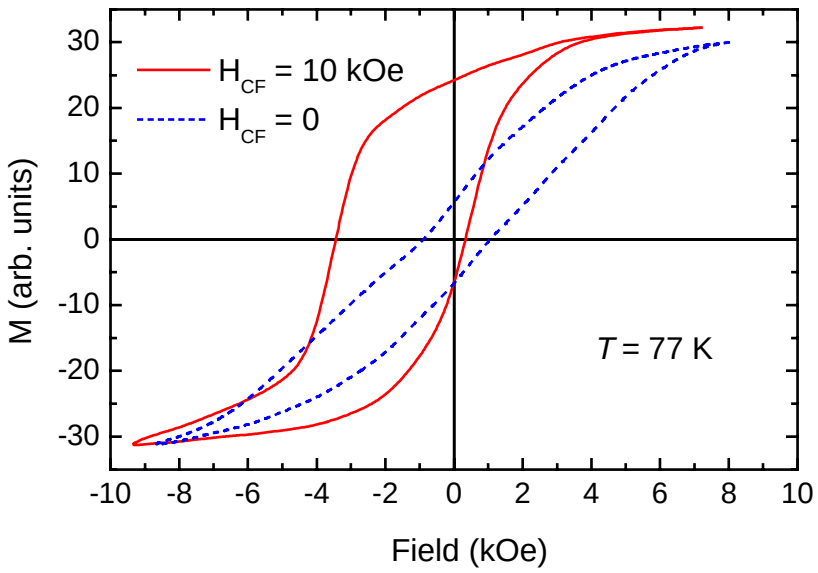

Figure 1.2: Hysteresis loops of 20 nm diameter, partially oxidized Co particles measured at 77 K. The solid line corresponds to data after cooling the material in a 10 kOe field. The dashed line results from cooling in zero field. After Ref. 2.

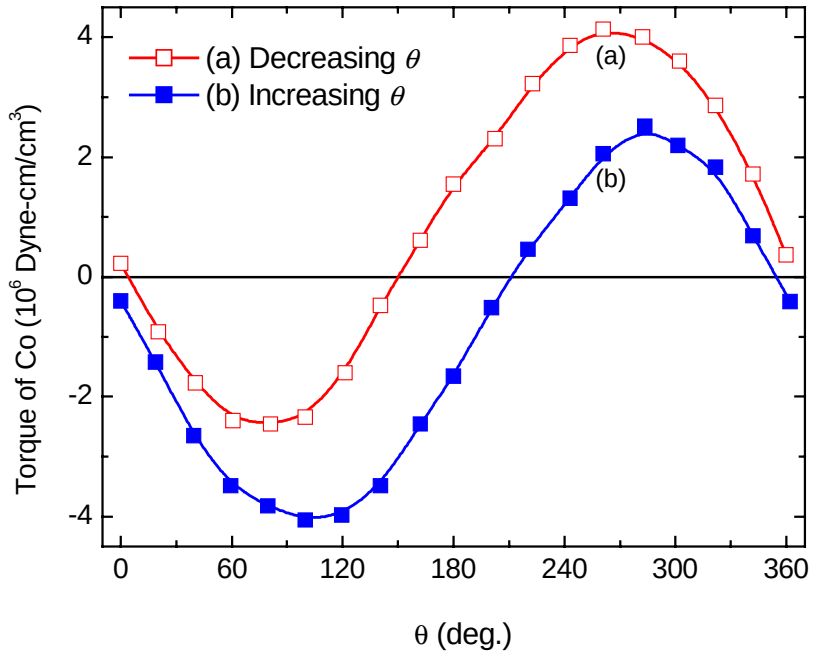

Figure 1.3: Torque curves on partially oxidized Co particles at 77 K. The sample was cooled in H_{CF} = 20 kOe along θ = 0, and the torque measured at 7.5 kOe. Curve (a) is for rotation of decreasing θ and curve (b) for increasing θ. After Ref. 3.

The torque data shown in Figure 1.3 of such a speciman[3] rotated in a large field is predominantly dependent on $\sin\theta$, indicating that there is only one stable equilibrium for the average magnetization. The anisotropy is therefore *unidirectional*, in contrast to the uniaxial anisotropy, which is *bidirectional*. Meiklejohn and Bean qualitatively explained this behavior, by considering that CoO antiferromagnetically orders at 291 K or below. When the cooling field H_{CF} is applied at room temperature, the Co magnetization is aligned with the field due to the large Co Curie temperature (T_C = 1403 K), while the magnetic moments of the Co in the oxide are affected only very slightly. Upon cooling through the Néel temperature (T_N) of the CoO, the moment arrangement in the oxide may be dictated by exchange interactions at the interface. Subsequent reversal of the applied magnetic field will cause the magnetization of the Co to rotate while the moment arrangement in CoO, which has a high uniaxial anisotropy, is unaffected far from the interface. If the reverse field is removed, the magnetization of the Co particles will tend to return to its original direction.

To generalize that idea, Figure 1.4 shows how the hysteresis loop of a single ferromagnetic layer differs from that of an exchange coupled AF/F bilayer, as well as the definition of exchange bias H_E and coercivity H_C. The advantage of this bilayer is that the ferromagnetic layer is in a well-defined state at zero applied field.

Since its discovery, exchange bias has been examined in detail in many nano-sized systems, mainly ferromagnetic particles covered by their native oxide, such as Co / CoO,[4] Ni / NiO,[5] Fe / FeO,[6] Fe / Fe_3O_4,[7] as well as in thin film bilayer systems,[8, 9, 10, 11] due to its technological applications in magnetic random memory,[12] spin valves,[13] and magnetic recording applications.[14]

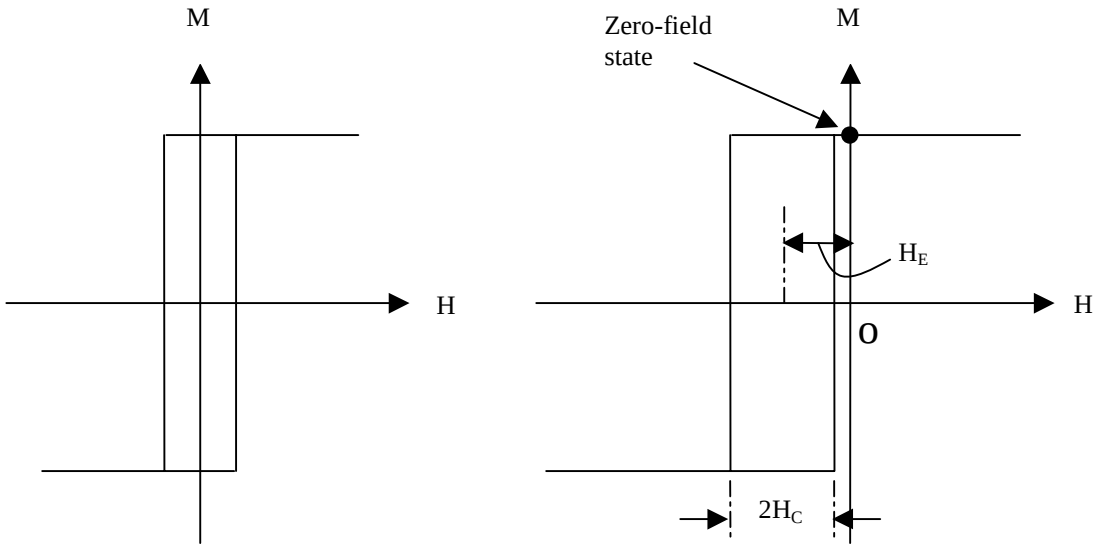

(a) Single F layer (b) Exchange coupled AF/F layer

Figure 1.4: Schematic diagrams contrasting normal (a) and exchange coupled (b) hysteresis loops. The biased case is usually accompanied by an increase in the coercive field H_C. After Ref. 14.

1.3 Thin Film Systems

In order to better understand the fundamental aspects of exchange bias, more controlled systems, based on an antiferromagnetic thin film coated with a ferromagnetic layer, or a ferrimagnetic layer, have been investigated, for example, Co / CoO,[15] Fe_3O_4 / CoO,[16] NiFe / FeMn,[17] Fe / FeF_2,[18] Fe / MnF_2.[19] This procedure allows for better characterized AF/F interfaces than in the small nano-particles and inhomogeneous materials that were initially studied. The dependence of exchange bias on the spin configurations at the interfaces can be accomplished by selecting different crystallographic orientations. Also the role of interface roughness can be understood from thin-film systems by changing the growth parameters using high vacuum techniques such as magnetron sputtering or molecular beam epitaxy. From the applied points of

view, most of the device applications based on exchange bias are in thin film form. Many other interesting phenomena, such as the exchange bias dependence on the thickness of the AF layer, F layer, spacer, dilution of the AF, can be readily explored.

To compare different systems, independent of the ferromagnetic material and its thickness, the magnitude of the exchange bias is often described in terms of an interface energy per unit area:[14]

$$\Delta E = M_F t_F H_E , \tag{1.3}$$

where M_F and t_F are the saturation magnetization and the thickness of the F layer, respectively, and H_E is the magnitude of the exchange bias.

Early work on thin oxidized transition metal films showed that Co / CoO exhibited a rather large exchange bias, compared to Ni / NiO and Fe / FeO. However, the oxide layer could not be measured accurately because the films tend to oxidize through the grain boundaries, therefore increasing the effective interface surface area.

1.3.1 Temperature Dependence

The exchange bias vanishes at a temperature often defined as the blocking temperature (T_B). In some cases, T_B is much lower than the bulk T_N of the AF, whereas in some other cases, T_B is very close to T_N. The origin of this effect seems to be closely related to the grain size and the thickness of the AF layer through finite size effects.[20] If the AF thickness is thinner than a system-dependent critical thickness, then T_N will be greatly reduced, which results in a smaller T_B. Other factors influencing T_B include the stoichiometry of the AF layers or the multiphased structure in the AF. Nevertheless, the distribution of the blocking temperature certainly exists in the bilayer system due to disorder such as different grain sizes or interface roughness. This

distribution can be studied by warming the sample to $T < T_B$, and then cooling in a field opposite to the original cooling field direction. The change in H_E caused by field cooling from different temperatures T ($< T_B$) gives information about the width of the T_B distribution.[13]

1.3.2 Thickness Dependence

The role of the thickness of the AF (t_{AF}) and F (t_F) layers in exchange-coupled bilayers has been studied in detail. For many systems H_E is roughly inversely proportional to t_F,[21] indicating that the exchange bias is an interface effect. As long as t_F is smaller than the F domain wall size, this relationship holds.[14] If the F layer is too thin, this relationship is not valid any more, probably due to the discontinuity of the film, which usually occurs at around a few nanometers. It is also closely related to the microstructure and the growth of the F layer.

The H_E dependence on the AF thickness is more complicated than the F thickness dependence, which is related to the spin configurations in the AF, as well as the anisotropy of the AF, the direction of the cooling field, *etc*. H_E generally is independent of t_{AF} for thick AF layers, for example, on the order of 20 nm and greater.[22] As the AF layer becomes thinner, H_E decreases very quickly. If t_{AF} is thin enough, then H_E becomes zero. Several factors could be related to this behavior. In order to observe exchange bias, $K_{AF}t_{AF} > J_{AF/F}S_{AF}S_F$, which can be deduced from Meiklejohn-Bean model,[5] where K_{AF} is the anisotropy of the antiferromagnet, $J_{AF/F}$ is the exchange interaction across the AF/F interface, and S is the spin state of the AF or F.[11] If this condition is not met, then reversing the F layer will switch the antiferromagtic order in parts of the AF layer, leading to an enhancement of coercivity, but the exchange bias will remain zero. Very recently, Binek *et. al.*[10] have generalized the Meiklejohn-Bean approach to obtain an analytical expression for the critical AF thickness:

$$t^{C}_{AF} = \frac{J_{AF/F} S_{AF} S_F}{2\sqrt{2} K_{AF}}, \tag{1.4}$$

which is quite similar to Meiklejohn-Bean model. Recent experiments,[11] in which the AF layers MnF_2 (anisotropy field = 7 kOe, t^{C}_{AF} = 14 nm) and FeF_2 (anisotropy field = 149 kOe, t^{C}_{AF} = 1.2 nm) were grown in a wedged structure, seemed to support such model, after taking into account the fact that the anisotropy fields of those two materials differ by a factor of 20. The exchange bias remains unchanged for t_{FeF2} > 25 nm. The small difference of t^{C}_{AF} between theory and experiment is probably due to the fact that the AF layers do not have a uniaxial anisotropy due to the orthogonal twin domains in MnF_2 or FeF_2 when grown on MgO (100) substrates, as explained further in Chapter 3.

1.3.3 Orientation Dependence

Due to the interface nature of H_E, exchange bias is also expected to strongly depend on the AF spin configurations at the interface, which essentially depends on the crystal structure of the AF, assuming the interface of the *AF* maintained the same spin configurations as in the bulk.

FeF_2 is a good candidate to verify this scenario because of the readiness of obtaining films with different orientations and the strong uniaxial anisotropy along the easy *c*-axis. H_E has been shown to vary when grown on different substrates with different crystal orientations.[23, 24] When it is (110) oriented, all the spins are in the plane, which results in a maximum exchange bias. When it is (001) orientated, all the spins are perpendicular to the interface, and H_E = 0. For (101)-oriented FeF_2, the *AF* spins have some intermediate angle between 0 and 90^0, and H_E is about half of the value obtained for (110) case. The same trend is also found in FeMn except the fact that FeMn has more complicated spin structures.[22]

An intuitive picture for this orientation effect is from the AF/F spin-spin interaction strength given by:[23]

$$H \sim S_{AF} S_F \cos\alpha, \tag{1.5}$$

with α the angle between both spins. If the F spins lay in the interface plane due to shape anisotropy, α is the angle between the AF spins and the interface plane, then for in-plane AF spins, $\alpha = 0$, H_E is maximized. For $\alpha = 90^0$, $H_E = 0$.

Another possible explanation is that the domain formation in the AF dominates the H_E, *i.e.*, $H_E \propto (K_{\text{eff}} A_{\text{eff}})^{1/2} \propto (K_{\text{AF}} A_{\text{AF}})^{1/2} \cos\alpha$.[14] Therefore, the effective anisotropy and stiffness will play a major role in determining the magnitude of H_E.

Several other factors, such as the crystallinity of the AF layer, interface roughness, grain size, interface impurity, *etc*. could strongly affect H_E, making exchange coupling much more complicated than expected.

1.4 Theoretical Models

Unidirectional anisotropy and exchange bias can be qualitatively understood by assuming a simple exchange interaction at the AF/F interface. This intuitive picture always gives H_E values several orders of magnitude larger than those observed experimentally.[22] In order to account for the discrepancy, different approaches have been proposed to model the hysteresis loops, including the formation of domains in the AF,[25, 26] perpendicular coupling between the F and the AF,[27] domain state models in the AF layer,[28] and incomplete domain formation in the F layer,[29] However, all of those models can only explain the experimental results to some extent with many other aspects to be solved in the future.

To summarize, it is now known that exchange bias is a feature of exchange-coupled AF/F films, in which a short-range exchange interaction exists. The resulting magnetic order may be accounted for by considering interactions with nearest-neighbors only. From experiments with Co / CoO particles, as well as in many other systems, it has been shown that exchange anisotropy is mainly an interface phenomenon. Another essential feature of exchange coupled systems is magnetocrystalline anisotropy in the antiferromagnet. It is the coupling of the ferromagnet spins to this anisotropy that results in biased magnetization curves, which was stressed very recently.[30] One requirement to observe H_E is the application of an external field while the bilayer system is cooled below the antiferromagnet T_N, or a magnetic field has to be applied during the growth of the bilayer.[14, 31]

Recent experimental investigations have made the first step towards probing the spin structure at AF/F interfaces,[32, 33] while new theoretical models have realistically taken into account the interface disorder and structure of the materials,[34] which elucidated the expected interfacial structure more clearly. However, a universal quantitative understanding of the exchange bias phenomenon remains elusive.

1.5 Motivation for the Present Work

Since exchange bias strongly depends on the magnetic anisotropy of the underlying AF layers, it would be interesting to see how the exchange coupling changes in dilute $Fe_xZn_{1-x}F_2$ / Co systems. $Fe_xZn_{1-x}F_2$ has a large uniaxial magnetic anisotropy along the easy [001] *c*-axis of the crystal, which is considered to be an ideal random field Ising model system. By using different substrates such as (100)-oriented MgO or (110)-oriented MgF_2, different domain structures may be achieved in such dilute systems. Exchange coupling between $Fe_xZn_{1-x}F_2$ and Co can thereafter

be studied to demonstrate the dependence of exchange bias on the dilution, magnetic anisotropy of the AF layers, interface structure, as well as on the angle of various applied magnetic field.

Chapter 2

Experimental Techniques

2.1 Molecular Beam Epitaxy

This dissertation focuses on $Fe_xZn_{1-x}F_2$ / Co bilayer samples that were grown in ultra-high vacuum (UHV) chamber via molecular beam epitaxy (MBE). As is well known, MBE combines precise control of film thickness and composition profiles with the ability to study film growth in real time using a variety of *in situ* structural and chemical probes, for example, reflection high-energy electron diffraction (RHEED), low-energy electron diffraction (LEED), Auger electron spectroscopy, X-ray photoelectron spectroscopy, scanning probe microscopy, *etc*. In MBE, the substrate is maintained in ultra-high vacuum (base pressure $\leq 10^{-9}$ Torr) during its *in situ* preparation and the growth process. The source of atoms or molecules for growth is the vapor flux from thermal sources, typically crucible sources (effusion cells) or electron-beam-heated metal charges. The advantage of UHV deposition is to minimize incorporation of impurities into the film from background species.

A schematic of the metals / insulator MBE system in the WVU lab is shown in Figure 2.1, which has a base pressure of less than 2 x 10^{-9} Torr after the liquid nitrogen cryopanel is filled. Two electron guns are located on each side of the main chamber. A single carbon crucible (40 cm^3) in the left gun contained compressed FeF_2 pellets, whereas the right one has four small crucibles (6 cm^3), containing source materials such as Co, Ni, MgF_2, depending on the need of the experiments. At the bottom of the chamber there is an effusion cell with a quartz crucible containing compressed ZnF_2 pellets.

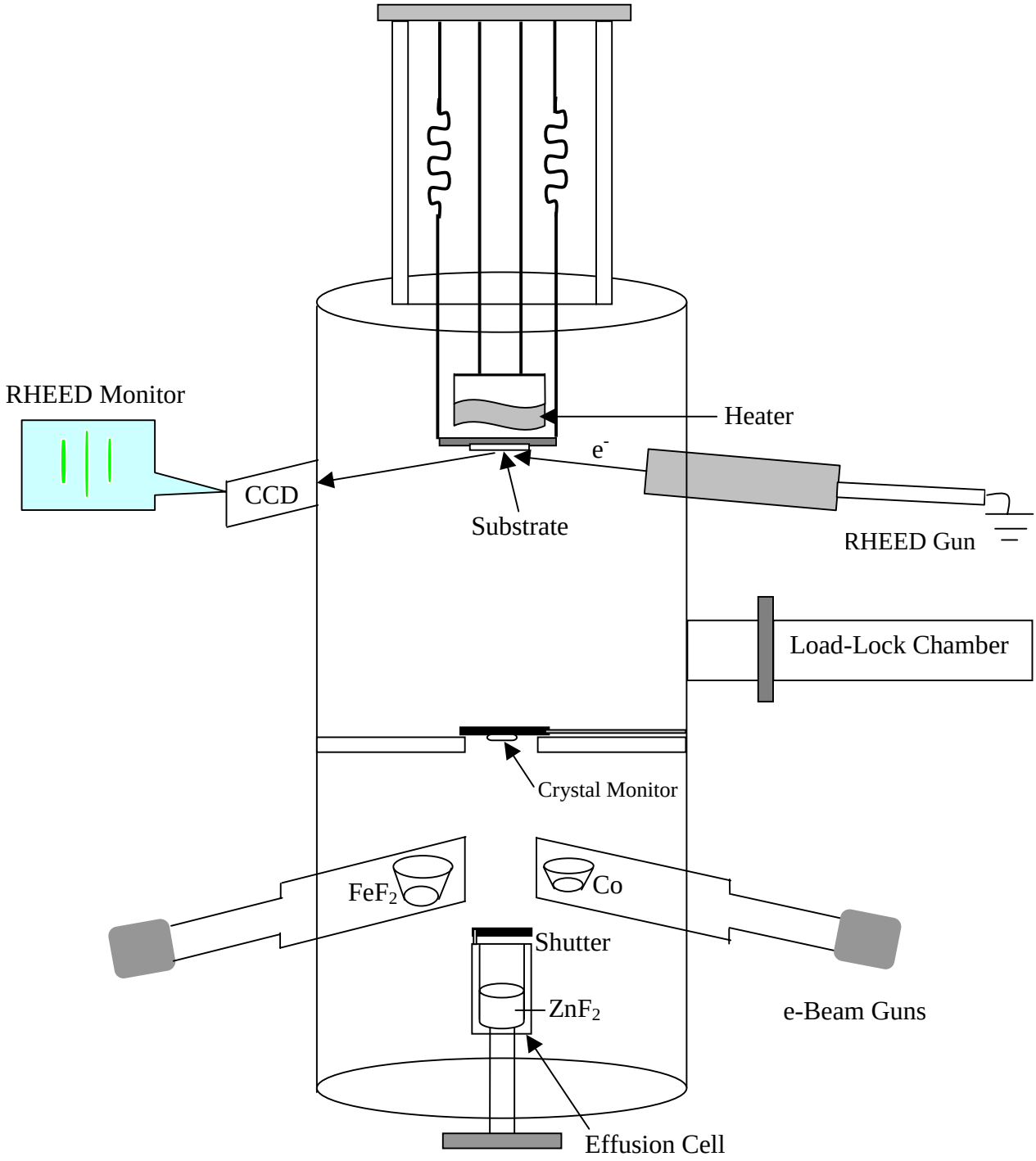

Figure 2.1: Schematic of the MBE chamber.

Each e-beam gun has a filament which emits a certain amount of electrons with the trace controlled by a magnetic field generated by coils in the gun. A circular pattern was chosen in the experiment to ensure that the source materials were uniformly heated. Quartz crystal monitors were installed in the chamber above the source materials to determine the evaporation rates prior to the growth. FeF_2 and Co were typically evaporated at 0.02 nm/s, whereas the growth rate of ZnF_2 was chosen to obtain the right concentration of Fe in $Fe_xZn_{1-x}F_2$ samples. During the growth process, the substrate was rotating about an axis parallel to the growth direction. A stationary heater was placed above the rotatable substrate cradle. The temperature calibration was done by placing a thermocouple on the surface of a Al_2O_3 substrate, and then recording the temperatures measured by the sample and heater thermocouples. The calibration curve is shown in Figure 2.2. Different materials had different optimum growth temperature, which essentially depends on the power to the heater.

In order to check the crystallinity of the substrate and the film, the MBE is equipped with an *in-situ* RHEED system to monitor the crystal surface that will be discussed in section 2.2.

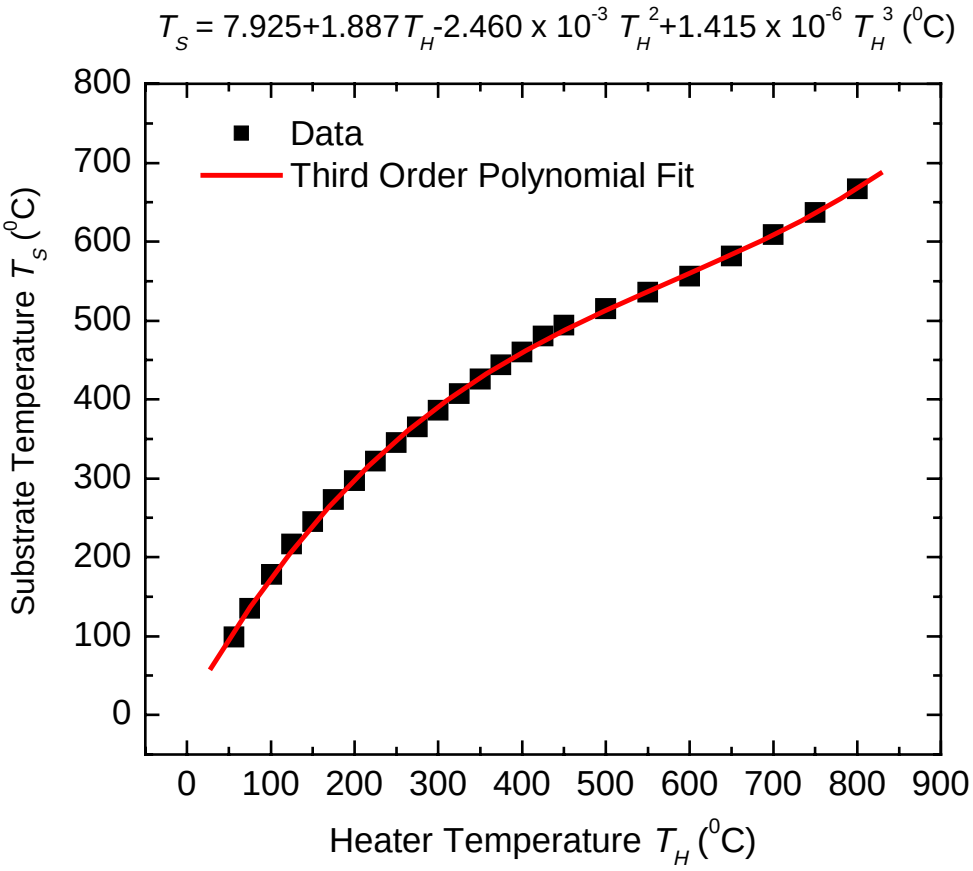

Figure 2.2: Calibrated temperature on the surface of the substrate (T_S) as a function of the temperature at the heater (T_H). Line represents a third order polynomial fit to the experimental data (solid squares), shown on top of the graph.

2.2 Reflection High Energy Electron Diffraction (RHEED)

During the past decade, reflection high-energy electron diffraction, or RHEED, has been widely used in thin films and established itself as a powerful *in-situ* surface-sensitive technique to characterize the surface structure of a crystal and qualitatively measure the surface properties of the sample during the growth process. This technique can also be carried out quantitatively to measure the in-plane surface lattice parameters and the in-plane coherence length of a sample.[35]

In RHEED, an electron beam has an incident angle of less than one degree, which is well collimated and monoenergetic. The electron beam is usually accelerated to energies ranging from 5 keV to 100 keV, striking the crystal surface at a variable glancing angle. Elastic back scattering is very weak when electrons are incident at such high energy. Elastic scattering is sharply peaked in the forward direction. The grazing incidence of the electrons, as well as the strong interaction of the electron beam and the electronic system of the sample, ensures that the penetration depth is limited to a few Å. By rotating the sample about the surface normal, different diffraction patterns related to the surface crystallographic information can be obtained, *i.e.*, surface periodicity and the crystal symmetry of the surface. Diffracted electrons are collected by a phosphorus screen and the data are acquired using a charge-coupled device (CCD) at similar angles on the opposite side of the surface normal.

A schematic experimental setup of RHEED in our lab is shown in Figure 2.3, which was provided by *k*-Space Associates (KSA 400).[36] The applied voltage to the electrons is 15 kV. This model combines a high-resolution, high-sensitivity imager, optimized optics, and image digitizer with sophisticated, RHEED-specific acquisition and analysis software. All hardware interfacing with the computer is taken care of, and acquisition and analysis is visually driven, resulting in simple, straightforward user operation. Determination of lattice spacing, strain

evolution, growth rate, thickness, coherence lengths, and reconstruction evolution can be performed using the KSA software.

Based on the wave nature of the electrons, one can calculate the wavelength of the incident e-beam with a certain accelerated energy E in the unit of electron volt (eV):

$$\lambda = \sqrt{\frac{150.4}{E}}(\text{Å}). \qquad (2.1)$$

The range of the wavelength varies from 0.04 to 0.12 Å, depending on the accelerating energy of the beam E.

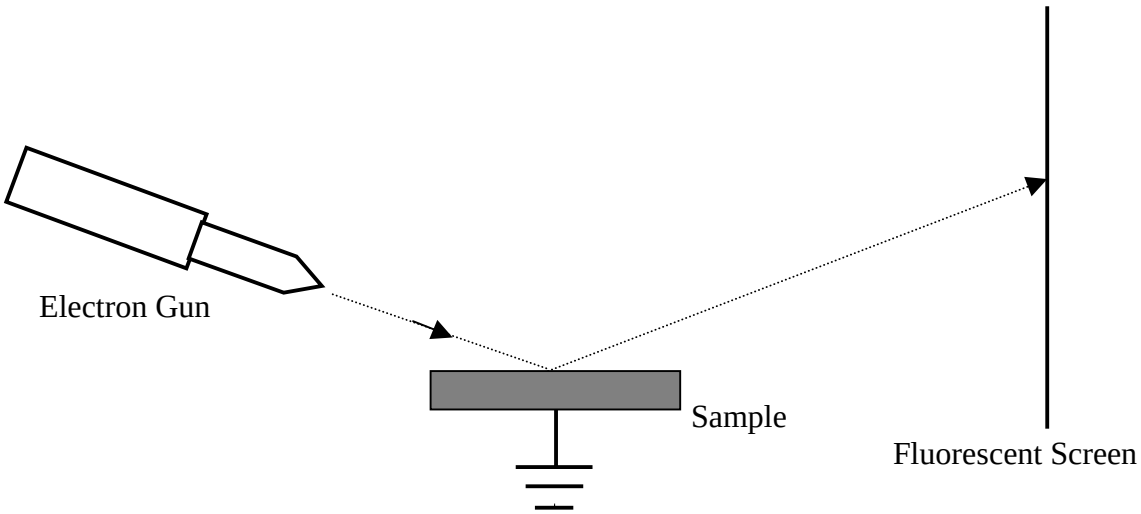

Figure 2.3: Schematic diagram of RHEED.

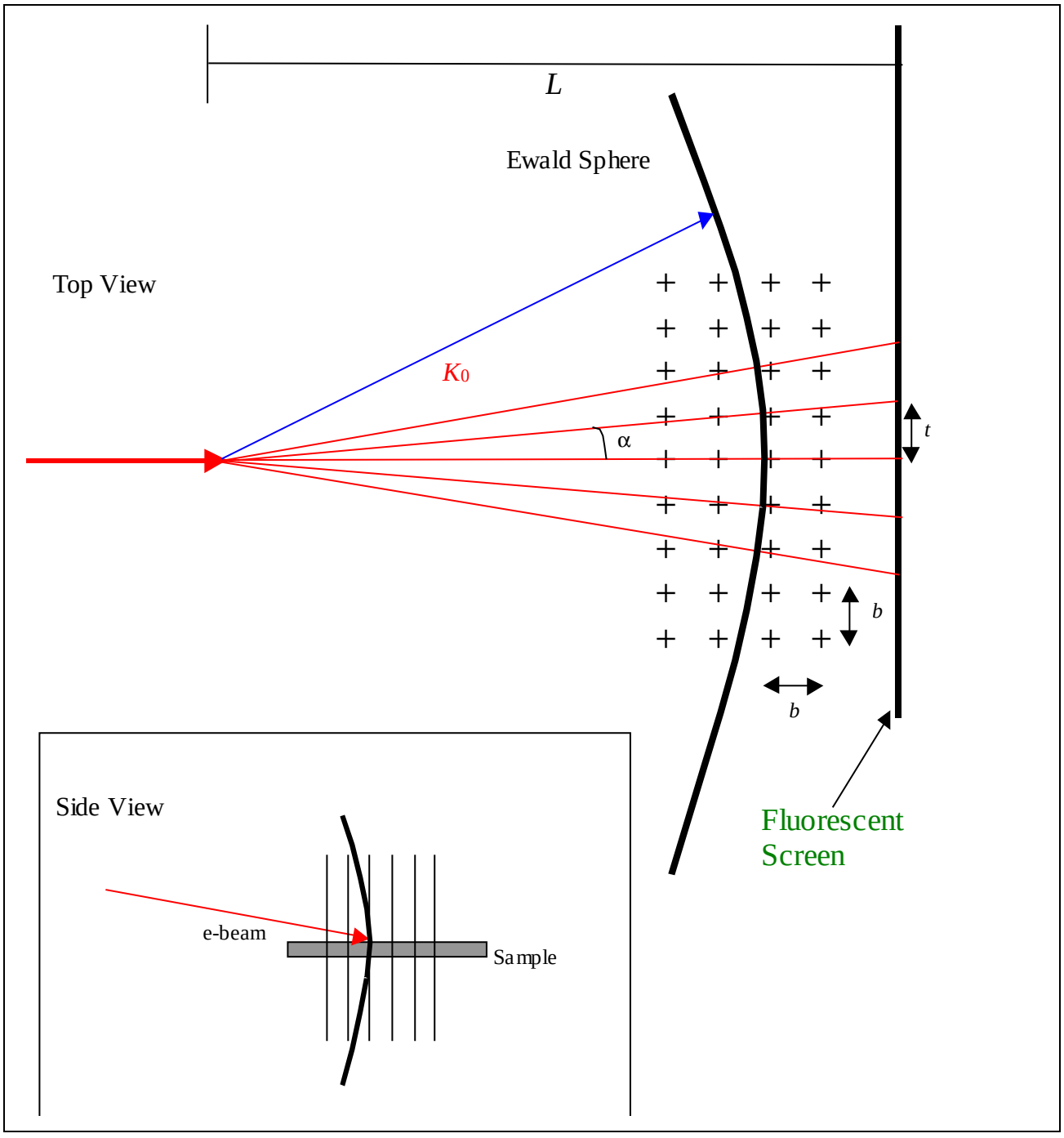

Figure 2.4: Top view and side view of the Ewald sphere.

Figure 2.4 shows the Ewald sphere of the incoming electron waves and the reciprocal space map of a diperiodic (surface) structure. Wherever the Bragg diffraction criteria are met the Ewald sphere of the incoming electron waves will intersect the reciprocal lattice rods of the surface of the sample, oriented perpendicular to the sample plane. This results in streaks spaced by a distance *t* on the florescent screen. Because the radius of the Ewald sphere is approximately two orders of magnitude greater than the modulus of the reciprocal lattice vector, one can find that the angle between points intersecting the sphere will be almost the same.

The surface lattice parameters can be determined as follows.[36] Suppose *b* is the distance, in *k*-space, between reciprocal lattice rods. This is of the order of 2 $Å^{-1}$, whereas the wave vector of the incoming electron beam, $\boldsymbol{K_0}$, is of the order of 100 $Å^{-1}$. As a result, the Ewald sphere will only touch a few rods on either side of the (00) rod.

From Laue conditions:

$$tan\alpha = \frac{b}{k_0} = \frac{t}{L}, \tag{2.2}$$

$$b = \frac{2\pi}{d_{parallel}}. \tag{2.3}$$

Therefore

$$d_{parallel} = \frac{L\lambda_0}{t} \tag{2.4}$$

where $d_{parallel}$ is the distance between equivalent rows of atoms parallel to the incident beam and $L\lambda_0$ is found by using a sample whose lattice constant is well known. By rotating the sample about its *z*-axis (surface normal) and measuring $d_{parallel}$ at known angles, the crystallographic structure of the sample can be determined.

One can also use RHEED to characterize a surface by its disorder. For a perfect electron beam and a perfect crystal with no disorder, the width of the Ewald sphere and the lattice rods would be infinitesimally small. This would result in a series of spots on the phosphorous screen.

However, a small dispersion of wavelengths incident on the screen and the finite width of the beam means that the Ewald sphere has a finite thickness, resulting in spots that extend vertically on the phosphorous screen, causing a series of streaks to appear. Also the broadening of the reciprocal lattice rods, due to structural disorder, causes a broadening of these streaks.

As a result, investigating the RHEED pattern can give the information about:

- In-plane lattice parameters as well as the crystal symmetry in the sample plane;
- Smoothness of the sample surface: A pure spotted pattern resulting from transmission of electrons through surface islands shows that the sample is not flat;
- Coherence length: Measuring the full width at half maximum (FWHM) of the diffraction streaks can allow one to quantify the in-plane grain size or correlation length. This is defined as the length scale over which the atomic positions are crystallographically correlated.

The RHEED apparatus in the lab has been mainly employed as a tool to monitor the surface of the dilute antiferromagnetic (DAF) $Fe_xZn_{1-x}F_2$ samples. By acquiring the RHEED patterns, we could determine the in-plane lattice parameters, both parallel and perpendicular to the magnetic easy *c*-axis of the DAF films.

2.3 X-ray Diffraction (XRD)

2.3.1 High Angle X-ray Diffraction

X-ray diffraction is a powerful non-destructive technique for characterizing crystalline materials. It provides information on structures, phases, preferred crystal orientations (texture) and other structural parameters such as average grain size, crystallinity, strain and crystal defects. X-ray diffraction peaks are directly related to the atomic distances, which are produced by constructive interference of monochromatic beam scattered from each set of lattice planes at specific angles, when the Bragg condition is satisfied. For a given set of lattice plane with an inter-plane distance of *d*, Figure 2.5 shows the schematic when the diffraction occurs, where λ is the wavelength of the incident x-ray, θ is the incident angle, $\boldsymbol{K_i}$ and $\boldsymbol{K_f}$ are the wave vectors of the beam before and after the diffraction.

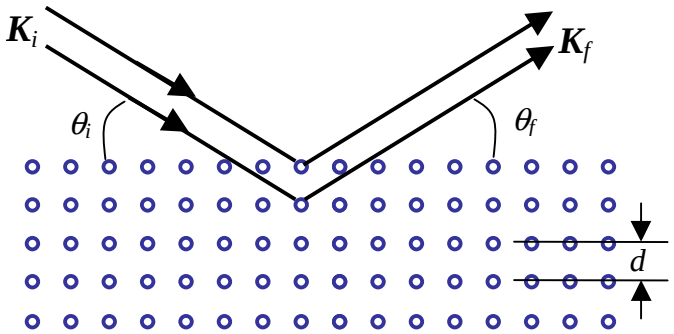

$$\theta_i = \theta_f = \theta$$
$$2d \sin\theta = n\lambda \qquad (2.5)$$

Figure 2.5: Schematic of x-ray diffraction from a crystal with an inter-planar distance *d*.

There are several advantages of using such technique:

1. It provides a completely non-destructive analysis;
2. A quantitative measurement of phase contents and texture orientation is possible;
3. There is minimal or no sample preparation requirements;

4. Ambient conditions can be used for analysis;

In the lab we used a Rigaku 18 kW rotating anode x-ray generator with Cu K_α radiation ($K_{\alpha 1}$ = 1.5406 Å, $K_{\alpha 2}$ = 1.5443 Å). The stepper motor resolution is 0.0025 degrees for θ and 2θ. The x-ray beam was focused at the center of a goniometer after passing through a graphite bent crystal monochromator. The entire system is computer-controlled with the necessary software for data collection and analysis. High angle x-ray diffraction was carried out using a four-circle (θ, 2θ, χ, ϕ) based goniometer. Before each run, a 2θ scan was done to align the beam and observe the profile of the incident beam. The sample was then mounted on the goniometer to do a rocking curve at $2\theta = 0$, ensuring that the sample was at the center of rotation. A rocking curve consists of setting the detector (2θ) to the Bragg peak position of certain plane and then rocking the sample by scanning θ to maximize the intensity of the Bragg peak. A θ-2θ was then performed through an angle range that was of interest.

Figure 2.6 shows the diagram of the x-ray setup in the lab. The slit widths before and after the sample are 1.2 mm and 0.6 mm, respectively, resulting in a 2θ FWHM of 0.2^0.

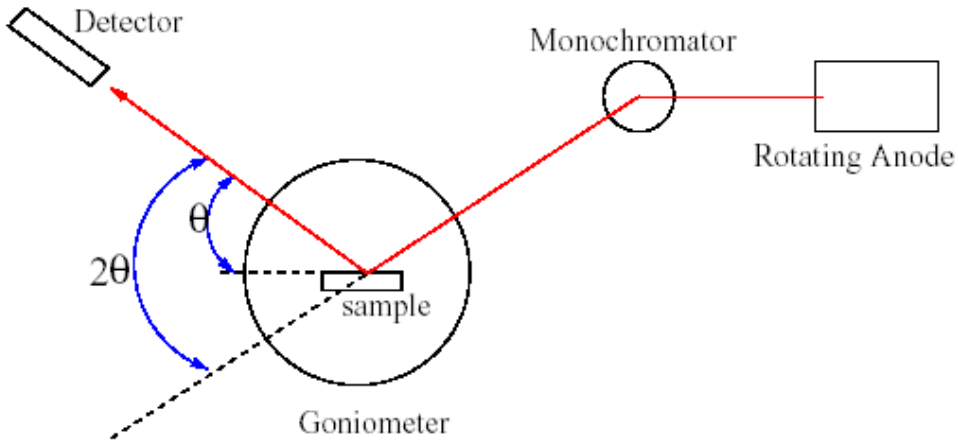

Figure 2.6: Top view of the x-ray setup. The path of the x-ray beam is shown in red. After Ref. 37.

Basic XRD measurements made on thin film samples include:

- Precise lattice constant measurements derived from θ - 2θ scans, which provide information about lattice mismatch between the film and the substrate and therefore is indicative of strain and stress. If the change of the wave vector, $\boldsymbol{K} = \boldsymbol{K}_f - \boldsymbol{K}_i$, is parallel to the surface normal, the scan is called an out-of-plane scan. If $\boldsymbol{K}$ has a component in the film plane, then it is called an in-plane scan. Out-of-plane scans probe the crystallinity of the film along the growth direction, whereas in-plane scans provide crystallinity information in the film plane, the symmetry of the film, the epitaxial relationship with the substrate, and the domain size in the film plane. In-plane scans (ϕ-scans) can be done by setting the incident beam and the detector at the Bragg condition of an in-plane peak and then rotating the sample about the surface normal, as shown in Figure 2.7.

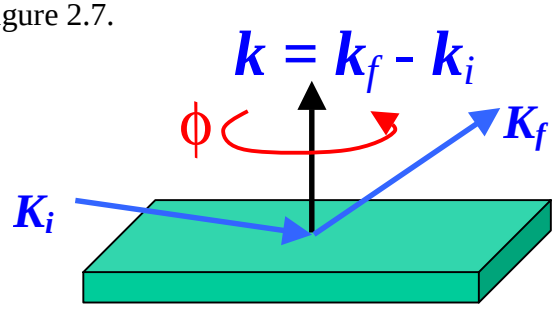

Figure 2.7: In-plane XRD with the sample rotating along the surface normal.

- Rocking curve measurements performed by rocking the sample at a fixed 2θ angle. In our setup 2θ is determined by the position of the detector, while θ is determined by the angle of the sample with respect to the incoming beam. The direction of the incoming beam is fixed. The rocking curve width is inversely proportional to the dislocation density and is therefore used as a gauge of the quality of the film.[38]

- Superlattice measurements in multilayered heteroepitaxial structures, which manifest as satellite peaks surrounding the main diffraction peak from the film. Film thickness and quality can be deduced from the data.[39]
- Glancing incidence x-ray reflectivity measurements, which will be described in more details below.

2.3.2 X-ray Reflectivity

Specular x-ray reflectivity, a technique complementary to x-ray diffraction, is now becoming a widely used tool for the characterization of thin-film and multilayer structures. When x-rays are incident at very low angles with respect to the plane of the film, the reflectivity is dominated by the optical scattering constants of the material. For a sufficiently smooth thin film 1 nm to 1000 nm thick deposited on a different material surface, the x-ray reflectivity has interference oscillations. By calculating the reflectivity based on optical scattering models, one can obtain accurate information about each film layer's thickness and interface roughness for either crystalline or amorphous materials.[40]

We used the same x-ray source as for high angle XRD to carry out the reflectivity measurement, although a different beam port was used. This arrangement allowed us to perform both high angle diffraction and reflectivity measurements using the same source without having to realign the system. For reflectivity measurements, the x-ray beam was focused at the center of a 29 cm, two-circle (θ, 2θ), computer-controlled goniometer which also used a bent graphite crystal monochromator, collimated to a width of ~ 0.02^0. The procedure is similar to the high angle diffraction measurements, except that there is no freedom of rotation for χ or ϕ. The slit widths before and after the sample are 0.2 mm and 0.3 mm, respectively, resulting in a 2θ

FWHM of 0.05^0. Prior to each scan, a 2θ scan was done to align the beam and observe the profile of the incident beam. The sample was then mounted on the goniometer to do a rocking curve at $2\theta = 0$, assuring that the sample is at the center of rotation. After that, rocking curve and θ-2θ scans were performed through an angle range around the specular condition with $\boldsymbol{K}$ perpendicular to the surface. Typical θ-2θ scans are between 0.5^0 and 8^0.

After the specular reflectivity was done, an off-specular reflectivity was measured with θ offset by ~ 0.1 degrees, which was then subtracted as the background from the specular part to get the real specular reflectivity. A recursive optical matrix model was used to model the real specular reflectivity to get each layer's thickness, as well as the interface roughness between each adjacent layer.[41]

For x-rays a material is characterized by its complex refractive index:

$$\tilde{n} = 1 - \frac{\rho_N r_e \lambda^2}{2\pi}(f_0 + \Delta f' - i\Delta f'') = n + ik, \qquad (2.6)$$

where ρ_N is the atomic density of the metal, r_e is the classical Thompson electron radius, 2.818 x 10^{-15} m, λ is the wavelength of the x-ray, f_0 is the atomic scattering power, $\Delta f'$ and $\Delta f''$ are the anomalous dispersion corrections for the atomic scattering power, $n = 1-\delta$ is the real part of the refractive index, where δ is often the order of 10^{-2}, and k is the imaginary part of the refractive index and is often close to zero. In the case of metal-dielectric layers, the interference between the reflected waves at each interface can not be neglected. For each interface, the electric field component above and below the interface has to be taken into account. Proper boundary conditions are then applied to each interface before getting the reflection matrix. To find the reflection matrix for the whole sample, all matrices are then multiplied. The model is then fit to

the data using Levenberg-Marquardt least squares minimization routine from Numerical Recipes[42] to get each layer's thickness, as well as the interface roughness.

2.4 Vibrating Sample Magnetometry (VSM)

Figure 2.8 shows the system diagram of the vibrating sample magnetometer (VSM) in the lab, which measures the magnetization of bulk materials as well as thin films along the magnetic field. From that measurement, information such as the saturation magnetization (M_S), coercivity (H_C), and the shift of the hysteresis loop (H_E) along the field direction can be extracted.

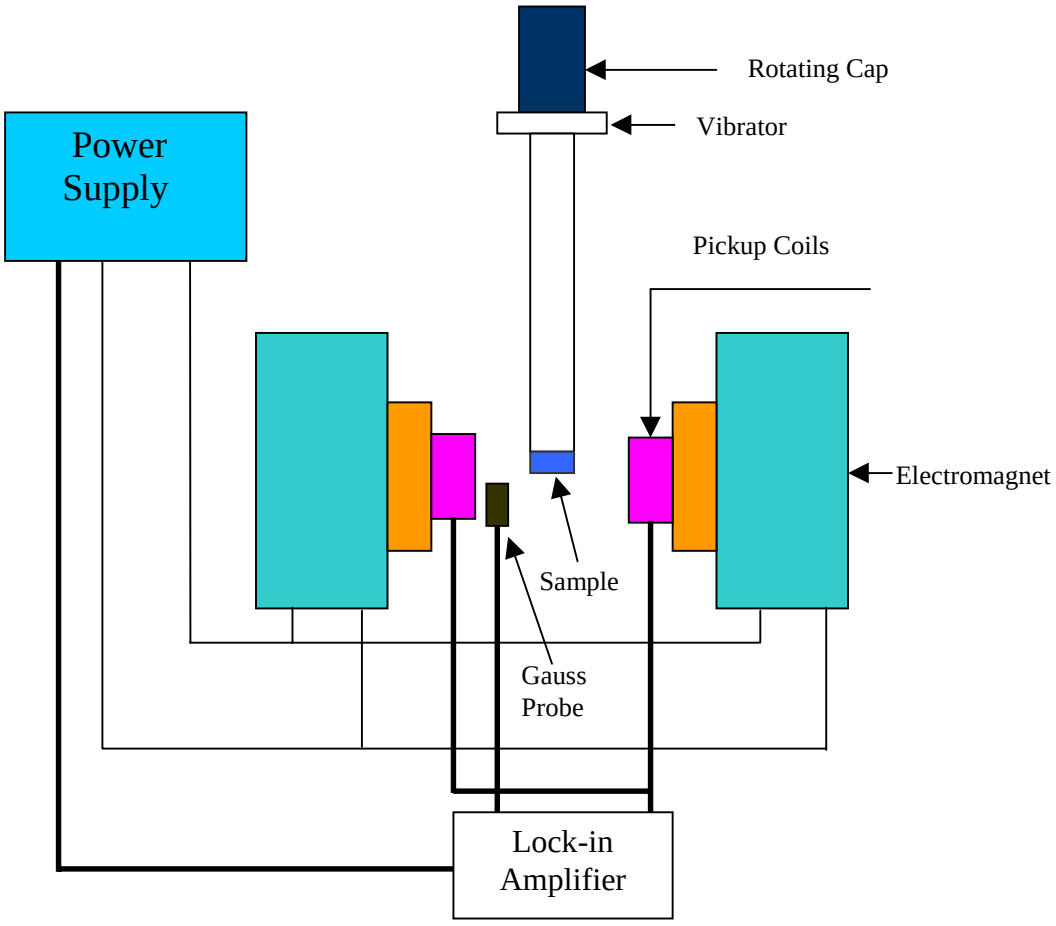

Figure 2.8: System diagram of the vibrating sample magnetometer. After Ref. 43.

The VSM operates by exploiting Faraday's Law of Induction that states a changing magnetic field will produce an electric field. The sample to be studied is placed in a DC magnetic field. If the sample is magnetic and the field is sufficiently large, this magnetic field will magnetize the sample by aligning the magnetic domains, or the individual magnetic spins, with the field. The sample is then mechanically vibrated at a frequency of 67 Hz in the vicinity of a set of pick-up coils, which induces a magnetic flux change and a voltage in the pick-up coils. That voltage is proportional to the magnetic moment of the sample:

$$V(t) = c\frac{d(f_i)}{dt}, \tag{2.7}$$

where $f_i(t)$ represents the changing flux in the pick-up coils caused by the vibrating magnetic sample.

The signal in the coils is typically very small and therefore extremely sensitive to noise sources. A transimpedance amplifier and a lock-in amplifier are therefore used to extract the small magnetic signal from the sample. The various components are connected to a computer. Using controlling and monitoring software, the system can measure the magnetization dependence of the sample on the strength of the applied magnetic field.

The major features of VSM in the lab are:

- $5 * 10^{-5}$ emu sensitivity;
- 11 kOe maximum field ;
- 360 degrees in-plane rotation with the resolution of better than 1 degree;
- Temperature range from 15 K to 350 K;
- Magnetic field resolution of better than 5 Oe;
- Full data storage, archival, and retrieval;

The temperature calibration in VSM was done by mounting a calibrated thermometer on the sample rod and then measuring the temperature at the thermometer as well as the temperature at the second stage of the cryostat.

2.5 SQUID Magnetometry

SQUID stands for Superconducting Quantum Interference Device, and is arguably the most sensitive magnetic flux detector known, with an equivalent energy sensitivity approaching the quantum limit. At the heart of the SQUID is a superconducting loop with a Josephson junction. Any flux change through the loop will lead to a change in phase difference across the junction, giving rise to a measurable voltage difference. If the current in the SQUID loop is kept to be constant then the magnitude of the voltage signal is directly proportional to the change in magnetic flux through the loop.[44]

Since the field of interest is often orders of magnitude smaller than power-line noise, or some other background noise, the SQUID in our lab uses the gradiometer configuration, which takes advantage of the mathematical form of the falloff of magnetic fields with distance from the source. In other words, superconducting pickup coils are arranged in a balanced second-derivative configuration designed to eliminate any unwanted signals from the superconducting magnet or other source of magnetic field, so that this arrangement actually measures d^2B/dz^2.

Chapter 3

Blocking Temperature and Exchange Bias in $Fe_xZn_{1-x}F_2$ / Co Bilayers

3.1 Introduction

The original model proposed by Meiklejohn and Bean qualitatively explained how H_E depends on the intrinsic magnetic properties by assuming an interface that is fully uncompensated, *i.e.* the surface of the antiferromagnet has a net magnetization, and therefore direct exchange AF/F interface coupling. This model fails to explain the existence of exchange bias observed in nominally fully compensated surfaces and surfaces with atomic-scale disorder that would tend to destroy H_E, nor does it reproduce the quantitative value of H_E, which is always much smaller than the value predicted by the theory.[22] Malozemoff later presented a model[45] that takes into account the likely randomness in exchange interactions at the interface, arising from surface roughness or chemical inhomogeneity on an atomic scale. Following an argument initially made by Imry and Ma,[46] the AF is assumed to break up into a domain state as local moments reorient to minimize the interfacial random-field energy. The exchange bias is then shown to be inversely proportional to the characteristic domain size L, *i.e.*, $H_E \propto 1/L$ with L the order of AF domain wall width $\pi\sqrt{A_A K_A}$, where A_A and K_A are the stiffness and anisotropy of the AF layer. This model calculates the correct order of magnitude to explain experimental data. The temperature dependence of H_E is expected to be ~ $(1-T/T_N)^{1/2}$ for uniaxial anisotropy and $(1-T/T_N)$ for cubic anisotropy based on Mean Field Theory. Following this logic, Miltényi *et al.*[28] attribute the exchange bias in Co / CoO bilayers to the exchange interaction between the net magnetization of finite-sized AF domains, bounded by domain walls perpendicular to the AF/F interface, with the F layer. This model predicts that a net magnetization of the AF layer establishes unidirectional anisotropy in the F layer parallel to the cooling field, so perpendicular

exchange coupling[27, 47, 48] across the AF/F interface is not required to produce exchange bias. Experimentally, this theory was tested by preparing dilute AF (DAF) $Co_{1-x}Mg_xO$ / 0.4 nm CoO / Co samples and measuring the exchange bias dependence on the dilution. It was found that H_E is enhanced by a factor of two to three after diluting the AF layer, when compared to pure CoO / Co bilayer samples, which was presumably due to the formation of domains in the DAF, facilitated by the non-magnetic impurities. As the dilution increases further, the antiferromagnetic order eventually breaks down, decreasing the interface coupling and therefore reducing the magnitude of H_E. Monte Carlo simulations, which consisted of a F monolayer (128 x 128 sites) exchange coupled to a 9 layers dilute AF film, qualitatively support that picture. [28] However, the H_E peak does not match what was observed experimentally, probably due to the fact that the interface layer on the DAF side was set to be 50% diluted in the simulations.

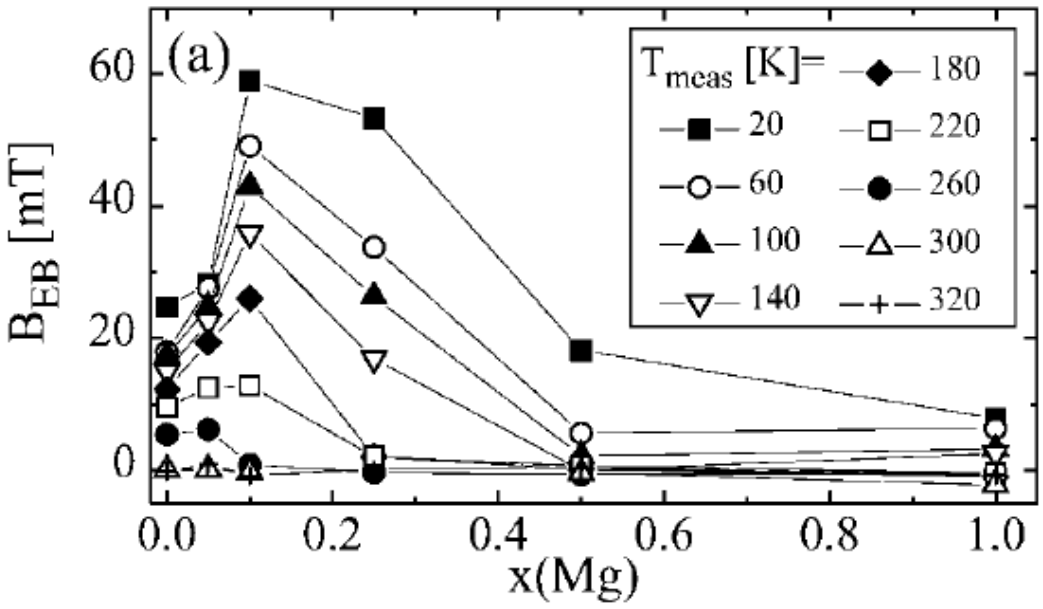

Figure 3.1: Exchange bias as a function of Mg concentration x in $Co_{1-x}Mg_xO$ at various temperatures. After Ref. 28.

The purpose of inserting the 0.4 nm pure CoO at the AF/F interface was to keep the defects away from the AF/F interface, regardless of the dilution. Therefore, different magnetic behaviors in different samples after field-cooling are directly related to the DAF volume part where defects substantially favor the formation of domains. Unfortunately, it is not known whether this interface layer can substantially alter the interface exchange interaction and thus complicate the experiment's interpretation. Another problem is that CoO, with its cubic crystal structure, has more than one possible antiferromagnetic arrangement, making a fundamental understanding of the effect more difficult.

The aim of the present work was to test the ideas of the domain-state model using a simpler AF system, and at the same time study the effects of a pure, thin AF layer placed at the AF/F interface. FeF_2 was chosen as the antiferromagnet because it has a simple body-centered-tetragonal (*bct*) structure[49] with $a = b = 0.469$ nm, and $c = 0.330$ nm. The ordering temperature of FeF_2 is 78.4 K (T_N).[50] The crystal structure, as well as the spin structure,[51] is shown in Figure 3.2. As can be seen, the Fe^{2+} ions at the corners order antiferromagnetically with the ion at the unit cell center. Also shown in Fig. 3.2 is the spin configurations on (110)-oriented FeF_2 surface, which turns out to be fully compensated, *i.e.*, the net moment is nominally zero. Another important issue is that FeF_2 has very strong uniaxial anisotropy along the [001] easy *c*-axis[52] ($K \sim 1.39 \times 10^8$ erg/cm^3, anisotropy field ~ 149 kOe), which is crucial to the exchange coupling at the interface, as we will discuss in Chapter 4. Hence, unlike CoO, FeF_2 has only one stable antiferromagnetic configuration at low temperatures.

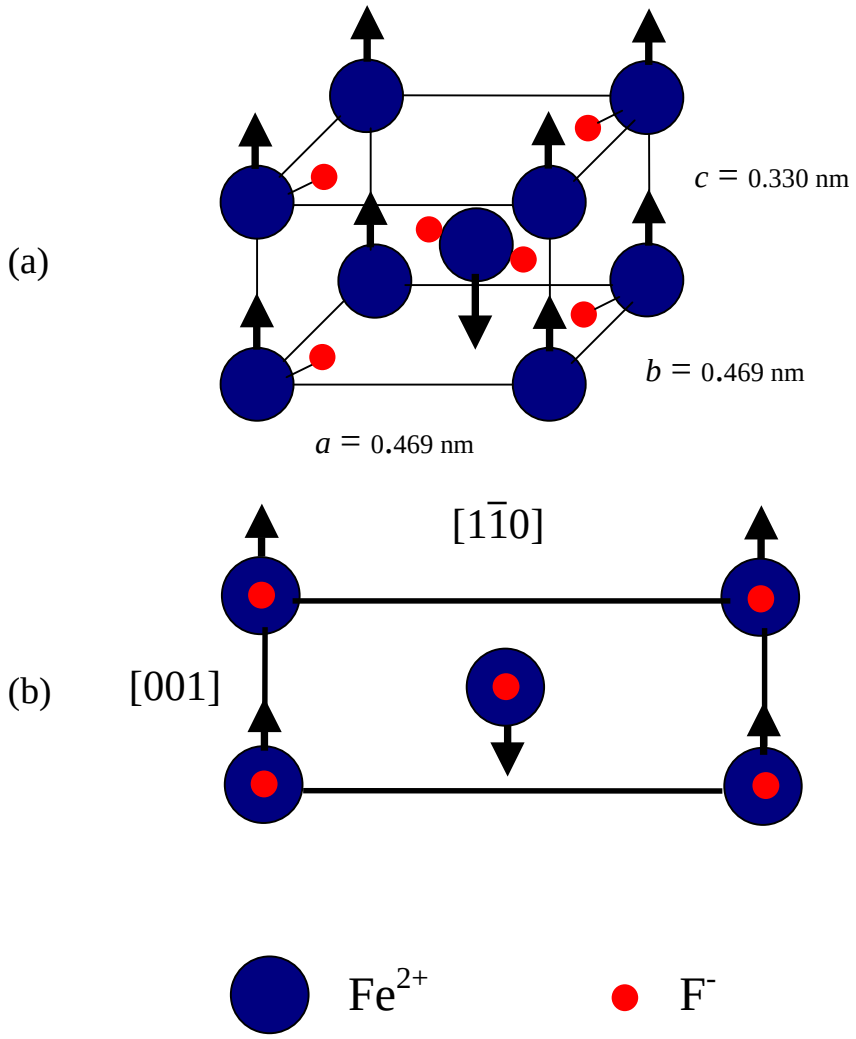

Figure 3.2: (a) Crystallographic unit cell of *bct* FeF_2 and spin structure; (b) Spin configurations on (110) surface of FeF_2. Notice the spins on (110) surface are fully compensated.

ZnF_2 was chosen to dilute the AF FeF_2 layer because it has the same *bct* rutile crystal structure[53] as FeF_2. The in-plane lattice mismatch between ZnF_2 and FeF_2 is 0.16% along the $[1\bar{1}0]$ direction and 5.25% along the [001] *c*-axis. Therefore, the dilute $Fe_xZn_{1-x}F_2$ AF possesses the same crystal structure as FeF_2, maintaining a strong magnetic uniaxial anisotropy along the *c*-axis. Unlike cubic antiferromagnets such as the transition metal oxides, $Fe_xZn_{1-x}F_2$ has a single axis (*c*-axis) along which the spins order at low temperature. Because of this, $Fe_xZn_{1-x}F_2$ is considered to be a realization of the random field Ising model (RFIM).[54]

In this chapter, the MBE growth of dilute $Fe_xZn_{1-x}F_2$ samples is described. The dependence of blocking temperature, T_B, on the concentration of Fe, *x*, in the dilute $Fe_xZn_{1-x}F_2$ layer as well as the dependence of interface energy ΔE on *x*, using Eq. (1.3) will also be presented.

3.2 Growth of $Fe_xZn_{1-x}F_2$ / Co Bilayers on MgO (100)

Magnesium oxide (MgO) is a non-magnetic crystal, which has a face-centered-cubic (*fcc*) NaCl crystal structure with lattice parameter a = 0.421 nm. The inter-planar distance along [110] direction is 0.298 nm, whereas FeF_2 has an inter-planar distance of 0.331 nm along $[1\bar{1}0]$ direction, which matches the *c*-value of FeF_2 (0.330 nm)[23]. The lattice mismatch between FeF_2 and MgO is 11.1% and 10.8% along $[1\bar{1}0]$ and [001] directions, respectively, with respect to MgO [110]. Also notice that 11 unit cells of (110) MgO corresponds to 10 unit cells of FeF_2, with an effective lattice mismatch of only 0.3%. This indicates that *c*-axis of FeF_2 could be parallel to MgO [110] or $[1\bar{1}0]$, resulting in FeF_2 to be twinned in the film plane when grown on MgO (100) substrate. This was confirmed by x-ray diffraction, in agreement with previous work.[55, 56]

In the experiments, we used MgO (100) crystals as the substrates to grow the $Fe_xZn_{1-x}F_2$ / Co bilayer samples via MBE. Before the substrate was loaded into the load-lock chamber, it was cleaned ultrasonically in methanol for 10 minutes to degrease the surface. After the transfer to the main chamber, the substrate was heated up to 494 ^{0}C in vacuum for 30 minutes, ensuring that the substrate is clean and smooth, which was monitored by RHEED. The substrate temperature was then set to 297 ^{0}C for the deposition of the dilute antiferromagnetic $Fe_xZn_{1-x}F_2$ layer. We waited at least 30 minutes at that temperature to make sure that the substrate was in thermal equilibrium. The pressure during the deposition of the AF layer and the Co layer was better than 2×10^{-7} Torr, with the major partial pressure contribution coming from fluorine gas.

Previous work[23] showed that the surface morphology of FeF_2 strongly depends on the growth temperature T_S for 200 ^{0}C < T_S < 300 ^{0}C. Interface root-mean-squared (rms) roughness values in the range ~ 0.5 – 5 nm were obtained. Figure 3.3 shows the atomic force microscopy (AFM) images (2 x 2 μm^2) of 80 nm thick FeF_2 films that were deposited at 297 ^{0}C, 345 ^{0}C, and 386 ^{0}C, respectively. All the AFM measurements were done in air at room temperature via Digital Instruments NanoScope II in the contact mode. The surface rms roughness values are 0.85, 0.97, and 1.96 nm, respectively. However, high angle XRD showed the full width at half maximum (110) peak did not have a strong dependence on growth temperature. Therefore, all DAF layers were grown at 297 ^{0}C on MgO.

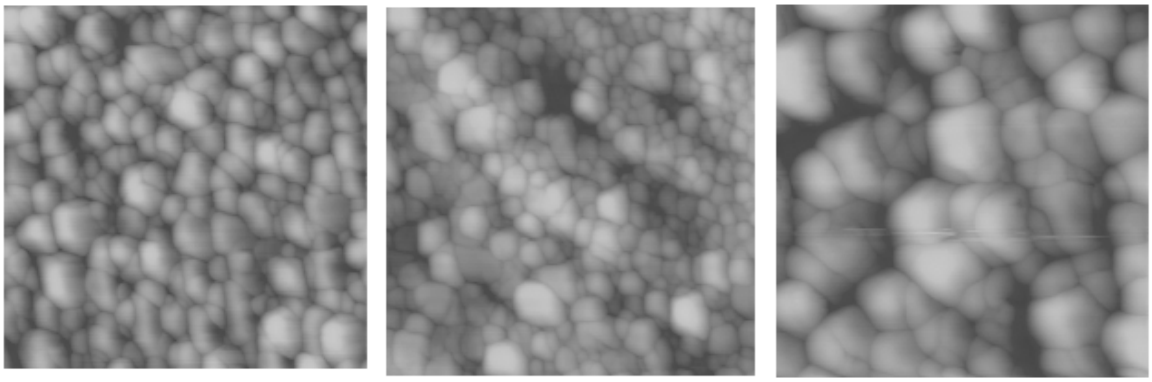

Figure 3.3: *Ex-situ* atomic force microscopy (AFM) images, 2 x 2 μm^2, at room temperature from 80 nm FeF_2 samples grown at (a) T_S = 297 ^{0}C; (b) T_S = 345 ^{0}C; and (c) T_S = 386 ^{0}C.

Two different sample structures (A, B) were employed in our experiments, which are shown in Figure 3.4. In both cases, a 68 nm thick dilute AF layer was first grown on the substrate. In structure A, an 18 nm Co layer, grown at T = 125 ^{0}C, was directly deposited on top of the DAF layer. The magnetic interface was therefore dependent on the concentration of Fe, x, in the dilute AF $Fe_xZn_{1-x}F_2$ layer. However, in structure B, a 1.0 nm pure antiferromagnetic (PAF) FeF_2 layer was deposited on top the DAF layer, followed by 18 nm Co layer. All samples were capped by 5 nm thick nonmagnetic MgF_2 films, which were grown at room temperature at a pressure of ~ 2 x 10^{-7} Torr, in order to prevent the oxidation of the samples.

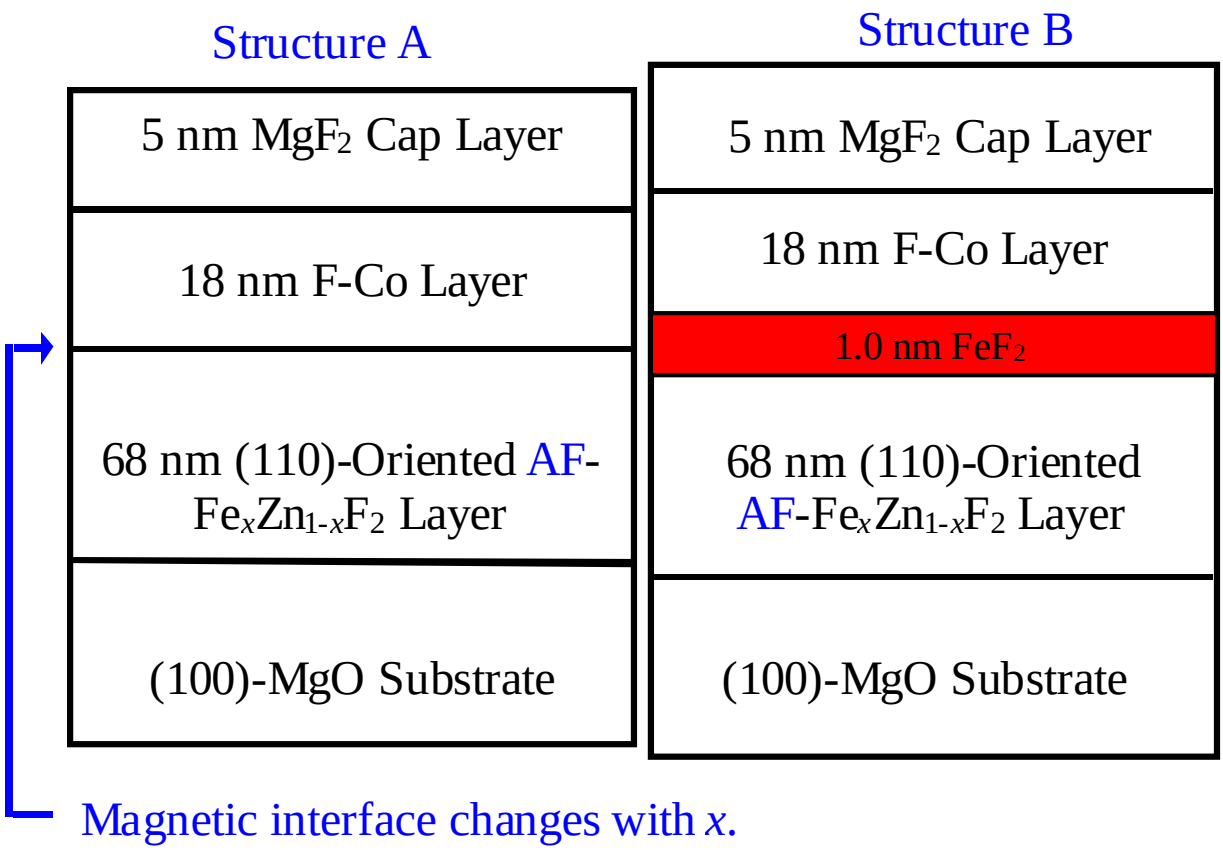

Figure 3.4: Two different sample structures (A, B) were used in this work, with (100) MgO as the substrates. The Co in structure A is in proximity with the dilute AF layer such that the magnetic interface depends on *x*. Structure B has a 1.0 nm pure FeF_2 between the Co layer and the dilute AF layer. Defects are in the volume part of the DAF, away from the F layer.

Figure 3.5 shows the out-of-plane XRD from a typical FeF_2 sample grown on MgO (100) at 297 ^{0}C. The presence of (110) and (220) diffraction peaks indicates that FeF_2 is (110)-oriented. X-ray diffraction from the pure MgO substrate indicates that these small peaks which are not labeled in Figure 3.5 are from the substrate. However, the in-plane ϕ-scan along FeF_2 (332), as shown in Figure 3.6, shows that FeF_2 has four peaks, separated by 90^0, which means that FeF_2 is twinned in the film plane. A four-fold symmetry from MgO (311) is also seen in

Figure 3.6, as expected from the cubic symmetry of the substrate. Combining the ϕ-scans of the film and the substrate, the epitaxial relationship between the film and the substrate was determined to be FeF_2 <001> || MgO <110>, and FeF_2 <$\bar{1}$10> || MgO <$\bar{1}$10>, which is shown in Figure 3.7. The FWHM values of the FeF_2 (110) and (220) peaks are 0.11^0 and 0.18^0, respectively.

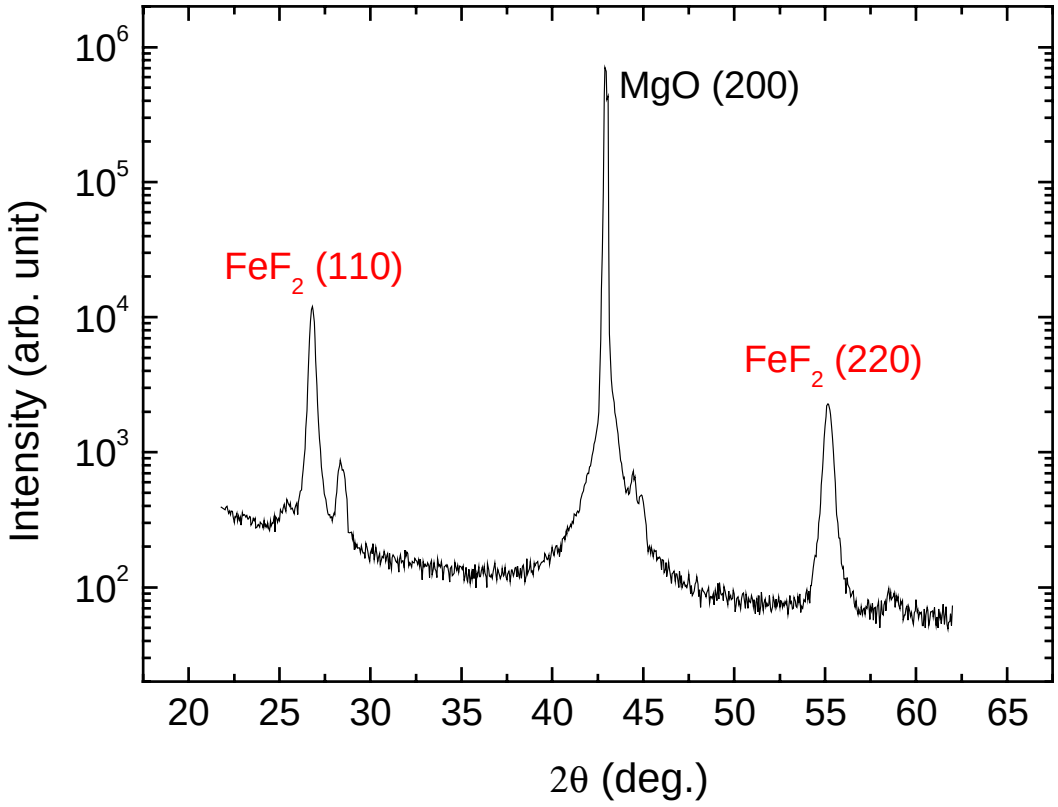

Figure 3.5: Out-of-plane x-ray diffraction from a FeF_2 film grown on MgO (100) substrate. Notice that only FeF_2 (110) and (220) peaks are present, indicating that FeF_2 is (110)-oriented. Unlabeled small peaks are from the substrate.

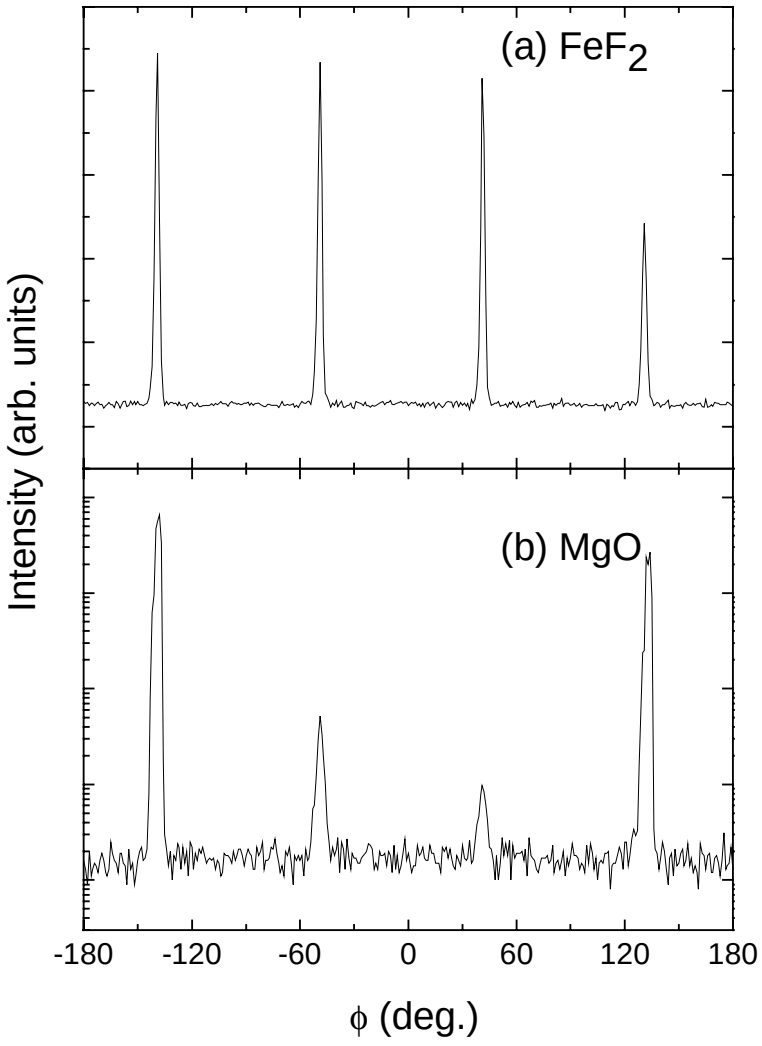

Figure 3.6: In-plane XRD scans from (a) FeF_2 (332) and (b) MgO (311). These peaks are separated by 90^0, indicating that the FeF_2 layer formed perpendicular twins in the film plane.

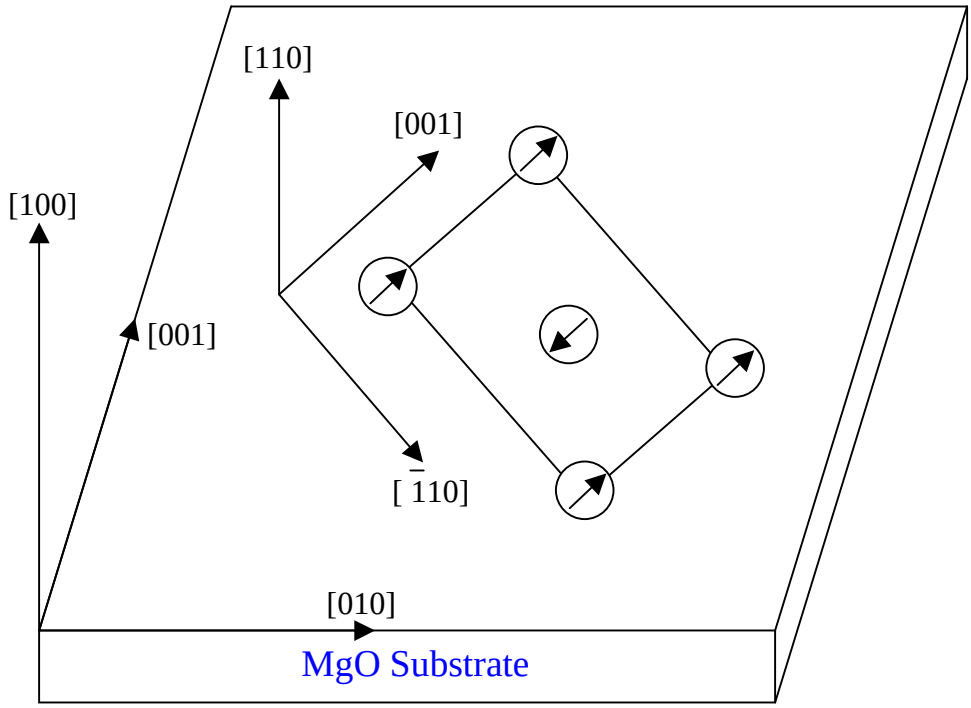

Figure 3.7: Orientation of the FeF_2 surface unit cell with respect to the MgO (100) substrate. The spin directions of the Fe^{2+} ions at low temperatures ($T << T_N$) are also shown in the figure, as indicated by the arrows.

Figure 3.8 (a) shows the *in-situ* RHEED pattern of a pure FeF_2 film. The electrons were incident along the *c*-axis of one of the FeF_2 domains and perpendicular to the other. The in-plane lattice parameter determined by the RHEED pattern is 0.331 nm, which agrees very well with the lattice parameter of the bulk FeF_2. The streaky pattern indicated that the film was smooth and epitaxial.

Figure 3.9 shows the x-ray reflectivity data from two different samples, MgO (100) / FeF_2 / Co / MgF_2-cap and MgO (100) / $Fe_{0.84}Zn_{0.16}F_2$ / 1.0 nm FeF_2 / Co / MgF_2-cap, as well as the fitting using the standard optical model.[41] The interface roughness of these two samples between the AF layer and the Co layer is 0.21 nm and 0.66 nm, respectively. All samples showed a similar reflectivity profile with interface roughness between 0.2 nm and 0.9 nm, which primarily depended on the roughness of the substrate.

(a)

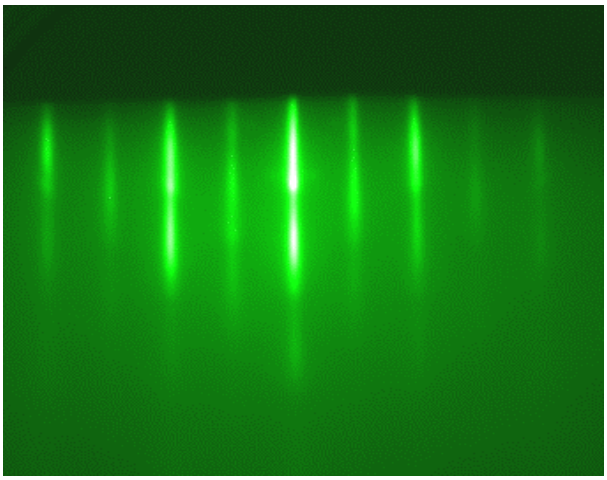

(b)

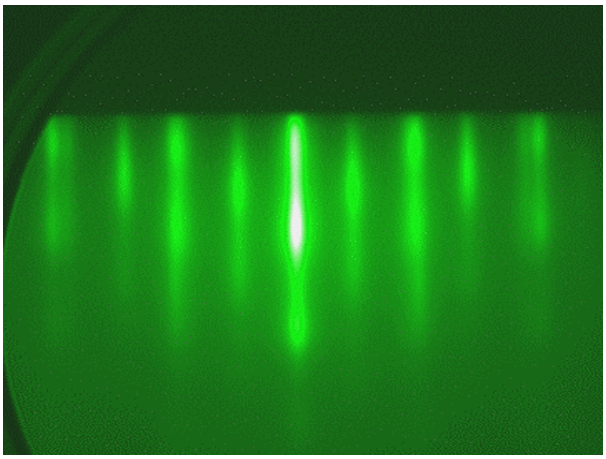

(c)

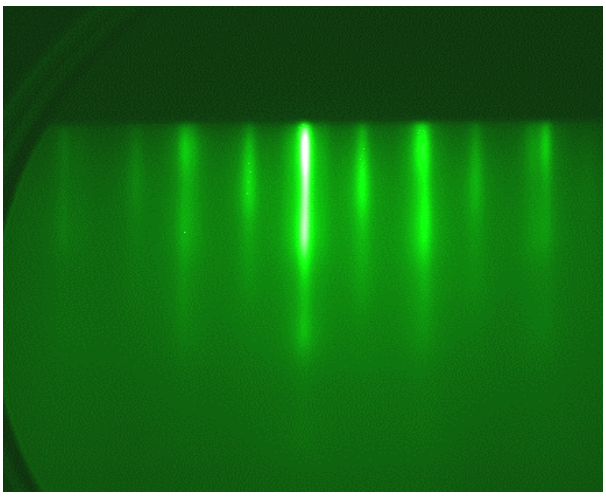

Figure 3.8: RHEED patterns from samples with different Fe concentration in $Fe_xZn_{1-x}F_2$. (a) Pure FeF_2; (b) $Fe_{0.43}Zn_{0.57}F_2$; (c) Pure ZnF_2;

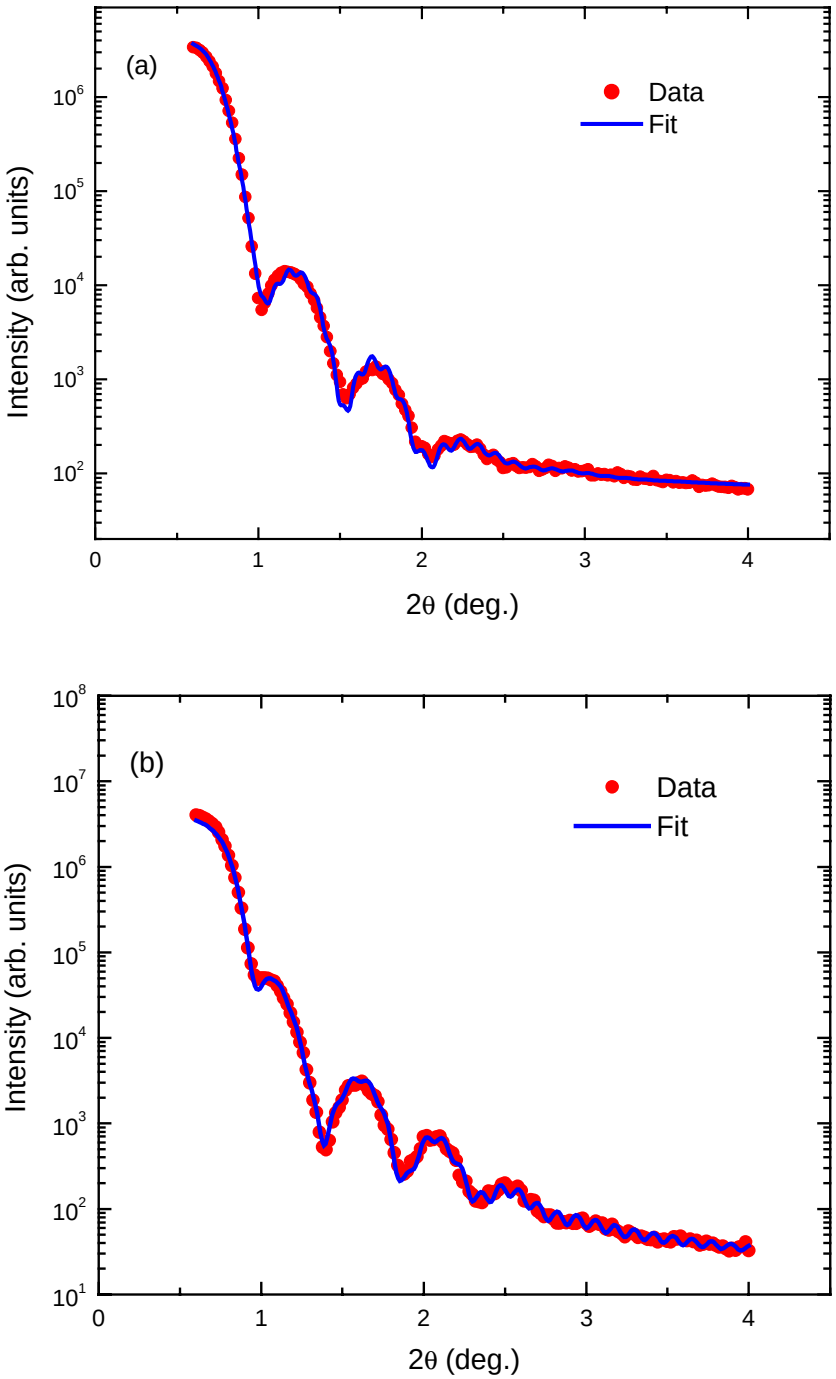

Figure 3.9: X-ray reflectivity data (in dots) and fitting (in lines) using the standard optical model.
(a) MgO (100) / FeF_2 / Co / MgF_2-cap, interface roughness = 0.21 nm.
(b) MgO (100) / $Fe_{0.84}Zn_{0.16}F_2$ / 1.0 nm FeF_2 / Co / MgF_2-cap, interface roughness = 0.66 nm.

Figure 3.10 shows the high angle XRD patterns of the pure FeF_2 sample in more detail, both out-of-plane and in-plane scans. Solid dots correspond to the data, whereas the lines are the fits to the data, using two Gaussian-typed functions with the intensity ratio of 2:1, due to the fact that the intensity ratio of Cu $K_{\alpha 1}$ to $K_{\alpha 2}$ is 2:1. The fitting function has the following form, where x_{c1} and x_{c2} are in the units of degrees:

$$y = y_0 + \frac{A_1}{w*\sqrt{\pi/2}} * e^{-2(\frac{x-x_{c1}}{w})^2} + \frac{1}{2} * \frac{A_1}{w*\sqrt{\pi/2}} * e^{-2(\frac{x-x_{c2}}{w})^2}, \quad (3.1)$$

$$x_{c2} = 2*\frac{180}{\pi} * a\sin(\frac{1.5443}{1.5406} * \sin(\frac{x_{c1}*\pi}{2*180})), \quad (3.2)$$

where x_{ci} (i = 1, 2) is the peak position for $K_{\alpha 1}$ or $K_{\alpha 2}$, y_0 is the offset, w is $\sqrt{2}$ times larger than the FWHM of the diffraction peaks. The relationship between x_{c1} and x_{c2} is due to the Bragg conditions. Based on that fitting, one can extract the peak positions for both out-of-plane and in-plane scans, as well as the width of each Bragg peak. With that information, one can then calculate the lattice parameters by using Bragg equation (2.5). The structural coherence length (L) can be estimated using Scherrer's equation,[57] *i.e*,

$$L = \frac{0.94\lambda}{B(2\theta)\cos\theta}, \quad (3.3)$$

where λ is the x-ray wavelength, θ is the Bragg diffraction angle, and $B(2\theta)$ is the full width at half maximum of the 2θ peak in radians.

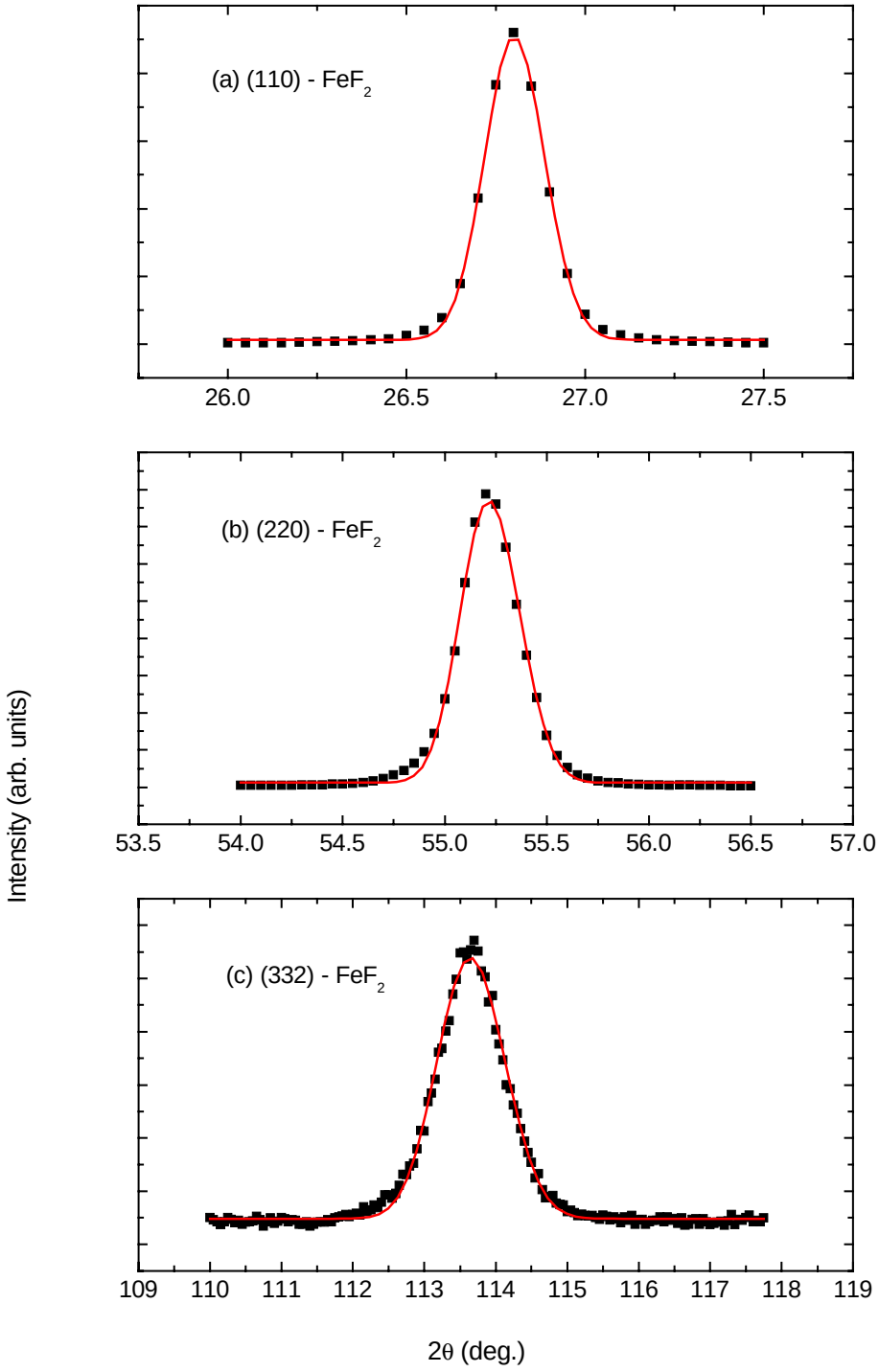

Figure 3.10: X-ray diffraction from a FeF_2 film. (a) (110) plane; (b) (220) plane; (c) (332) plane. Data are in dots. Lines are the fitting using Eqs. (3.1) and (3.2).

When we performed high angle x-ray diffraction the sample may not be exactly at the center of rotation, as shown in Figure 3.11. In our experiments it was important to accurately determine the lattice parameter in order to calculate the Fe concentration in the DAF, so this effect was taken into account as follows. Suppose the sample rotates at point *B*, which has a distance *h* to the real center of rotation, point *A*. The distance from *A* to the detector is *l*.

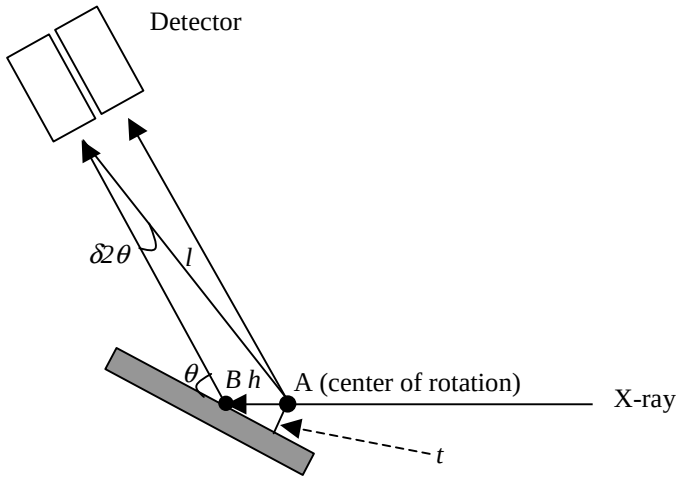

Figure 3.11: Top view of high angle x-ray diffraction with sample rotating around point *B*, which has a distance *h* from the real point of rotation *A*.

When Bragg condition is satisfied, we have $2d\sin\theta = n\lambda,$ where *d* is the lattice parameter and λ is the x-ray wavelength. Taking a partial derivative of this equation, we have:

We also have:

$$\delta d = -\frac{d\cos\theta\delta\theta}{\sin\theta}, \tag{3.4}$$

$$\frac{l}{\sin(180-2\theta)} = \frac{h}{\sin(\delta 2\theta)}. \tag{3.5}$$

If we define:

$$h\cos\theta = t, \tag{3.6}$$

and taking into account the fact that $\delta 2\theta$ is small, then combining Eqs. (3.4) – (3.6) we obtain:

$$\delta d = -\frac{d\cos\theta\delta\theta}{\sin\theta} = -\frac{td\cos^2\theta}{l\sin\theta}, \tag{3.7}$$

Suppose the measured lattice parameter is d_{eff} after fitting the θ-2θ scan using Eqs. (3.1) and (3.2), and the real value is d, then:

$$\begin{aligned} d_{eff} &= d + \delta d \\ &= d - \frac{td\cos^2\theta}{l\sin\theta} \\ &= d + (-\frac{td}{l})(\frac{\cos^2\theta}{\sin\theta}). \end{aligned} \tag{3.8}$$

Experimentally, we measured the (110) and (220) diffraction lines from the AF layer, and then plotted d_{eff} as a function of $\cos^2\theta/\sin\theta$, which gave us the lattice parameter d, as well as the slope, $k = -td/l$. The lattice parameter a can then be calculated from the d value. We then did an in-plane scan along the (332) peak. The c value of the DAF layer can be calculated by plugging $2\theta/2$ at (332) peak and the slope k into Eq. (3.8).

Applying such procedure to the FeF_2 film with XRD shown in Figure 3.10, we determined the lattice parameters of the pure FeF_2 film to be:

$$a_{FeF_2} = 4.704\,\text{Å}, \qquad c_{FeF_2} = 3.308\,\text{Å}.$$

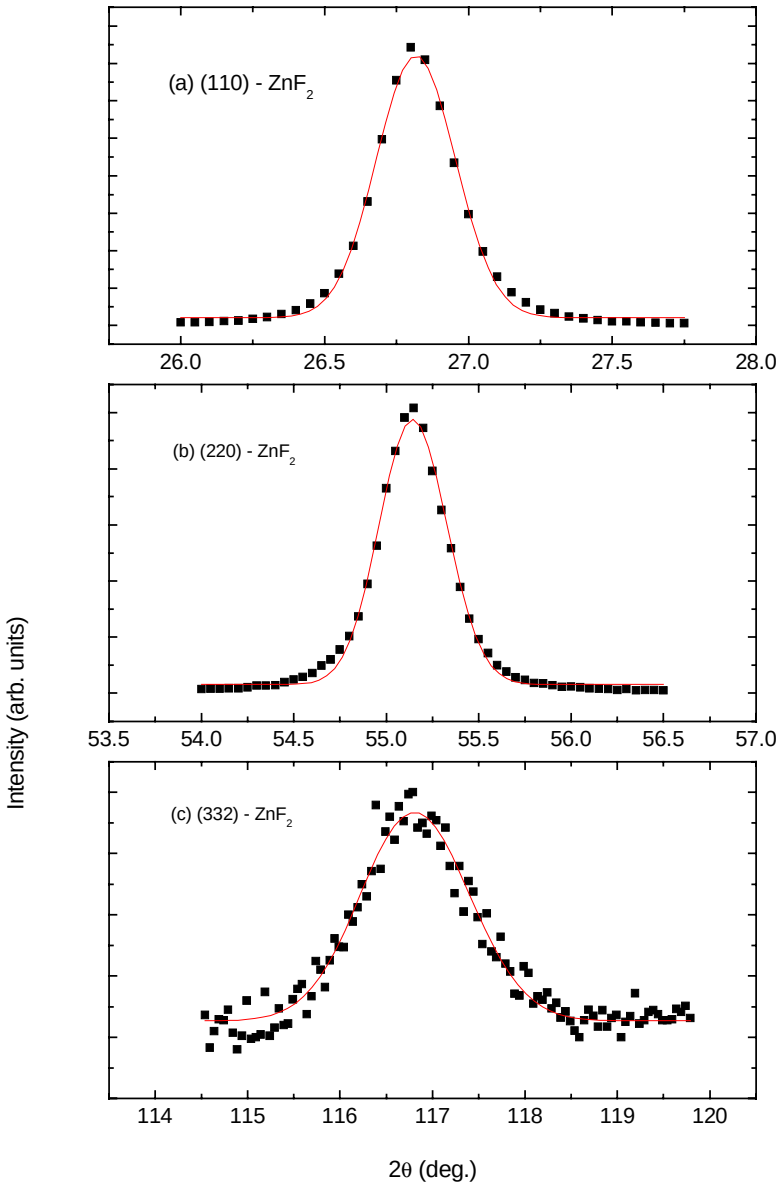

Figure 3.12: X-ray diffraction from a ZnF_2 film. (a) (110) plane; (b) (220) plane; (c) (332) plane. Data are in dots. Lines are the fitting using Eqs. (3.1) and (3.2).

Figure 3.12 shows the out-of-plane and in-plane XRD scans of the pure ZnF_2 sample, 68 nm thick, grown on MgO (100) substrate at 297 ^{0}C. By fitting the data using Eqs. (3.1), (3.2), and (3.8), the lattice parameters were determined to be:

$$a_{ZnF_2} = 4.721 \text{ Å}, \qquad c_{ZnF_2} = 3.139 \text{ Å}.$$

The RHEED pattern of a pure ZnF_2 sample is shown in Figure 3.8(c), which also has a four-fold symmetry, as confirmed by ϕ-scan along the (332) peak. The streaky pattern indicates that ZnF_2 is also smooth when grown on MgO (100) substrate.

In order to determine the Fe concentration x in $Fe_xZn_{1-x}F_2$ films, we performed an out-of-plane θ-2θ XRD scan first to determine the lattice constant a of the dilute AF layer, followed by the ϕ-scan of the *bct* (332) peak to determine the lattice constant c of the dilute AF layer. Based on these values of lattice parameters, the Fe concentration x was then calculated using Vegard's Law:

$$x = \frac{c(Fe_xZn_{1-x}F_2) - c(ZnF_2)}{c(FeF_2) - c(ZnF_2)}, \tag{3.9}$$

where $c(Fe_xZn_{1-x}F_2)$, $c(FeF_2)$, and $c(ZnF_2)$ are the c values of the $Fe_xZn_{1-x}F_2$ layer, pure FeF_2 layer and pure ZnF_2 layer, respectively. This method yields an uncertainty in x of ±0.01.

A typical RHEED pattern of a dilute AF layer with x = 0.43 is shown in Figure 3.8(b), which is very similar to that of the pure FeF_2 and ZnF_2 samples. This indicates that the smooth interface can be well maintained in all DAF/Co bilayer samples, independent of the Fe concentration in the AF $Fe_xZn_{1-x}F_2$ layers.

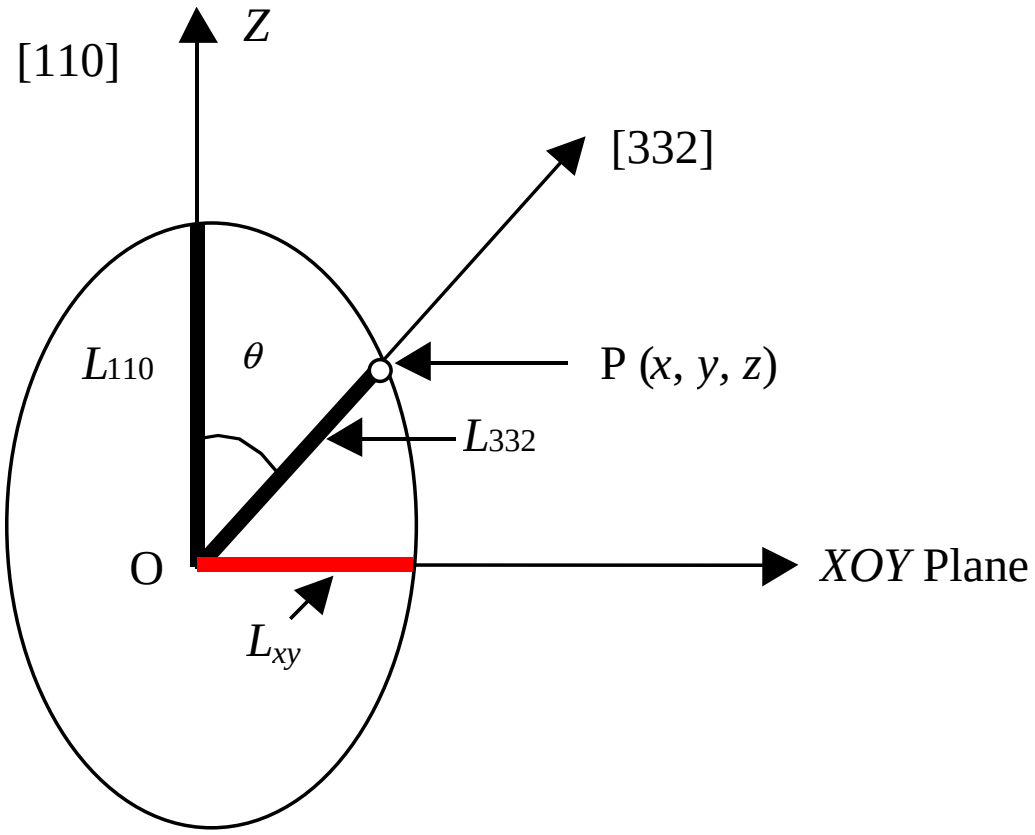

Figure 3.13: Coherence length in the film plane.

Assuming the AF domains are ellipsoid-shaped, as illustrated in Figure 3.13, L_{110} is the coherence length along [110] direction, and L_{332} is the coherence length along [332] direction, which can be obtained by doing the out-of-plane and in-plane (332) XRD and then using Eq. (3.3). The following equation holds for any point on the surface of the ellipsoid where L_{xy} is the crystallographic domain size in the film plane:

$$\frac{z^2}{L_{110}^{\ 2}} + \frac{x^2 + y^2}{L_{xy}^{\ 2}} = 1. \tag{3.10}$$

The angle θ between (110) plane and (332) plane is 33.85^0. If we look particularly at the point P, which is the intersection between [332] direction and the ellipsoid, then:

$$\begin{aligned} x^2 + y^2 &= L^2_{332} \sin^2 \theta, \\ z &= L_{332} \cos\theta. \end{aligned} \tag{3.11}$$

Putting these equations together, we can get the in-plane crystallographic domain size:

$$L_{xy} = \sqrt{\frac{L^2_{110} L^2_{332} \sin^2 \theta}{L^2_{110} - L^2_{332} \cos^2 \theta}}. \tag{3.12}$$

Combining the x-ray diffraction data with Eqs. (3.3) and (3.12), the crystallographic domain size in the film plane was determined to be between 6 nm and 10 nm, or approximately 20 - 30 unit cells.

3.3 Temperature Dependence of H_E

It is now known that the largest exchange bias in pure FeF_2 / Fe bilayers occurs in (110)-FeF_2 twinned samples with two perpendicular in-plane (001) domains.[58] In order to characterize the magnetic properties of Co on dilute $Fe_xZn_{1-x}F_2$ layers, particularly the exchange bias dependence on the concentration of Fe, x, in $Fe_xZn_{1-x}F_2$ with different sample structure A or B, we performed SQUID magnetometry in the 2.5 K – 90 K temperature range. Samples were cooled from 90 K through the Néel temperature of the samples to 2.5 K in a magnetic field of 2 kOe, which is large enough to saturate the F layer. The cooling field (H_{CF}) was parallel to the in-plane MgO [001] direction, *i.e.*, parallel to the bisector of the twinned domains, which is known to result in a magnetic easy axis because of the frustration of the perpendicular coupling due to the twinning. H_E was determined from hysteresis loops measured at different temperatures, from which the blocking temperature T_B can be determined.

Figure 3.14 shows the temperature dependence of H_E from a pure FeF_2 / Co bilayer sample, as well as a hysteresis loop at T = 2.5 K, which was normalized to the saturation magnetization M_S of the Co layer. It can be seen that T_B is very close to T_N of FeF_2. Figures 3.15 and 3.16 show the T_B dependence of these two types of samples on x. The blocking temperatures are plotted in Figure 3.17. The dotted line in the graph is the T_N of bulk $Fe_xZn_{1-x}F_2$ in the form of $T_N(x) = T_N(1.0)x$, where $T_N(1.0)$ = 78.4 K,[59] the T_N of pure FeF_2. This linear dependence is known to be highly accurate in $Fe_xZn_{1-x}F_2$ single crystals for $x > 0.25$,[59] which is the percolation threshold in $Fe_xZn_{1-x}F_2$.[60] Notice that H_E is saturated at T = 2.5 K, which was also true for all samples with $x > 0.25$. The insertion of a 1.0 nm pure FeF_2 layer between the AF layer and the Co layer does not significantly alter T_B for $x > 0.25$. The good agreement between the data and the dotted line in this range indicates that T_B is likely to be governed by the ordering temperature of the underlying AF layer.

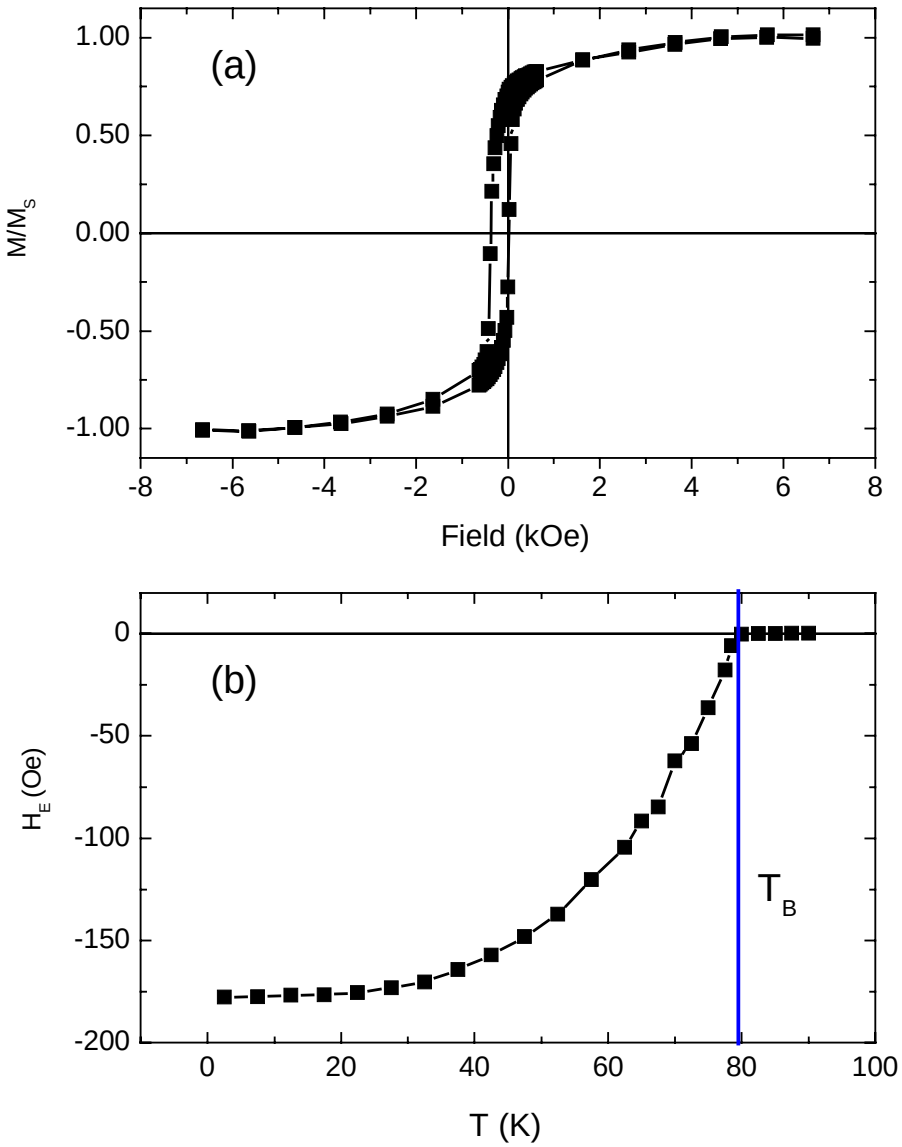

Figure 3.14: (a) Hysteresis loop at T = 2.5 K and (b) temperature dependence of H_E of the FeF_2 / Co bilayer sample. Lines are the guides to the eye.

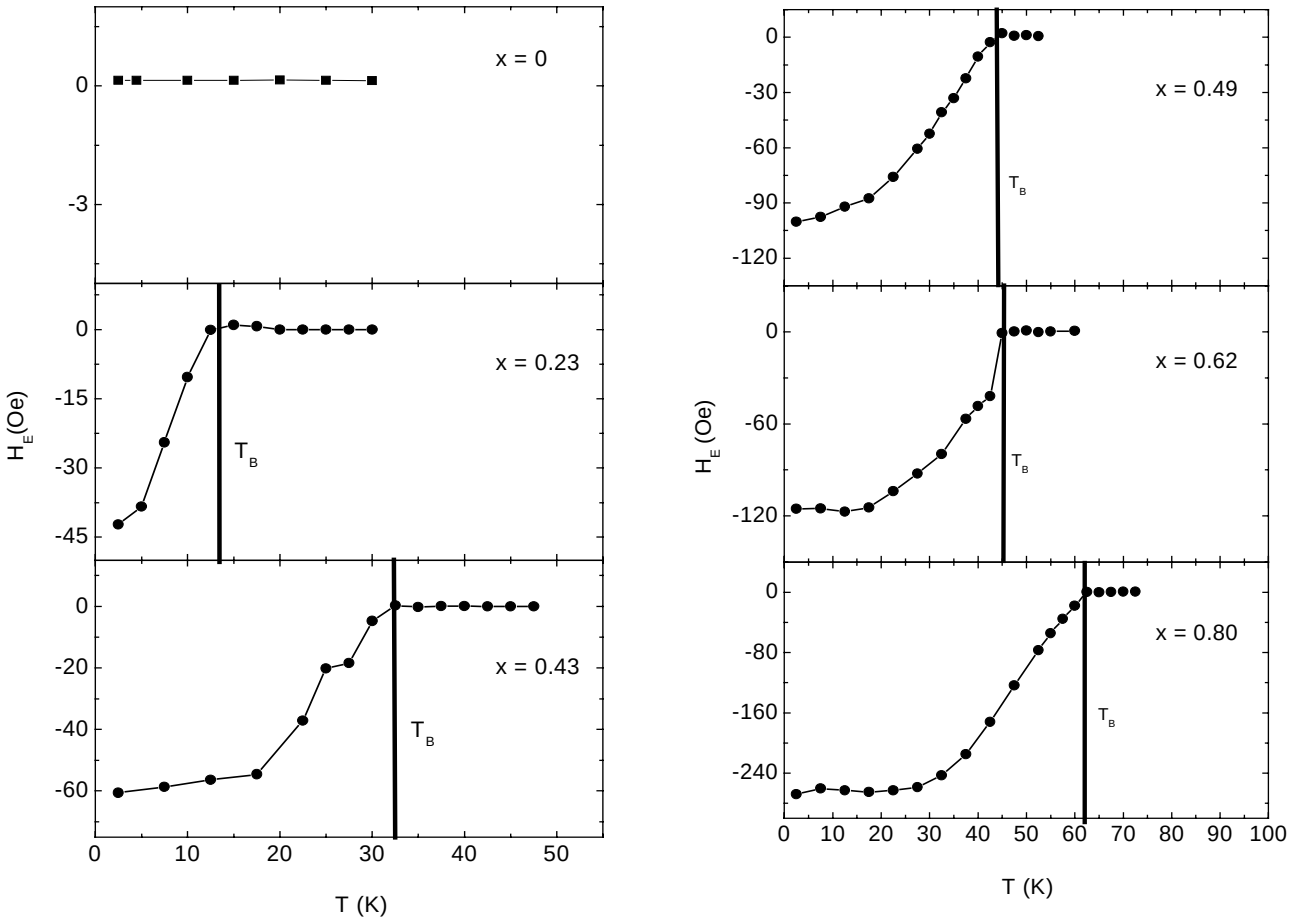

Figure 3.15: Exchange bias dependence on Fe concentration in $Fe_xZn_{1-x}F_2$ at various temperatures, in which Co was in proximity with FeF_2 layer. Lines are the guides to the eye.

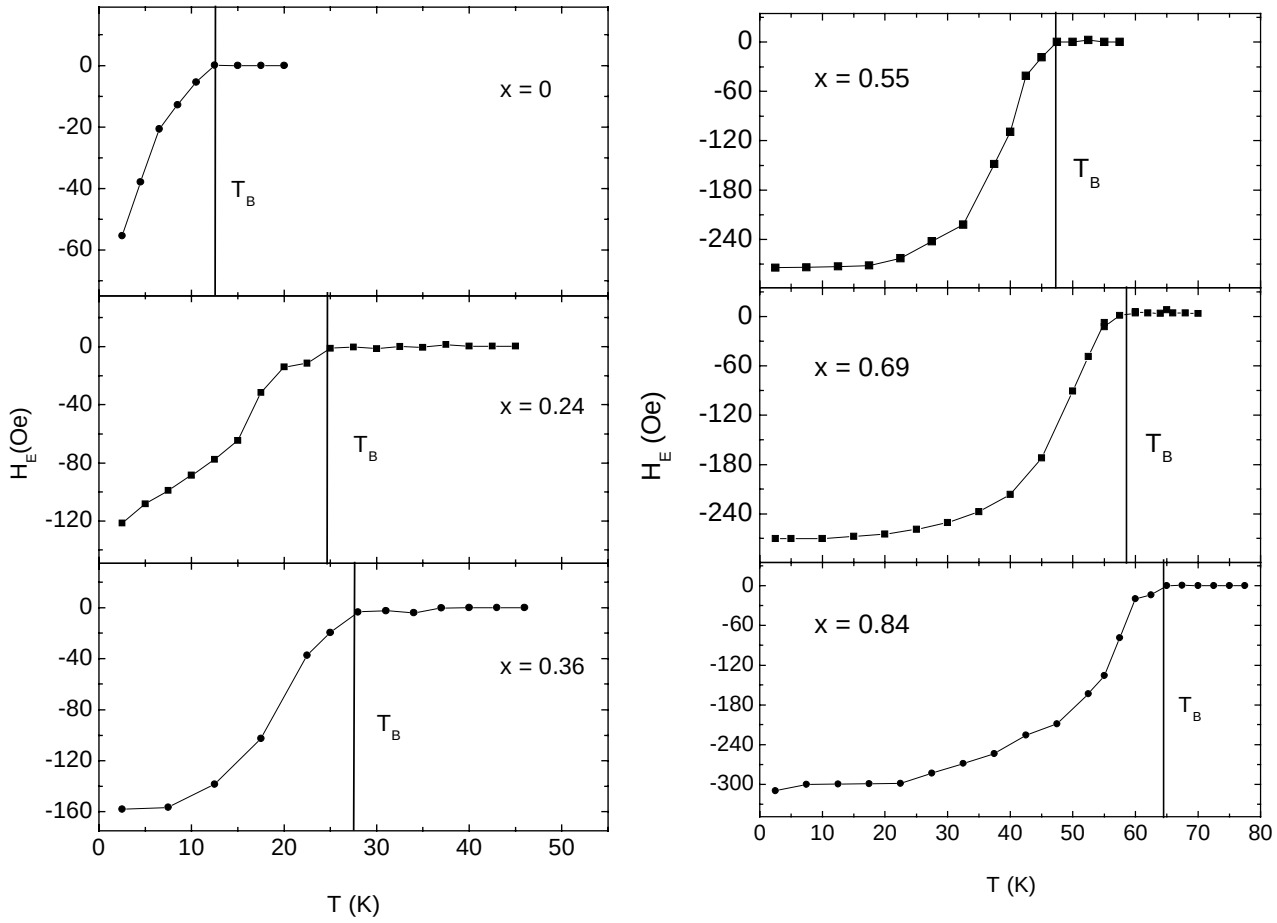

Figure 3.16: Exchange bias dependence on Fe concentration in $Fe_xZn_{1-x}F_2$ at various temperatures, in which there was a 1.0 nm pure FeF_2 interface layer between the AF layer and the Co layer. Lines are the guides to the eye.

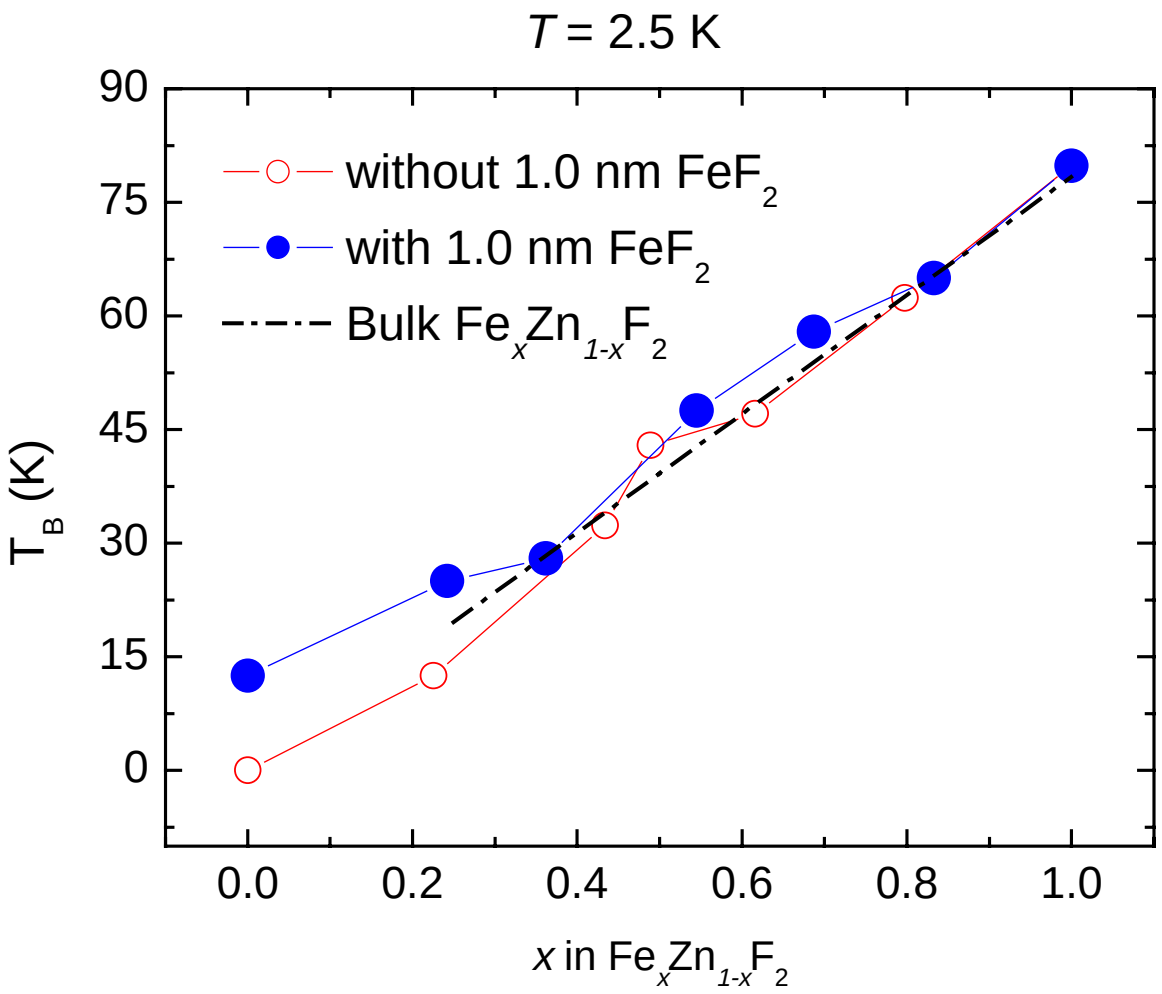

Figure 3.17: Blocking temperature as a function of the concentration of Fe in the dilute antiferromagnetic $Fe_xZn_{1-x}F_2$ layers. Open and solid circles represent samples that do not and do have the 1.0 nm FeF_2 at the interface, respectively. Dotted line is the T_N dependence on x in bulk $Fe_xZn_{1-x}F_2$ for $x > 0.25$.

3.4 Interface Energy

Figure 3.18 shows the dependence of interface energy per unit area (ΔE) of those two types of samples on the concentration of Fe in the dilute $Fe_xZn_{1-x}F_2$ layers, using equation (1.3), *i.e.*, $\Delta E = M_F t_F H_E$, where M_F and t_F are the saturation magnetization and the thickness of the ferromagnetic layers, respectively. It can be seen that ΔE increases for $x \cong 0.8$ in samples with and without the 1.0 nm pure interface layer when compared with the pure FeF_2 / Co system (x = 1.0). However, this effect is more accentuated for the samples with the pure FeF_2 interface layer. Notice that this enhancement is not explained by the dilution at the interface, as demonstrated by the triangles in the figure, which are $\Delta E/x$ for the samples without the pure interface layer. This indicates that the thin, pure antiferromagnetic layer plays a crucial role in enhancing the ΔE. This may also happen in the case of $Co_xMg_{1-x}O$, although to our knowledge this has not been investigated.

It is well known that a DAF forms a metastable domain state upon field-cooling through its T_N, resulting in a net moment.[61] The orientation and magnitude of that moment are controlled by the competition between the exchange interaction with the adjacent F layer and the adaptation of the interface spin configuration to the underlying AF domain structure. An antiferromagnet with strong uniaxial magnetic anisotropy, such as FeF_2, will lead to a compromise between complete interface and bulk adaptation. In the case of dilution, nonmagnetic impurities facilitated the formation of the domains, breaking the symmetry of the two sublattices, resulting in the net moment coupled to the external field, as sketched in Figure 3.19. The enhancement of H_E after the insertion of 1.0 nm FeF_2 at the AF/F interface is possibly related to the small thickness of that pure interface layer which breaks up into small antiferromagnetic domains, causing the domains in the alloy to be slightly smaller than they would otherwise be.

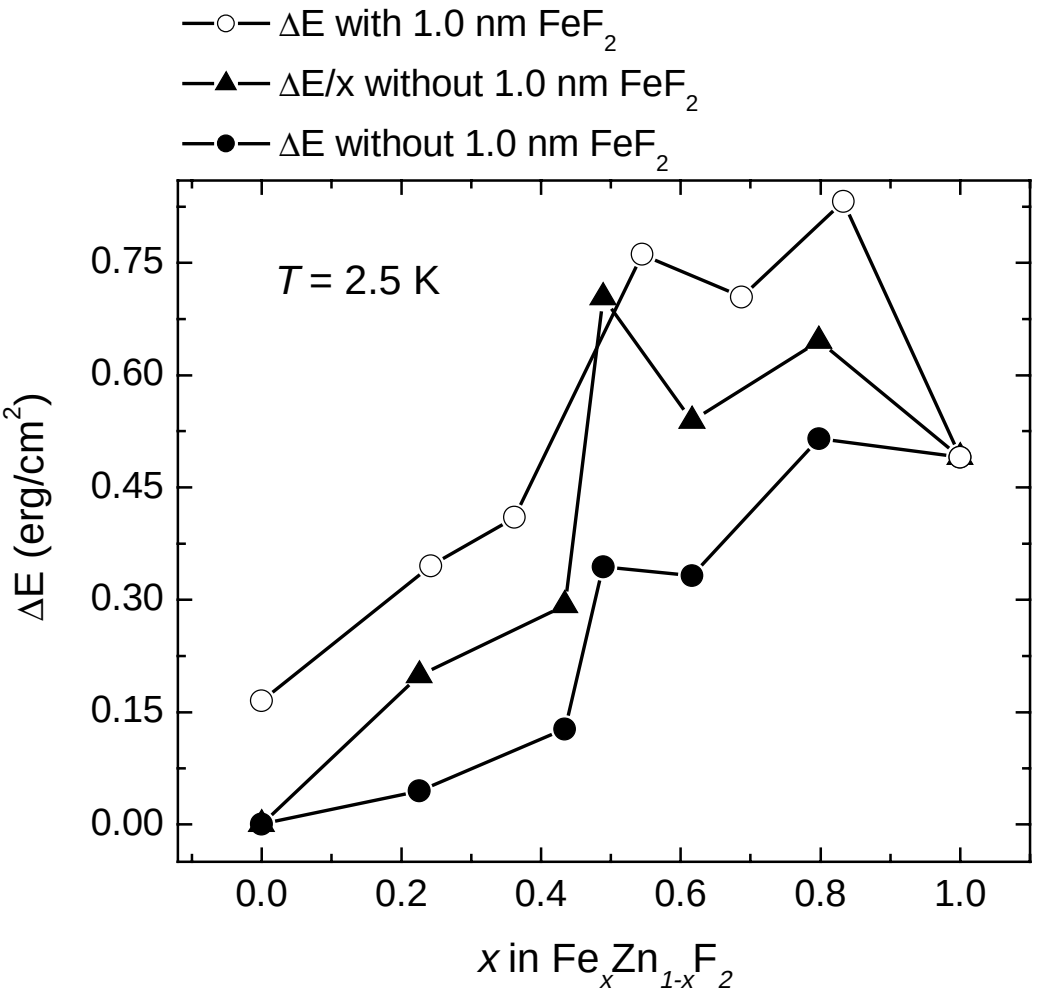

Figure 3.18: Interface energy per unit area ΔE as a function of Fe concentration x in the DAF layers. $\Delta E = M_F\, t_F\, H_E$, where M_S and t_F are the saturation magnetization and the thickness of the Co layer, H_E is the exchange bias at T = 2.5 K.

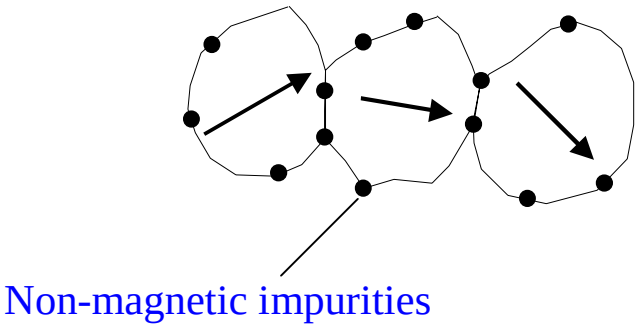

Figure 3.19: Schematic of the formation of domains around the non-magnetic impurities (in dots), which made small domain creation easier. Also, the net magnetization of AF domains should increase the effective interface interaction, shown in arrows.

Figure 3.20 shows the temperature dependence of H_E and the excessive moment ΔM, which was the shift of the *M*-*H* loops along the magnetization axis, of the sample $Fe_{0.57}Zn_{0.43}F_2$ / FeF_2 (1.0 nm) / Co. H_E(T) and ΔM(T) became zero at approximately the same temperature. Since the magnetic field was strong enough to saturate the F layer in either direction when *M*-*H* loop was measured, ΔM was therefore supposed to originate from the DAF surface. This seems to support the domain state picture that was proposed for CoO / Co system.[28] However, not all samples showed this temperature dependence.

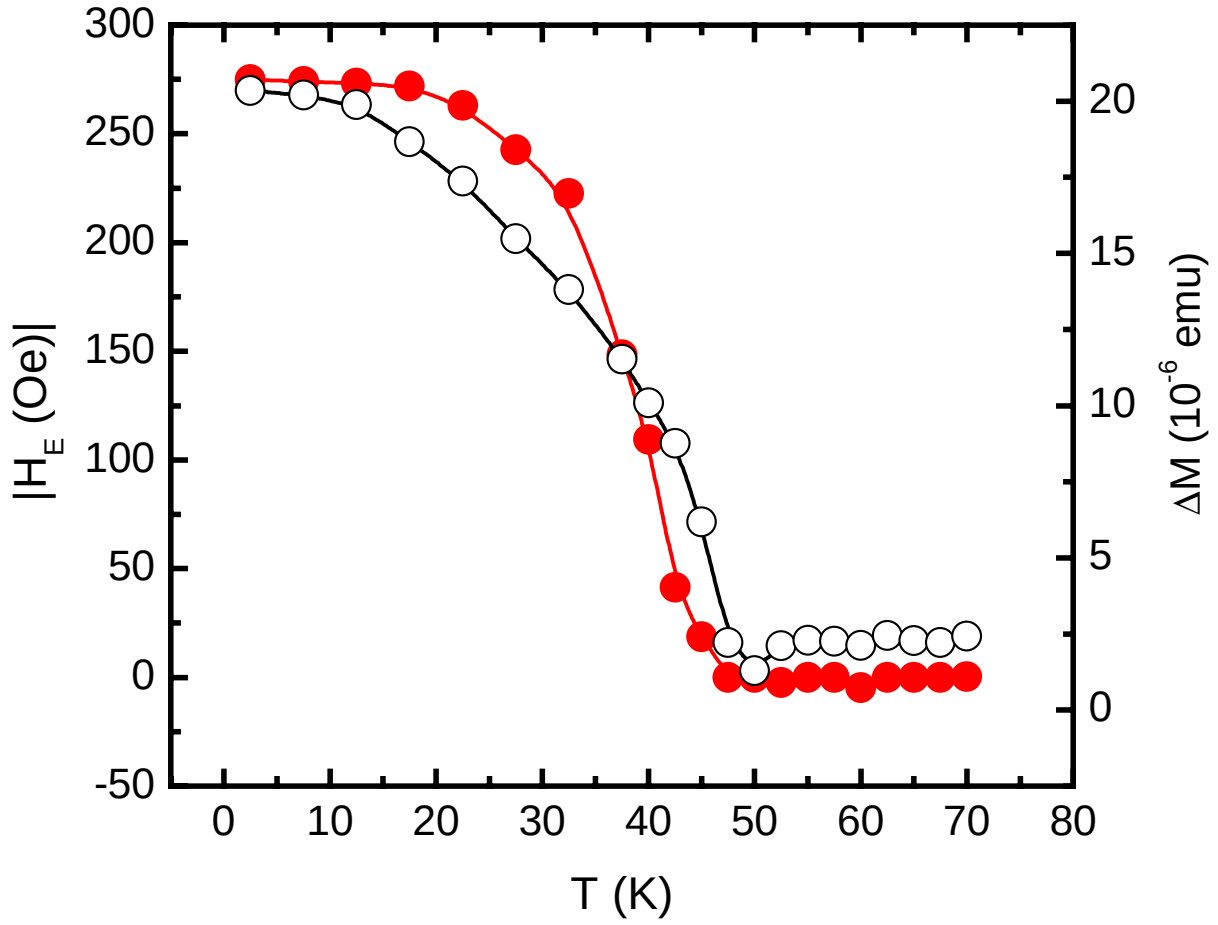

Figure 3.20: H_E (solid circles) and ΔM (open circles) as a function of temperature in sample $Fe_{0.57}Zn_{0.43}F_2$ / FeF_2 (1.0 nm) / Co. Lines are guides to the eye.

In Meiklejohn's simplest microscopic model, with uncompensated AF surface fixed during the F magnetization rotation, H_E is a result of the AF/F interface energy,[3]

$$\Delta E = \frac{2J_i S^2}{a^2}, \tag{3.13}$$

where J_i is the exchange constant at the interface, S is the spin, and a is the lattice paratmeter. Using the bulk Co values,[62] ΔE = 4.97 erg/cm^2. Using the bulk FeF_2 values[49], ΔE = 1.3 erg/cm^2, which is much closer to the experimental value.

Malozemoff's model,[26] which relies on the creation of AF domains perpendicular to the interface due to a random exchange field at the interface, resulting from defects, roughness, or lattice mismatch, predicts that for thick AF films,

$$\Delta E = \frac{4zA_{AF}}{\sqrt{\pi}L}, \tag{3.14}$$

where z is a factor of order unity, A_{AF} is the AF exchange stiffness and L is the AF domain size.

Taking L to be the domain wall size,

$$L = \pi\sqrt{\frac{A_{AF}}{K_{AF}}}, \tag{3.15}$$

with K_{AF} being the AF anisotropy, we get:

$$\Delta E = \frac{4z\sqrt{A_{AF}K_{AF}}}{\pi^{3/2}}. \tag{3.16}$$

Using FeF_2 K_{AF} and A_{AF} values, ΔE= 1.47 erg/cm^2, which has the same order of magnitude as our data. The advantage of this model is that no uncompensated AF surface is required, as long as an interfacial random exchnage interaction exists which creates small, slightly uncompensated AF

domains during cooling, which in FeF_2 could be due to the unequal coupling to the two sublattices. As Fig. 3.2 shows, the positions of the fluorine atoms is different for the two sublattices.

Nevertheless, Eq. (3.16) shows that ΔE only depends on the stiffness and anisotropy in the AF layer, which seems to indicate that domain creation is primarily responsible for exchange bias. Nonmagnetic impurities help form those domains in the DAF layers.

It is interesting to note that for $x = 0$ the sample with 1.0 nm of FeF_2 had a significant H_E at 2.5 K, with a $T_B = 12.5$ K. This represents approximately 3 – 4 monolayers of pure FeF_2. It is possible to speculate whether this temperature is consistent with 3D to 2D dimensional crossover effects (finite-size scaling[20]) or if this low transition temperature is due to defects. Previous experiments show that three monolayers of FeF_2 should have a $T_N \sim 33$ K,[20] if only finite size scaling effects diminished the transition temperature, and suggest the low T_B value results from disorder (e.g. island growth) which would tend to limit the lateral magnetic coherence length. The $x = 0$ sample without the interface layer was measured and showed no appreciable H_E. This confirms that the effect results from the interfacial AF-F interactions when the AF has long-range order, and not due to interdiffusion and the formation of CoF_2 ($T_N = 37.8$ K for CoF_2[63]).

Chapter 4

Angular Dependence of Exchange Bias in $Fe_xZn_{1-x}F_2$ / Co Bilayers

The angular dependence of H_E and the coercivity H_C was recently used to demonstrate that in general H_E does not have a simple $\cos\theta$ dependence in polycrystalline systems. The maximum H_E occurs at $\pi/4$ or $-\pi/4$ in NiFe / CoO bilayers,[64] whereas an in-plane four-fold symmetry is induced in Fe / MnPd bilayers after field cooling.[65] On the other hand, a pure $\cos\theta$ term is adequate for bilayers using amorphous $Co_{65}Mo_2B_{33}$ as the F layer,[66] presumably due to the suppression of the magnetic anisotropy in the F layer. It has also been demonstrated that there is an asymmetric angular dependence of the exchange coupling direction on the applied field direction in polycrystalline Co / CoO bilayers due to a rotatable anisotropy.[67] Very recently, it was pointed out that the complex angular dependence of H_E in polycrystalline bilayers can be explained by inhomogeneous AF/F interface coupling, possibly as a result of AF domain wall formation during the F magnetization reversal.[68]

Measurements of the dependence of H_E and H_C on the angle θ, which the applied magnetic field **H** makes with the AF easy axis, provide an independent test for the validity of existing theoretical models. The data can also be compared to those obtained by different techniques, such as ferromagnetic resonance (FMR),[69] Brilliouin light scattering (BLS),[70] or *ac* susceptibility.[71] The angular dependence of H_E and H_C can help understand the nature of the AF/F coupling at the interface, as well as the AF domain structure in the process of field cooling. Spin flop or perpendicular coupling between the AF and F can be easily verified from these measurements.

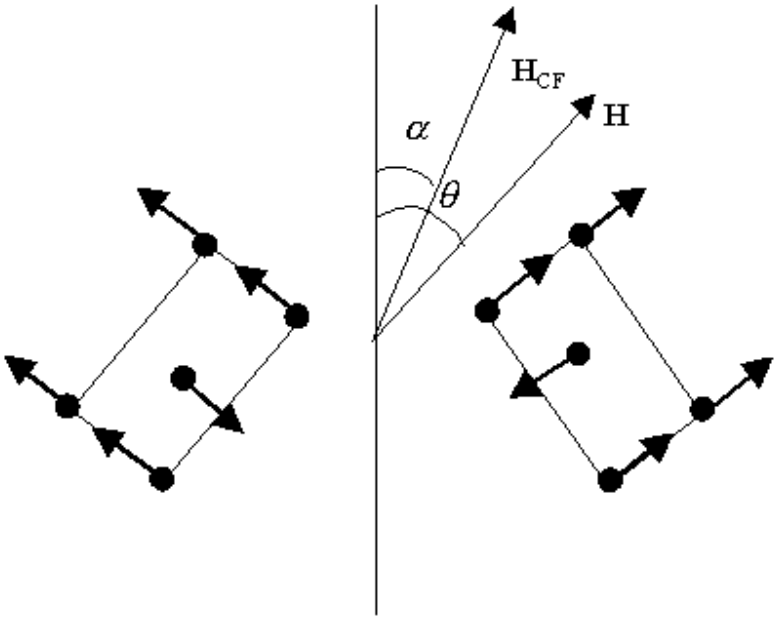

Figure 4.1: Angular dependence measurement geometry. Both the cooling field $\mathbf{H_{CF}}$ and the applied field **H** are with respect to the bisector of the perpendicular twins in the AF layer.

Magnetization measurements were performed using a vibrating sample magnetometer (VSM). The VSM was only sensitive to the magnetization component parallel to the applied field. Figure 4.1 shows the measurement geometry. The samples were cooled in a field H_{CF} = 2 kOe, as in the SQUID magnetometer measurements, from a temperature of at least T = 90 K, which is greater than the T_N of the AF, to T = 20 K. $\mathbf{H_{CF}}$ was applied at an angle α with respect to the bisector of the two perpendicular AF crystallographic domains. Subsequently, magnetic hysteresis loops were measured at T = 20 K in the –5 kOe to 5 kOe field range. The loops were measured at various angles θ with respect to the bisector of the perpendicular twins by manually rotating the sample in the VSM after field-cooling along a particular angle α. Both $\mathbf{H_{CF}}$ and **H** were applied in the film plane. H_E, H_C, and M_R were determined from the hysteresis loops. Hysteresis loops at T = 300 K and T = 90 K showed that Co does not have an in-plane anisotropy above T_N when deposited on top of the twinned $Fe_xZn_{1-x}F_2$ layers.

Figure 4.2 shows H_E, H_C, and the normalized M_R/M_S as functions of θ for a FeF_2 / Co bilayer and a $Fe_{0.84}Zn_{0.16}F_2$ / FeF_2 (1.0 nm) / Co sample after field-cooling along the $\alpha = 0$ and $\alpha = 45^0$ directions. Notice that H_E has a 360^0 symmetry, while H_C and M_R/M_S have 180^0 symmetry, which is a result of unidirectional nature of the exchange bias. For $\alpha = 0$, the most negative value of H_E ($H_{E,\,min}$) occurs at $\theta = 0$, as expected for a cooling field that is small and positive. Note that the maxima of H_C, M_R/M_S, and $H_{E,\,min}$ coincide perfectly.

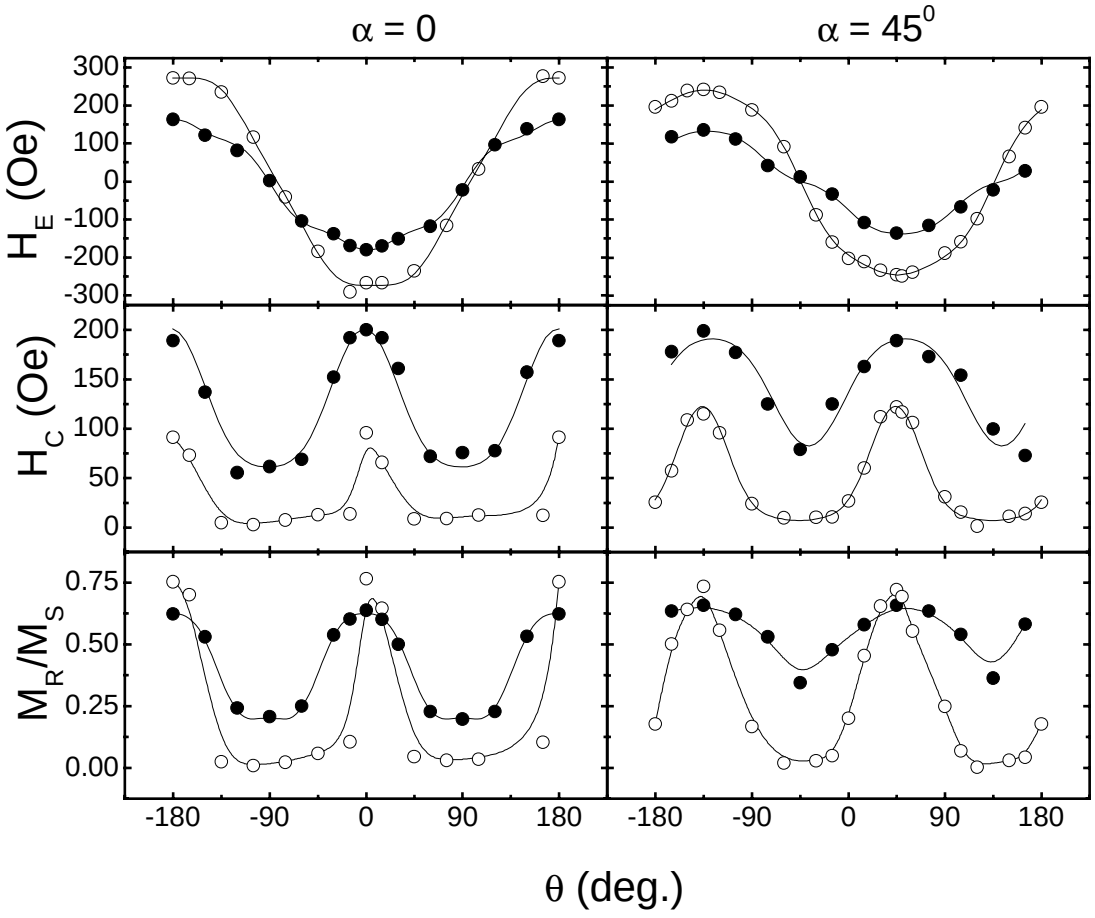

Figure 4.2: Angular dependence of H_E, H_C, and normalized remanence M_R/M_S of two different samples for $\alpha = 0$ and $\alpha = 45^0$. Solid dots are from Co on pure FeF_2, whereas the open dots are from a sample that has the following structure: $Fe_{0.84}Zn_{0.16}F_2$ / FeF_2 (1.0 nm) / Co. Lines are fits to Eqs. (4.2) - (4.4).

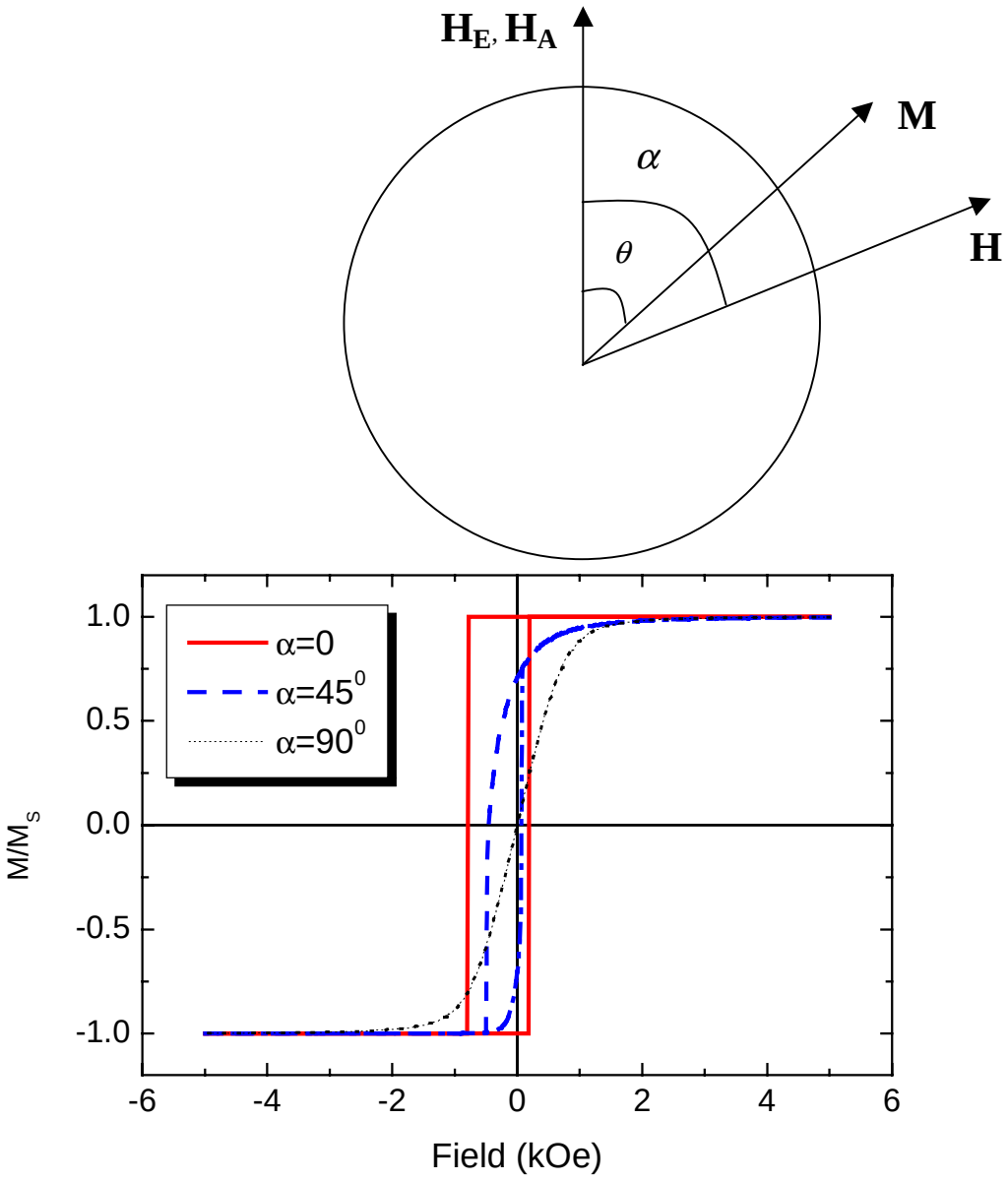

Figure 4.3: A single particle model, showing the dependence of the hysteresis loops on the direction of applied field **H**. α is the angle between the applied field **H** and the unidirectional anisotropy field $\mathbf{H_E}$, assumed to be parallel to the uniaxial anisotropy field $\mathbf{H_A}$ with the same magnitude.

In a simple single-particle model where the F layer has a uniaxial anisotropy K_1 and a unidirectional anisotropy field $\mathbf{H_E}$ due to exchange coupling to the AF, the magnetic free energy can be written as:

$$E = -H_E M t_F \cos\theta + K_1 t_F \sin^2\theta - MHt_F \cos(\alpha - \theta), \tag{4.1}$$

where t_F is the thickness of the F layer, **M** is the magnetization of the F layer, θ and α are the angles between the magnetization **M**, applied field **H** and the exchange coupling field $\mathbf{H_E}$, respectively. Hysteresis loops can be calculated by minimizing the energy with respect to θ, which is shown in Figure 4.3 by assuming that $\mathbf{H_E}$ is parallel to the uniaxial anisotropy field $\mathbf{H_A}$ with the same magnitude. Notice that the hysteresis loop is sheared when **H** is perpendicular to the unidirectional anisotropy field, which qualitatively agrees with the experimental data.

Interestingly, the peaks in H_C and M_R/M_S sharpen significantly as the Fe concentration, x, decreases. For $\alpha = 45^0$, H_{CF} points along the c-axis of one of the AF domains (see Figure 4.1). In this case a shift of the $H_{E,\,min}$, maxima of H_C, and M_R/M_S by 45^0 is clearly observed. In addition, the maxima of H_C, and M_R/M_S are significantly broadened compared to $\alpha = 0$ case, indicating the existence of a wider distribution of interface exchange anisotropy.

The solid curves in Figure 4.2 are fits to the following equations:

$$H_E = \sum_{n=1}^{\infty} H_{En} \cos((2n-1)(\theta - \phi)), \tag{4.2}$$

$$H_C = \sum_{n=0}^{\infty} H_{Cn} \cos(2n(\theta - \phi)), \tag{4.3}$$

$$M_R = \sum_{n=0}^{\infty} M_{Rn} \cos(2n(\theta - \phi)). \tag{4.4}$$

These equations represent a Fourier decomposition of H_E, H_C, and M_R, where ϕ is a phase difference with respect to θ = 0. This treatment is based on previous measurements of the angular dependence of these quantities, where it was shown that H_E can only have odd Fourier components and H_C and M_R must have even components.[64] The fitted coefficients for $H_E(\theta)$ are summarized in Table 4.1. In this case it was sufficient to go to the n = 3 term to reproduce the H_E data. Notice that the second term is only ~ 5% of the first term H_{E1}, which is negligible in this case. On the other hand, fitting H_C and M_R required higher order terms comparable to the zeroth order term, due to the sharply-peaked features shown in Figure 4.2. The simple $\cos\theta$ dependence of H_E demonstrates that the exchange bias is strongly influenced by the uniaxial magnetic anisotropy in the AF layer, which leads to a strong interface interaction during the cooling procedure.

Table 4.1. Summary of fitting parameters of H_E for $\alpha = 0$ and $\alpha = 45^0$, respectively, for twinned samples. $C_n = H_{En}/H_{E0}$. The uncertainties are ±2.5 Oe for H_{E0} and ± 0.025 for C_n.

Sample	H_{E0} (Oe)	$\alpha = 0$			H_{E0} (Oe)	$\alpha = 45^0$		
		C_1	C_2	C_3		C_1	C_2	C_3
FeF_2/Co	-171	1.00	-0.06	0.06	-126	1.00	0.12	-0.05
$Fe_{0.84}Zn_{0.16}F_2/FeF_2$(1.0 nm)/Co	-292	1.00	-0.03	-0.03	-258	1.00	-0.08	0.03
$Fe_{0.57}Zn_{0.43}F_2/FeF_2$(1.0 nm)/Co	-280	1.00	-0.04	-0.04	-242	1.00	-0.06	-0.03
$Fe_{0.62}Zn_{0.38}F_2$/Co	-111	1.00	-0.08	0.05	-73	1.00	-0.03	0.00
FeF_2/Co (untwinned)	-366	1.00	0.11	0.02				

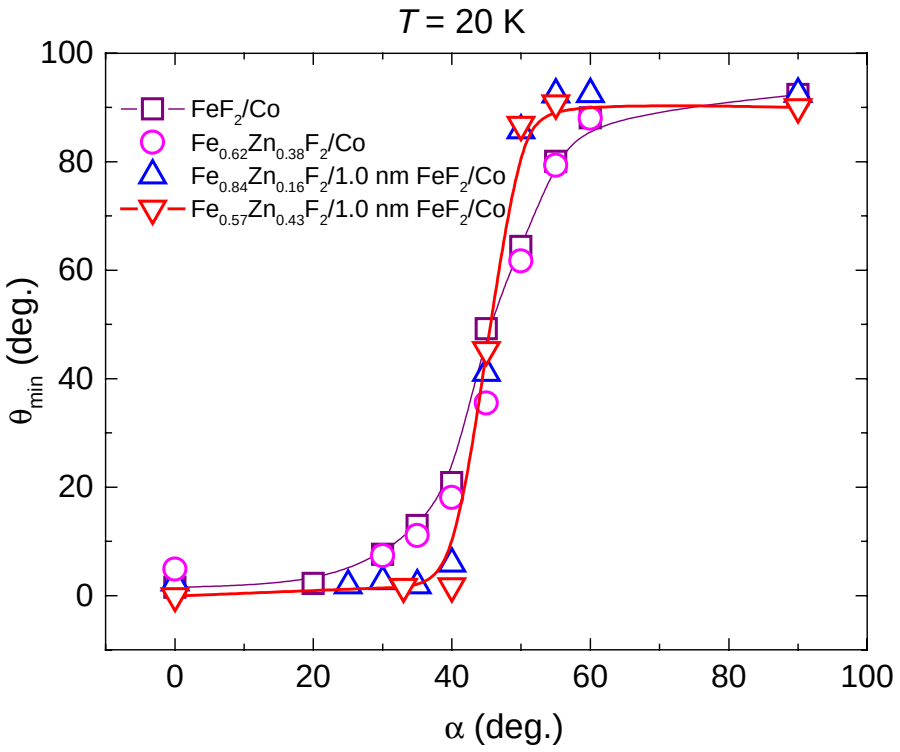

Figure 4.4: Angular position θ_{min} at which most negative H_E occurs as a function of the cooling field direction α, measured at T = 20 K for FeF_2 / Co (□); $Fe_{0.62}Zn_{0.38}F_2$ / Co (O); $Fe_{0.84}Zn_{0.16}F_2$ / FeF_2 (1.0 nm) / Co (Δ); and $Fe_{0.57}Zn_{0.43}F_2$ / FeF_2 (1.0 nm) / Co (∇).

Further insight can be gained by plotting the angle θ where the minimum value of H_E occurs (defined as $\theta_{\min}$), which coincides with H_C and M_R maxima, as shown in Figure 4.4. Notice that $\theta_{\min}$ remains unchanged for $\theta_{\min} = 0$ for $0^0 < \alpha < 30^0$, and then suddenly shifts to $\theta_{\min} = 90^0$ in the $30^0 < \alpha < 60^0$ range for the samples without the pure AF interface layer. This is a clear indication that there are two stable domain structures that form as the sample is field-cooled. Hence, when the sample is cooled within $\pm 30^0$ of one of the perpendicular bisectors, a stable AF structure forms such that the effective exchange anisotropy $H_{E,\,min}$ occurs in a direction along the perpendicular bisector. A more complicated structure presented in the 30^0 to 60^0 range, where a slight canting of the AF domains occurs. This provides evidence for the existence of an effective unidirectional anisotropy direction resulting from a frustration of the interface exchange interaction due to the small size of the AF structural domains. The size of these domains was determined by XRD to be ~ 6 nm – 10 nm using Eq. (3.12) (see section 3.2), which is much smaller than the lateral domain wall width of Co. The interface unidirectional anisotropy induced during the cool-down procedure is reversed in one of the domains in going from $\alpha = 30^0$ to $\alpha = 60^0$, causing the effective interface exchange field to rotate by 90^0, as illustrated in Figure 4.5.

Figure 4.4 also shows that the transition is substantially narrower for samples having 1.0 nm pure interface layer, independent of the Fe concentration. This result can be explained by assuming that the PAF/DAF short-range interface exchange interaction is significantly weaker than the PAF/F interactions. As the sample is cooled, the bulk of the AF orders more rapidly than the AF surface in contact with the F, in the same way that the surface of a ferro- or antiferromagnetic material orders more slowly as the temperature is lowered below its critical temperature.[72] At low temperatures, the DAF tends to freeze along its anisotropy direction,

whereas in samples with the PAF, the DAF will tend to make it easier to form domains that are not perfectly aligned along its easy direction. In other words, the PAF acts as a buffer between the F and the DAF, shielding the interaction between the DAF and the F layer, causing the domains in the DAF layer to align more easily along the AF uniaxial anisotropy direction.

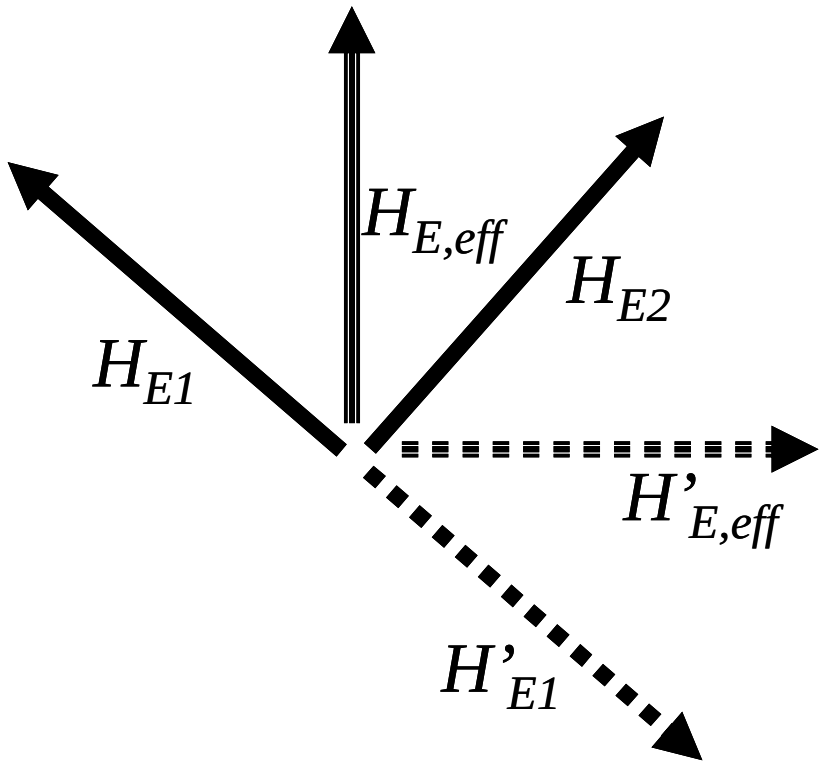

Figure 4.5: Schematic for the effective exchange anisotropy fields generated during the field-cooling procedures. $\mathbf{H_{E1}}$ and $\mathbf{H_{E2}}$ are the exchange fields generated by the two perpendicular crystallographic domains when the sample is cooled along $\alpha = 0$, and $\mathbf{H_{E,\,eff}}$ is the effective exchange field detected by the F layer. When the sample is cooled with $60^0 \leq \alpha \leq 90^0$, one of the domains reverses its magnetic structure, resulting in an exchange field $\mathbf{H'_{E1}}$, which causes the effective exchange field to rotate by 90^0 to $\mathbf{H'_{E,\,eff}}$.

The dependence of $H_{E,\,\min}$ on α is shown in Figure 4.6. In the $30^0 < \alpha < 60^0$ range the value of $|H_{E,\,\min}(\alpha)|$ abruptly dips to a value ~ $|H_{E,\,\min}(0)|/\sqrt{2}$, which occurs at $\alpha \sim 45^0$ for the pure

sample. As previously noted,[58] in this configuration $\mathbf{H_{CF}}$ points to parallel to one of the domains and perpendicular to the other. Since the coupling for each of the domains is parallel to the *c*-axis, the exchange bias for the domain with its *c*-axis perpendicular to $\mathbf{H_{CF}}$ is shut down during the cooling procedure, while the H_E for the other crystallographic domain is maximized. Assuming that the two crystallographic domains are on average identical in size, and that the maximum coupling to one of these domains is J_{eff}, the maximum value of $|H_{E,\,\text{min}}|$ is proportional to twice $J_{\text{eff}}/\sqrt{2}$ for $\alpha = 0$. On the other hand, for $\alpha = 45^0$, only one of the domains is active, so the maximum value of H_E is proportional to J_{eff}. A significant disagreement with this expectation was recently observed in FeF_2 / Fe bilayers, with $|H_{E,\,\text{min}}(45^0)|$ being a factor of 3 too small when the sample was cooled with H_{CF} applied 45^0 from the bisector.[58] This discrepancy can be explained by a small misalignment of H_{CF} with respect to the AF *c*-axis, on the order of 5^0 or less. Such a small misalignment could have caused the position of $H_{E,\,\text{min}}$ to shift by approximately $20^0 \sim 30^0$, yielding an apparently small value of $|H_E|$ measured along the cooling field direction. For the samples with the interface PAF layer in Figure 4.6, the dip is less evident, perhaps due to the sharpness of the angular transition, so that the actual minimum is not observed.

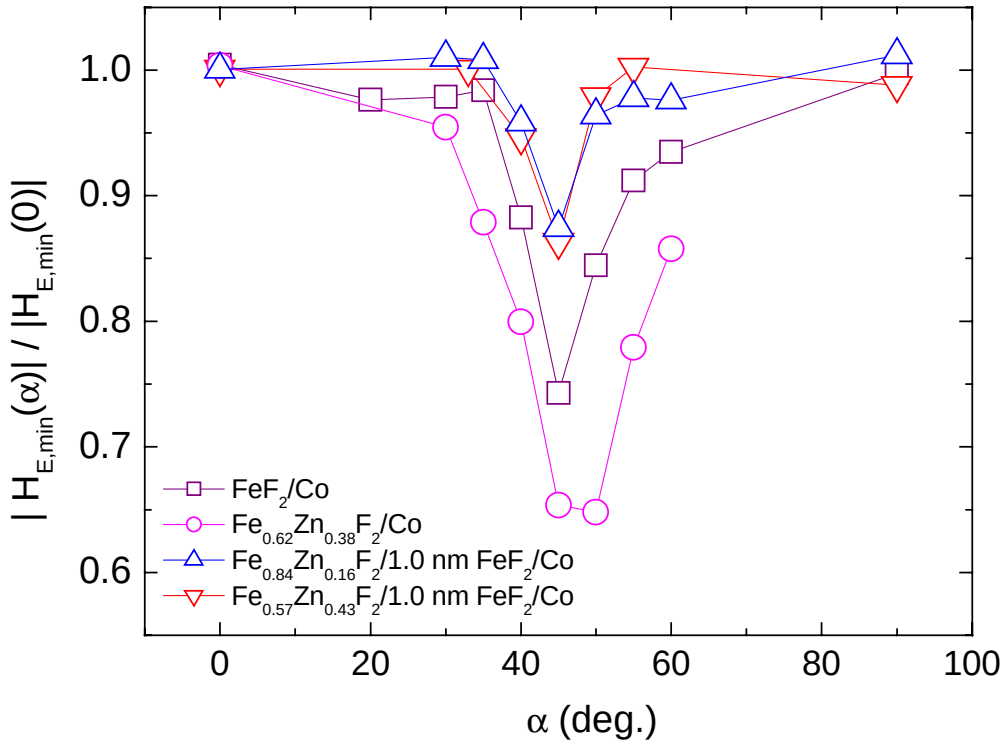

Figure 4.6: Magnitude of the maximum value of $|H_E|$ as a function of α.

Chapter 5

Exchange Bias in Single Crystal FeF_2 / Co Bilayers

In the second set of experiments, we used (110)-oriented single-crystal MgF_2 as the substrate to grow FeF_2. MgF_2 is a non-magnetic crystal and has the same rutile, *bct* crystal structure as FeF_2. The lattice parameters of MgF_2 are a = 0.462 nm, c = 0.305 nm, meaning that FeF_2 has a lattice mismatch of 1.7% along the *a*-axis, and 8% along the [001] *c*-axis. Before the substrate was loaded into the chamber, it was cleaned in methanol for 10 minutes ultrasonically. The temperature was set to T_S = 297 ^{0}C and waited 30 minutes before depositing FeF_2 onto the substrate. The samples had the following sandwich structure: MgF_2 (110)-substrate / 68 nm FeF_2 / 18 nm Co / 5 nm MgF_2, where Co was grown at 125 ^{0}C and the cap layer MgF_2 was grown at room temperature, as was done for samples grown on MgO substrates, to protect the sample from oxidation.

Figure 5.1 shows the *in-situ* RHEED measurement of lattice constant c of FeF_2 as a function of the film thickness. The e-beam was set to be parallel to $[1\bar{1}0]$ direction of the film. It can be seen that when the film is thicker than 50 nm, the c value of the film is the same as in the bulk. Sample with smaller thickness has certain amount of strain due to the lattice mismatch between the film and the substrate.

Figure 5.2 shows the RHEED pattern from a 68 nm thick FeF_2 film with the e-beam along FeF_2 $[1\bar{1}0]$ direction. Streaky pattern indicated that the AF surface was smooth and highly ordered, which was also confirmed by the *in-situ* AFM (OMICRON scanning probe microscopy SPM-SCALA 4.1) image, as shown in Figure 5.3. FeF_2 had a surface roughness of 0.55 nm. Co deposited on top of the FeF_2 had similar morphology.

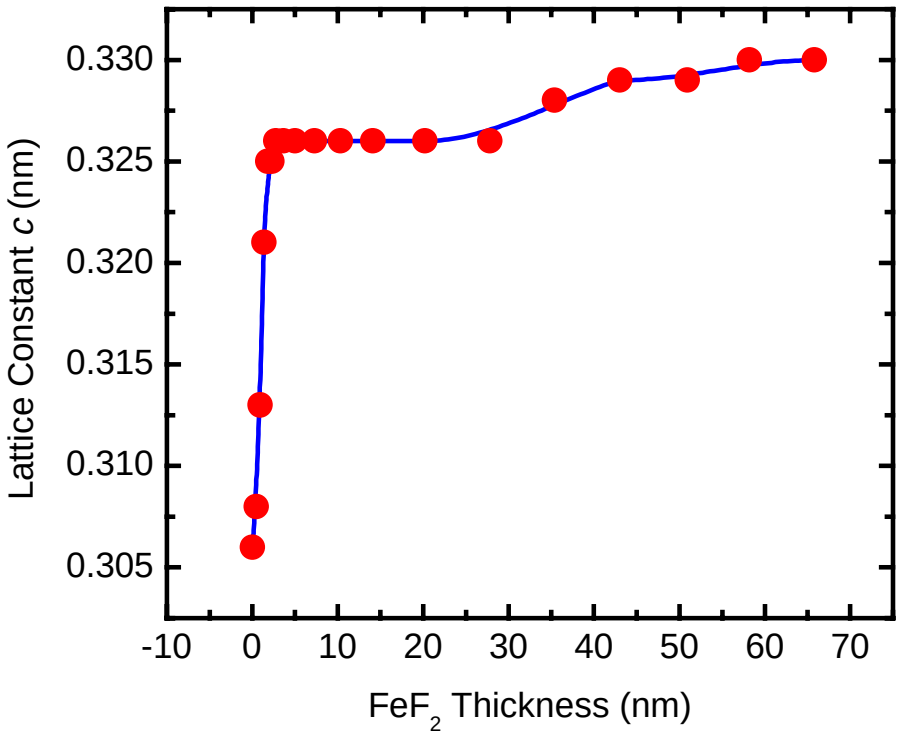

Figure 5.1: Lattice constant *c* of FeF_2 as a function of film thickness, determined by RHEED. Line is a guide to the eye.

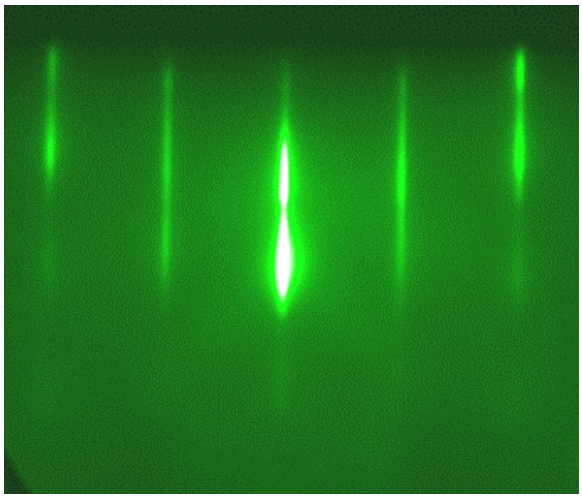

Figure 5.2: RHEED pattern from FeF_2, grown on (110)-oriented MgF_2 at 297 ^{0}C, with the e-beam parallel to FeF_2 $[1\bar{1}0]$ direction.

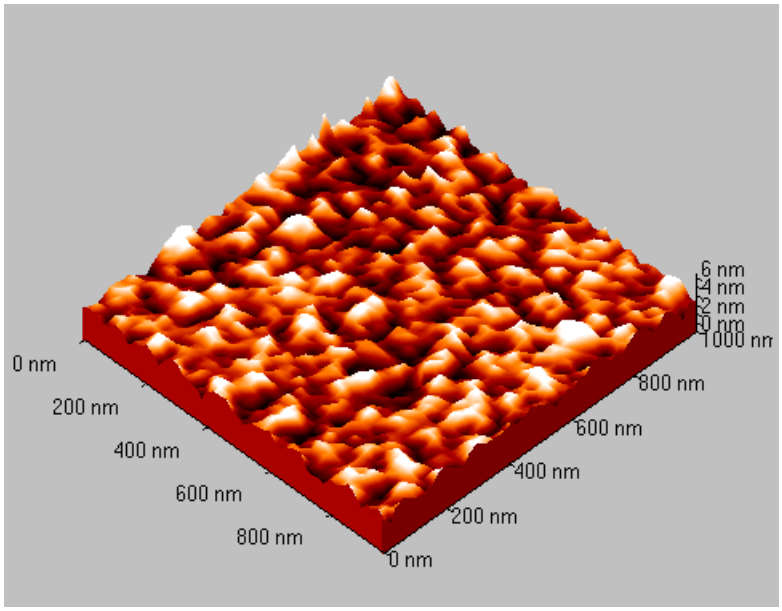

Figure 5.3: *In-situ* AFM image from FeF_2 film grown on (110)-MgF_2. Image size is 1 x 1 μm^2.

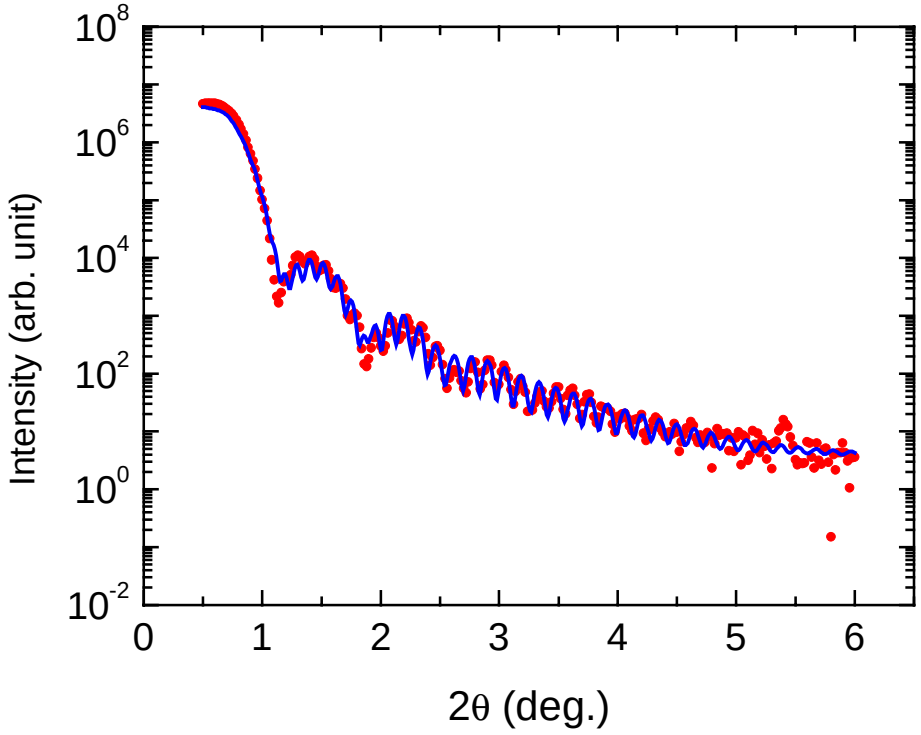

Figure 5.4: X-ray reflectivity data (red dots) and the fitting (blue line) using the recursive optical model. Interface roughness between FeF_2 and Co is 0.54 nm.

Figure 5.4 shows the x-ray reflectivity data of the FeF_2 / Co bilayer as well as the fitting using the recursive optical model, which results in an interface roughness of 0.54 nm, which agrees well with the AFM measurement.

Figure 5.5 shows high angle out-of-plane and in-plane *bct* (332) XRD scans from the film and the substrate. The Co film did not have any preferential crystal orientation. A two-fold symmetry from FeF_2 can be clearly seen, indicating that the sample was not twinned. The epitaxial relationship in this case is MgF_2 [001] || FeF_2 [001], MgF_2 [$1\bar{1}0$] || FeF_2 [$1\bar{1}0$].

Using the same procedure as we did for twinned FeF_2 samples, *i.e.*, Eqs. (3.3) - (3.12), the in-plane domain size was determined to be ~ 23 nm, approximately 3 times larger than the size in twinned samples grown on MgO.

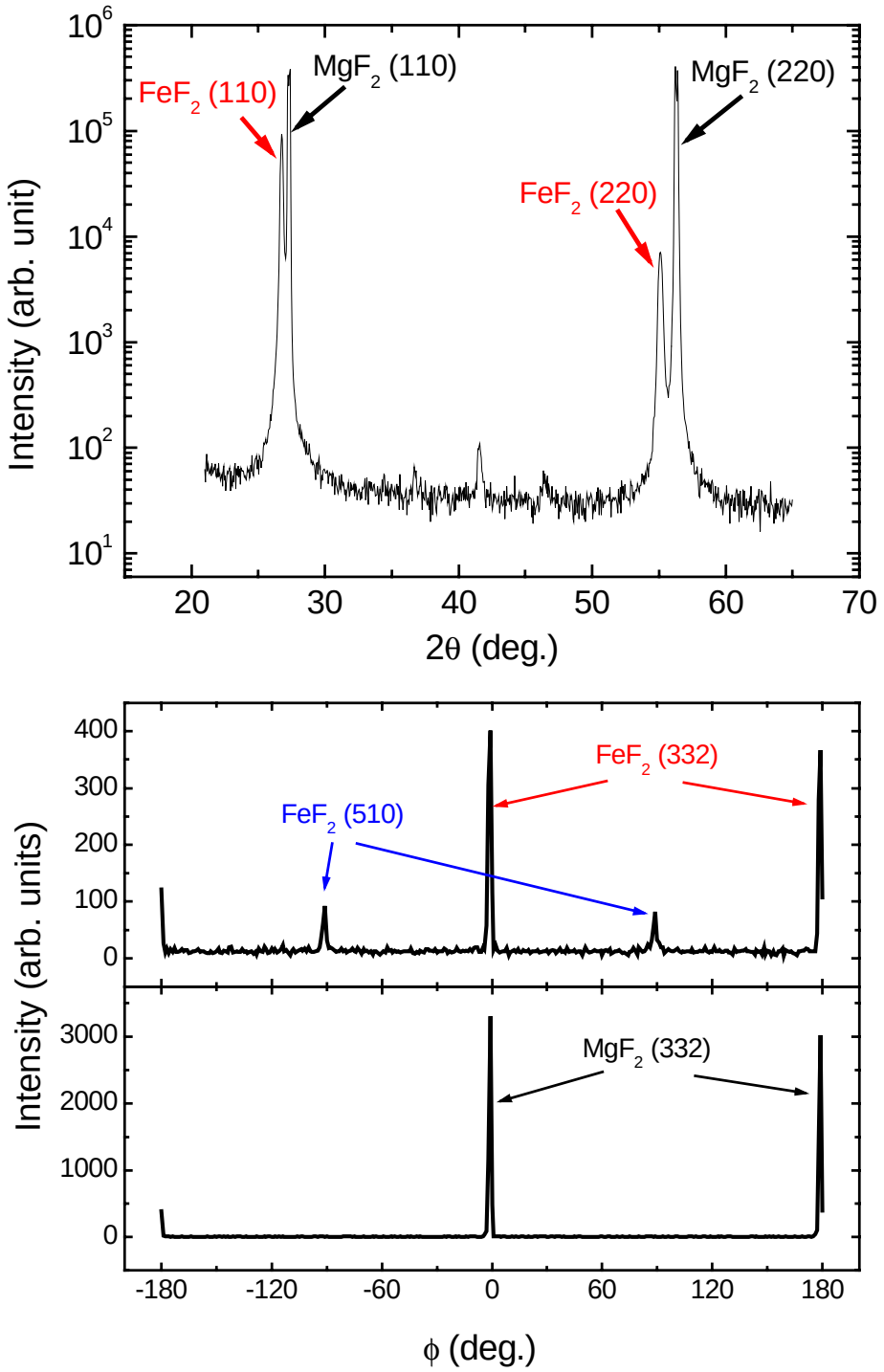

Figure 5.5: High angle x-ray diffraction from FeF_2 / Co bilayer sample grown on (110)-oriented MgF_2 substrate. (a) Out-of-plane; (b) in-plane FeF_2 (332); (c) in-plane MgF_2 (332). Small peaks unlabeled in (a) are from the substrate.

To characterize the magnetic anisotropy in the F layer, VSM measurements were performed on the sample at room temperature with the magnetic field **H** along different directions with respect to the AF easy *c*-axis, which is shown in Figure 5.6. It can be seen that an anisotropy exists in the Co layer with the easy axis parallel to FeF_2 [001] *c*-axis. Measurements at T = 90 K showed very similar results, indicating that above the AF's T_N, the easy axes of both F and AF layers are parallel to each other.

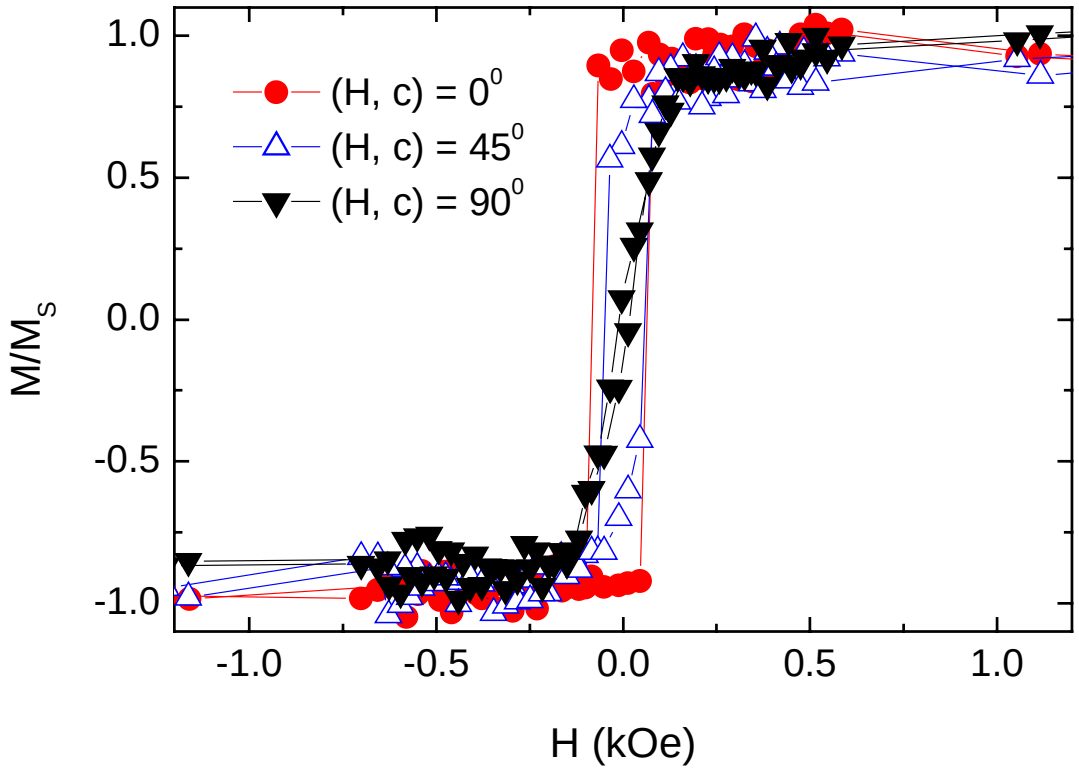

Figure 5.6: Hysteresis loops in FeF_2 / Co bilayer sample measured at T = 300 K with **H** parallel to (solid dots), 45^0 with respect to (up triangles), and 90^0 (down triangles) to the AF *c*-axis.

To investigate the exchange bias dependence on temperature, we performed SQUID magnetometry on the sample. Hysteresis loops were taken after field-cooling the sample from T = 90 K to T = 5 K in a magnetic field H_{CF} = 2 kOe, parallel to the FeF_2 easy *c* - axis.

Representative *M* - *H* loops with H parallel to the *c*-axis of the AF layer were shown in Figure 5.7 for T = 5 K, 45K, 90K, respectively. As can be seen, H_C decreases with temperature.

Figure 5.8 shows the H_E, H_C, and M_R/M_S dependence on temperature in the range of 5 K to 290 K. Notice that: 1) Large exchange bias is present at low temperature though the normalized remanence (M_R/M_S) of the hysteresis loops slightly decreases at low temperature due to the additional anisotropy induced in the F layer during field cooling[73]. In our case, M_R/M_S is approximately 0.55 at T = 5 K, much more than 0.1 in the FeF_2 / Fe bilayers where a perpendicular coupling[47] between the F and the AF layers was proposed. Neutron diffraction experiments[58] indeed demonstrated that such perpendicular coupling is not sufficient to result in exchange bias, nor is it necessary. 2) Coercivity peaks at close to the AF's T_N and that enhancement was still there even when T was much higher than T_N. This was observed by other groups,[74] and interpreted in terms of the spin fluctuations when the temperature was close to T_N.

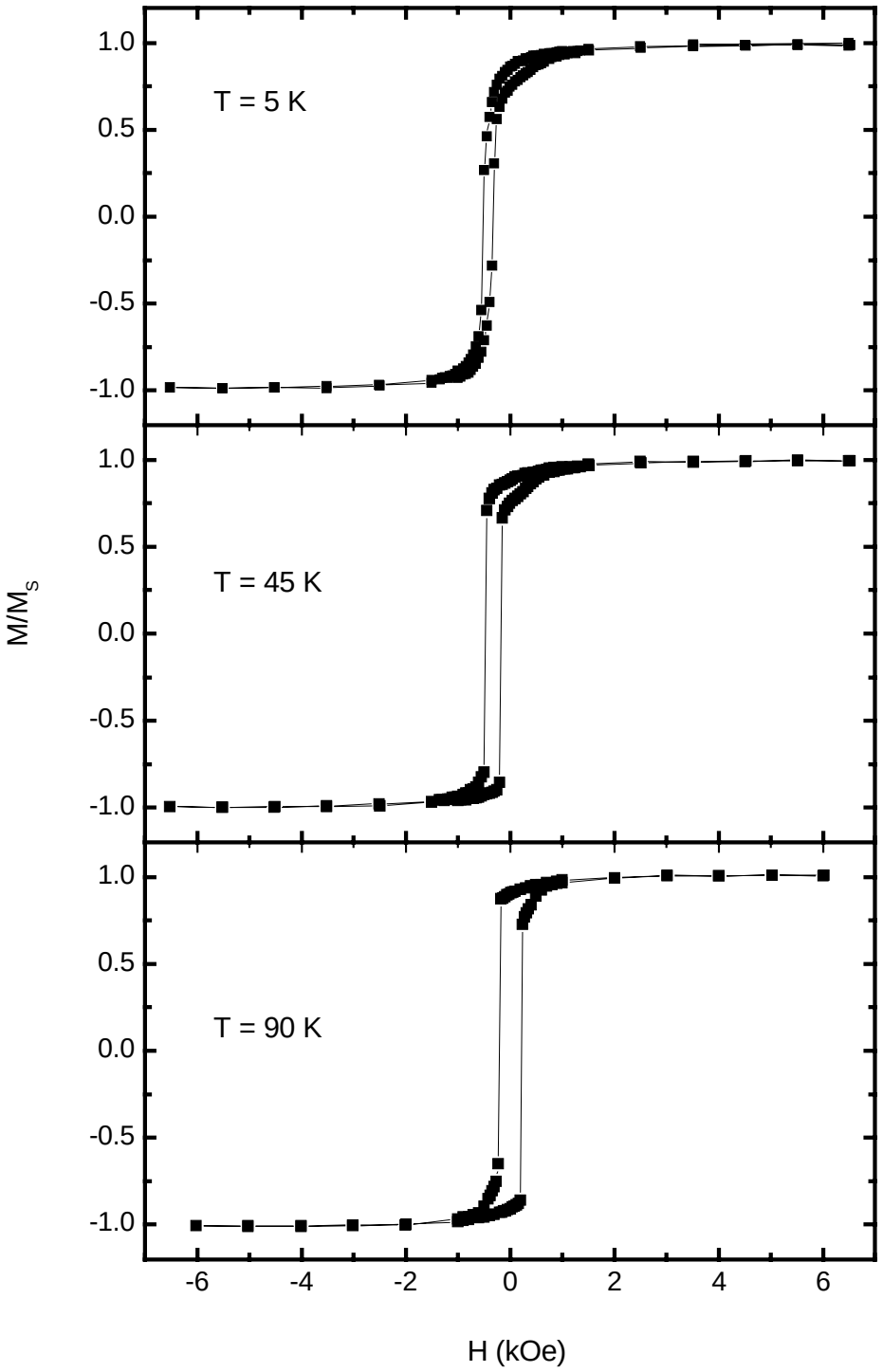

Figure 5.7: Hysteresis loops at T = 5 K, 45 K, and 90 K after field cooling in a magnetic field of H_{CF} = 2 kOe, parallel to FeF_2 [001] direction.

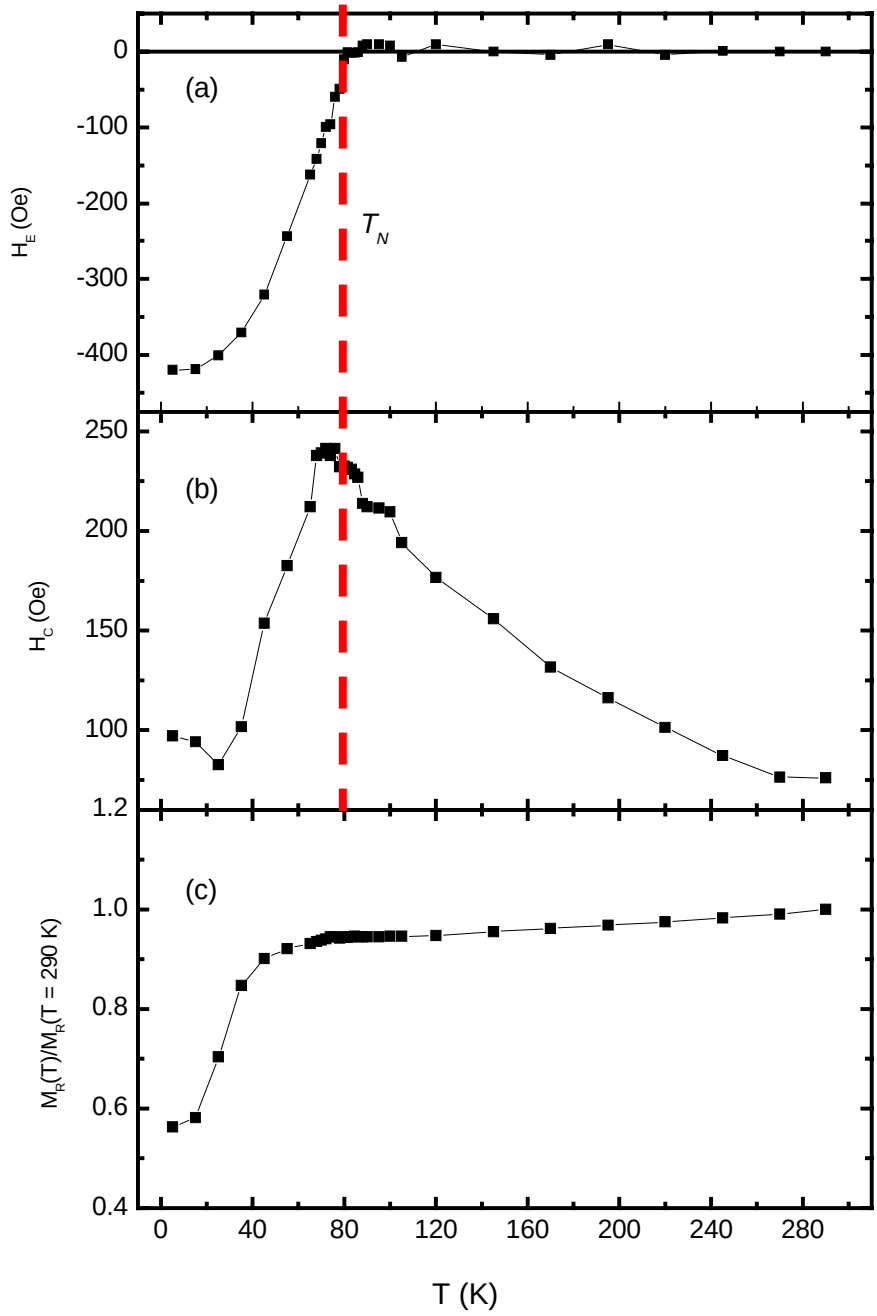

Figure 5.8: Exchange bias, coercivity, and normalized remanence as functions of temperature after field cooling at H_{CF} = 2 kOe along FeF_2 *c*-axis.

In order to see if the exchange bias field flips in untwinned AF/Co bilayer samples, the angular dependence of H_E was also measured via VSM, using the procedure described in Chapter 4. Figure 5.9 shows that a large exchange bias is present if the sample is field-cooled from room temperature to 20 K in a field H_{CF} = 2 kOe parallel to the *c*-axis of the AF layer, and then measured along *c*-axis. However, no exchange bias is observed with **H** perpendicular to *c*-axis, which implies that H_E in all AF domains is parallel to *c*-axis ($\mathbf{H_E} \parallel c$). Figure 5.9 also shows that after the sample is field-cooled with $\mathbf{H_{CF}} \perp c$, there is no net exchange bias with $\mathbf{H} \parallel c$ or $\mathbf{H} \perp$ c. Nevertheless, a double loop is observed with $\mathbf{H} \parallel c$, indicating that the local $\mathbf{H_E}$ vector direction in the AF layer can take one of two antiparallel directions. This is likely due to the formation of antiparallel domain states in the AF, where the staggered magnetization vectors are antiparallel to each other, and the strong uniaxial anisotropy in FeF_2 does not permit the formation of significantly canted states at low temperatures.

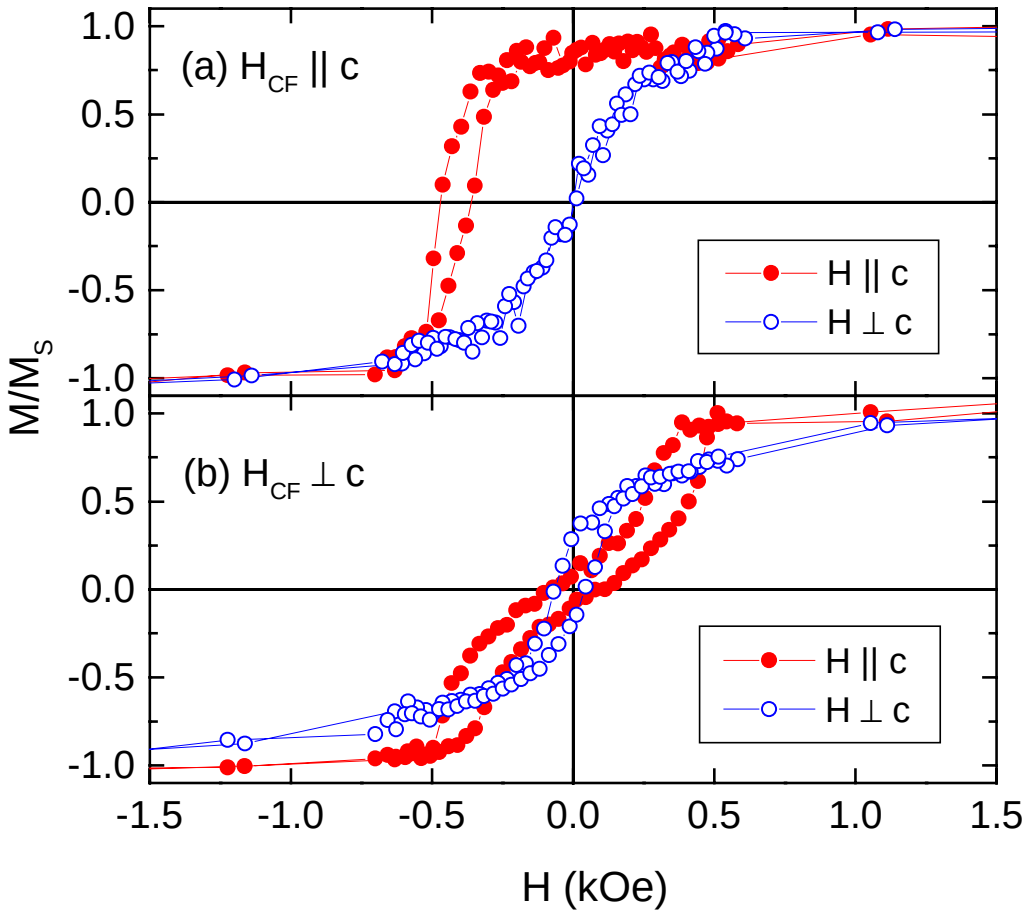

Figure 5.9: Exchange bias in single crystal FeF_2 / Co bilayer with (a) $\mathbf{H_{CF}} \parallel c$, then measured with $\mathbf{H} \parallel c$, $\mathbf{H} \perp c$; (b) $\mathbf{H_{CF}} \perp c$, then measured with $\mathbf{H} \parallel c$, $\mathbf{H} \perp c$.

The exchange bias angular dependence in untwinned FeF_2 / Co bilayer sample with $\mathbf{H_{CF}} \parallel c$ is shown in Figure 5.10. The angular dependence of the twinned sample is also shown for comparison purposes, and the results of the fit to the Eqs. (4.2) - (4.4) are shown in Table 4.1. Clearly the first order $\cos\theta$ term still dominates, but the second order term is now an appreciable 11% and positive, indicating that the interface coupling may not entirely be collinear.

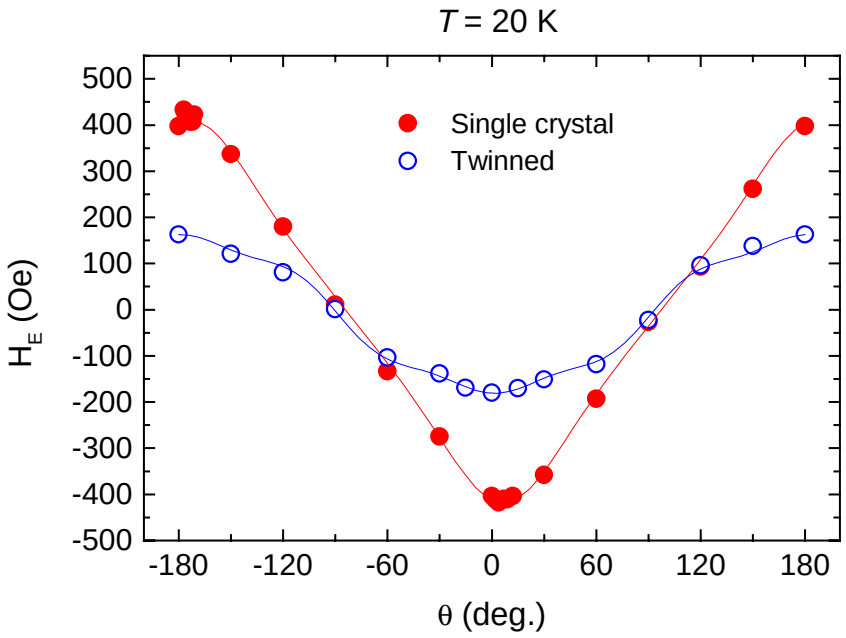

Figure 5.10: Angular dependence of H_E for untwinned FeF_2 / Co sample (●) when cooled along the *c*-axis of the FeF_2. As a comparison, twinned sample is also shown (O). Solid curves are fits to Eqs. (4.2) - (4.4). Samples were measured at T = 20 K.

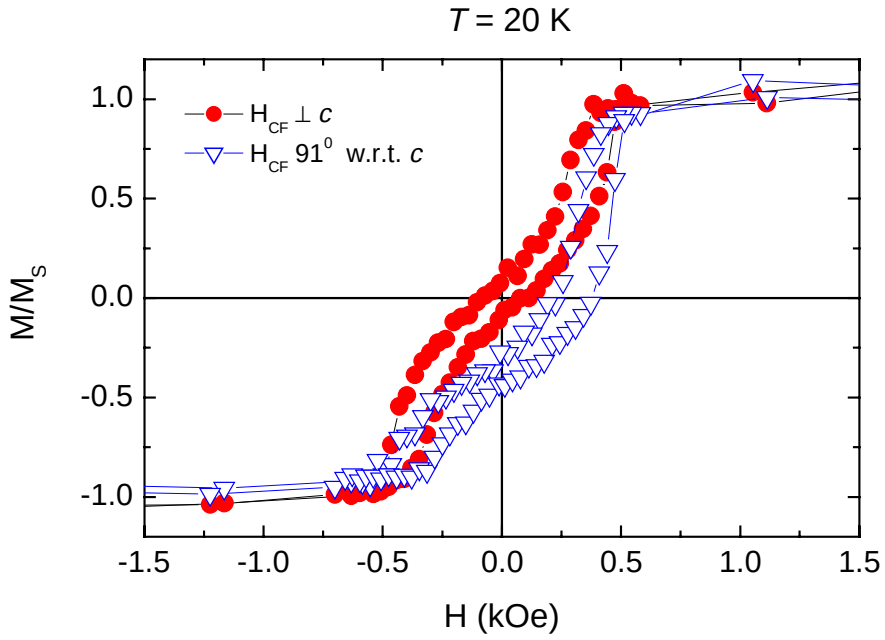

Figure 5.11: Hysteresis loops with the applied field along the *c*-axis of FeF_2 after field cooling (a) 90 degrees (red dots); (b) 91 degrees (blue triangles) with respect to the *c*-axis of FeF_2.

Finally, the extreme sensitivity of the exchange bias to the cooling field direction is shown in Figure 5.11. The figure demonstrates that cooling in a direction just 1^0 away from the direction perpendicular to the AF *c*-axis results in a significant positive exchange bias of ~ 300 Oe. By assuming that the sample breaks up into regions of positive and negative H_E, the data show that roughly 75% of the sample has a positive H_E due to the 1^0 misalignment. This remarkable angular sensitivity is reminiscent of the extreme sensitivity of the spin-flop transition in bulk MnF_2 to the applied field direction.[75] It is possible that the two effects have the same physical origin if the AF/F interface exchange interaction selects one of the two possible domain structures in the AF depending on the direction of the cooling field. In the bulk material, the domains would have the same energy, and the only way to make the sample single domain is to go through the spin-flop transition and then lower the field to zero. In the case of the exchange bias, the cooling field breaks the symmetry during the cooling procedure.

Chapter 6

Conclusions and Future Work

In conclusion, by using UHV molecular beam epitaxy, we deposited (110)-oriented dilute antiferromagnet $Fe_xZn_{1-x}F_2$ on MgO (100) substrate. Surface roughness was between 0.2 nm and 0.9 nm. We observed that the dilute antiferromagnets had perpendicular twins in the film plane. SQUID magnetometry showed that for $x > 0.25$, the blocking temperature T_B was linearly dependent on the concentration of Fe in the dilute layers, coinciding with the T_N of the bulk dilute crystals. H_E got enhanced by 65% when $x = 0.84$, compared to the pure FeF_2 / Co bilayer, which was presumably due to the formation of domain states inside the dilute antiferromagnetic layers. Pure FeF_2 interface layer was found to be very crucial in increasing the coupling between the F and the AF layers.

The angular dependence of H_E, H_C and M_R on the cooling field direction showed that there were two equivalent domain states in the AF layers. The most negative H_E occurred along the AF easy *c*-axis for $0 \leq \alpha \leq 30^0 \sim 40^0$, where α is the angle between the cooling field and the AF easy axis. An exchange bias flop occurred if α was increased further. The 1.0 nm pure FeF_2 interface layer acted as a buffer for the interface interaction, resulting in a sharper exchange bias flop transition. Such spin flop picture was further demonstrated in single crystal FeF_2 / Co bilayers.

These experiments have demonstrated that the interface coupling responsible for H_E is extremely sensitive to the underlying magnetic anisotropy of the AF layer, and that the direction of the cooling field does not necessarily determine the direction of H_E.

In the future, untwinned dilute $Fe_xZn_{1-x}F_2$ can be grown on single crystal (110)-oriented MgF_2 substrates, followed by Co layers. Exchange bias dependence on the dilution, domain structure can therefore be investigated and compared to the twinned dilute samples.

Another interesting work is to investigate the exchange bias in NiF_2 / Co bilayers, because NiF_2 is a weak ferromagnet with the spins antiferromagnetically ordering along [100] or [010] direction (off by 0.9^0). However, NiF_2 has the same *bct* crystal structure as FeF_2 with much smaller lattice mismatch when grown on MgF_2 substrates (< 1% along *a*- or *c*-axis). Therefore, by varying the thickness of the NiF_2 layers, the strain effect in NiF_2 on the exchange bias could be addressed. Neutron diffractions, as well as SQUID magnetometry, could be employed to investigate the Néel temperatures of the NiF_2 layers, as well as the blocking temperatures in such bilayers.

Bibliography

[1] R.G. Piety, Phys. Rev. **50**, 1173(1936); K. Honda and S. Kaya, Sci. Rept. Tohoku Univ. **15**, 721 (1926).

[2] W.H. Meiklejohn and C.P. Bean, Phys. Rev. **102**, 1413 (1956).

[3] W.H. Meiklejohn and C.P. Bean, Phys. Rev. **105**, 904 (1957).

[4] S. Gangopadhyay, G.C. Hadjipanayis, C.M. Sorensen, and K.J. Klabunde, J. Appl. Phys. **73**, 6964 (1993).

[5] Y.D. Yao, Y.Y. Chen, M.F. Tai, D.H. Wang, and H.M. Lin, Mater. Sci. Eng. A **217/218**, 281 (1996).

[6] W.H. Meiklejohn, J. Appl. Phys. **29**, 454 (1958); W.H. Meiklejohn, J. Appl. Phys. Supplement to Vol. **33**, 1328 (1962).

[7] C.M. Hsu, H.M. Lin, and K.R. Tsai, J. Appl. Phys. **76**, 4793 (1994).

[8] C. Tang, J. Appl. Phys. **55**, 2226 (1984).

[9] B.Y. Wong, C. Mitsumata, S. Prakash, D.E. Laughlin, and T. Kobayashi, J. Appl. Phys. **79**, 7896 (1996).

[10] Ch. Binek, A. Hochstrat, and W. Kleemann, J. Magn. Magn. Mater. **234**, 353 (2001).

[11] M.S. Lund, W.A.A. Macedo, K. Liu, J. Nogués, I.K. Schuller, and C. Leighton, Phys. Rev. B **66**, 054422 (2002).

[12] D.D. Tang, P.K. Wang, V.S. Speriosu, S. Le, and K.K. Kung, IEEE Trans. Magn. **31**, 3206 (1995).

[13] C.H. Lai, T.J. Regan, R.L. White, and T.C. Anthony, J. Appl. Phys. **81,** 3989 (1997).

[14] For a review, see J. Nogués and I.K. Schuller, J. Magn. Magn. Mater. **192**, 203 (1999).

[15] B.H. Miller and E.D. Dahlberg, J. Appl. Phys. **81**, 5002 (1997).

[16] P.J. van der Zaag, A.R. Ball, L.F. Feiner, R.M. Wolf, and P.A.A. van der Heijden, J. Appl. Phys. **79**, 5103(1996).

[17] Z.Q. Lu, W.Y. Lai, and C.L. Chai, Thin Solid Films, **375,** 224 (2000).

[18] J. Nogués, D. Lederman, T.J. Moran, I.K. Schuller, and K.V. Rao, Appl. Phys. Lett. **68**, 3186 (1996).

[19] I.N. Krivorotov, C. Leighton, J. Nogués, I.K. Schuller, and E.D. Dahlberg, Phys. Rev. B **65**, 100402 (2002).

[20] D. Lederman, C.A. Ramos, V. Jaccarino, and J.L. Cardy, Phys. Rev. B **48**, 8365 (1993).

[21] D. Mauri, E. Kay, D. Scholl, and J.K. Howard, J. Appl. Phys. **62**, 2929 (1987).

[22] R. Jungblut, R. Coehoorn, M.T. Johnson, J. aan de Stegge, and A. Reinders, J. Appl. Phys. **75**, 6659 (1994).

[23] J. Nogués, T.J. Moran, D. Lederman, I.K. Schuller, and K.V. Rao, Phys. Rev. B **59**, 6984 (1999).

[24] M.R. Fitzsimmons, C. Leighton, A. Hoffmann, P.C. Yashar, J. Nogués, K. Liu, C.F. Majkrzak, J.A. Dura, H. Fritzsche, I.K. Schuller, Phys. Rev. B **64**, 104415 (2001).

[25] D. Mauri, H.C. Siegmann, P.S. Bagus, and E. Kay, J. Appl. Phys. **62**, 3047 (1987).

[26] A.P. Malozemoff, Phys. Rev. B **35**, 3679 (1987).

[27] N.C. Koon, Phys. Rev. Lett. **78**, 4865 (1997).

[28] P. Miltényi, M. Gierlings, J. Keller, B. Beschoten, G. Güntherodt, U. Nowak, and K.D. Usadel, Phys. Rev. Lett. **84**, 4224 (2001).

[29] M. Kiwi, J. Mejía-Lopez, R.D. Protugal, and R. Ramírez, Solid State Comm. **116**, 315 (2000).

[30] P. Steadman, M. Ali, A.T. Hindmarch, C.H. Marrows, B.J. Hickey, S. Langridge, R.M. Dalgliesh, and S. Foster, Phys. Rev. Lett. **89**, 077201 (2002).

[31] A.E. Berkowitz and K. Takano, J. Magn. Magn. Mater. **200**, 552-570 (1999).

[32] H. Ohldag, A. Scholl, F. Nolting, S. Anders, F.U. Hhillebrecht, and J. Stöhr, Phys. Rev. Lett. **86**, 2878 (2001).

[33] W.J. Antel, Jr., F. Perjeru, and G.R. Harp, Phys. Rev. Lett. **83**, 1439 (1999).

[34] M.D. Stiles and R.D. McMichael, Phys. Rev. B **60**, 12950 (1999).

[35] D.P. Woodruff and T.A. Delchar in Modern Techniques of Surface Science, 2nd edition, University Press, Cambridge (1994).

[36] K-Space Associates, Inc., KSA 400 User Manual.

[37] T. Charlton, Ph.D. dissertation, Growth, Characterization, and Properties of Co/Re Superlattices, West Virginia University, 22 (2001).

[38] M. Fatemi, Appl. Phys. Lett. **80**, 935 (2002).

[39] T. Charlton, J. McChesney, D. Lederman, F. Zhang, J.Z. Hilt, and M.J. Pechan, Phys. Rev. B **59**, 11897 (1999).

[40] E.E. Fullerton, I.K. Schuller, H. Vanderstraeten, and Y. Bruynseraede, Phys. Rev. B **45**, 9292 (1992).

[41] B. Vida and P. Vincent, Appl. Opt, **23**, 1794 (1984).

[42] W.H. Press, S.A. Teukolsky, W.T. Vetterling, and B.P. Flannery, Numerical Recipes in C: The Art of Scientific Computing (Cambridge University Press, Cambridge, 1992).

[43] EG & G Princeton Applied Research, Model 4500 Vibrating Sample Magnetometer Instruction Manual, 2-15 (1987).

[44] W.G. Jenks, I.M. Thomas, and J.P. Wikswo, Encyclopedia of Appl. Phys. **19**, 457 (1997).

[45] A.P. Malozemoff, J. Appl. Phys. **63**, 3874 (1988).

[46] Y. Imry and S.K. Ma, Phys. Rev. Lett. **35**, 1399 (1975).

[47] T.J. Moran, J. Nogués, D. Lederman, and I.K. Schuller, Appl. Phys. Lett. **72**, 617 (1998).

[48] Y. Irjiri, J.A. Borchers, R.W. Erwin, and S.H. Lee, Phys. Rev. Lett. **80**, 608 (1998).

[49] J.W. Stout and S.A. Reed, J. Am. Chem. Soc. **76**, 5279 (1954).

[50] D.P. Belanger, P. Nordblad, A.R. King, and V. Jaccarino, J. Magn. Magn. Mater. **31-34**, 1095 (1983).

[51] R.A. Erickson, Phys. Rev. **90**, 779 (1953).

[52] M.T. Hutchings, B.D. Rainford, and H.J. Guggenheim, J. Phys. C **3**, 307 (1970).

[53] K.V. Krishna-Rao, AIP Conference Proceedings, **17**, 219 (1973).

[54] For a review of RFIM, see D.P. Belanger, and A.P. Young, J. Magn. Magn. Mater. **100**, 272 (1991).

[55] J. Nogués, C. Leighton, and I.K. Schuller, Phys. Rev. B **61**, 1315 (2000).

[56] S. Adenwalla, G.P. Felcher, J. Nogués, and I.K. Schuller, J. Appl. Phys. **81**, 5307 (1997).

[57] B.E. Warren, *X*-ray Diffraction (Dover Publications Inc, New York, 1990), 251.

[58] M.R. Fitzsimmons, C. Leighton, J. Nogués, A. Hoffmann, K. Liu, C.F. Majkrzak, J.A Dura, J.R. Groves, R.W. Springer, P.N. Arendt, V. Leiner, H. Lauter, and I.K. Schuller, Phys. Rev. B **65**, 134436 (2002).

[59] G.K. Wertheim, D.N.E. Buchanan, and H.J. Guggenheim, Phys. Rev. **152**, 527 (1966).

[60] K. Jonason, C. Djurberg, P. Nordblad, and D.P. Belanger, Phys. Rev. B **56**, 5404 (1997).

[61] For a review of DAF's, see D.P. Belanger, Spin Glasses and Random Fields, edited by A.P. Young (World Scientific, Singapore, 1998).

[62] C. Kittle, Introduction to Solid State Physics, 7th ed. (Wiley, New York, 1996), p. 426.

[63] R.A. Cowley, W.J.L. Buyers, P. Martel, R.W.H. Stevenson, J. Phys. C**6**, 2997 (1973).

[64] T. Ambrose, R.L. Sommer, and C.L. Chien, Phys. Rev. B **56**, 83 (1997).

[65] Y.J. Tang, B.F.P. Roos, T. Mewes, A.R. Frank, M. Rickart, M. Baur, S.O. Demokritov, B. Hillebrands, X. Zhou, B.Q. Liang, X. Chen, and W.S. Zhan, Phys. Rev. B **62**, 8654 (2000).

[66] X.W. Wu, T. Ambrose, and C.L. Chien, Appl. Phys. Lett. **72**, 2176 (1998).

[67] T. Gredig, I.N. Krivorotov, C. Merton, A.M. Goldman, and E.D. Dahlberg, J. Appl. Phys. **87**, 6418 (2000).

[68] M.D. Stiles and R.D. McMichael, Phys. Rev. B **63**, 064405 (2001).

[69] M.J. Pechan, D. Bennett, N. Teng, C. Leighton, J. Nogués, and I.K. Schuller, Phys. Rev. B **65**, 064410 (2002).

[70] A. Ercole, T. Fujimoto, M. Patel, C. Daboo, R.J. Hicken, J.A.C. Bland, J. Magn. Magn. Mater. **156**, 121(1996).

[71] B. Kuhlow, M. Lambeck, H. Schroeder-Furst, and J. Wortman, Phys. Lett. A, **34**, 223 (1971).

[72] S. Alvarado, M. Campagna, and H. Hopster, Phys. Rev. Lett. **48**, 51 (1981).

[73] M. Grimsditch, A. Hoffman, D. Lederman, and H. Shi, to be published.

[74] C. Leighton, H. Suhl, M.J. Pechan, R. Compton, J. Nogués, and I.K. Schuller, J. Appl. Phys. **92**, 1483 (2002).

[75] G.P. Felcher and R. Kleb, Europhys. Lett. **36**, 455 (1996).

Vita

Hongtao Shi

Education

Ph.D. Physics	West Virginia University, 2002
M.S. Course Work	West Virginia University, 1998
M.S. Physics	Nanjing University, China, 1992
B.S. Physics	Nanjing University, China, 1989

Employment

Research Assistant	West Virginia University, 1996, 1998 – 2002
Teaching Assistant	West Virginia University, 1997
Research Assistant Professor	Nanjing University, China, 1992 – 1995

Awards and Honors

Graduate Fellowship	Nanjing University, China, 1990 – 1991
B.S. with honors	Nanjing University, China, 1989

Professional Activities

Memberships	American Physical Society
	Materials Research Society